Distribution Agreement

In presenting this thesis or dissertation as a partial fulfillment of the requirements for an advanced degree from Emory University, I hereby grant to Emory University and its agents the non-exclusive license to archive, make accessible, and display my thesis or dissertation in whole or in part in all forms of media, now or hereafter known, including display on the world wide web. I understand that I may select some access restrictions as part of the online submission of this thesis or dissertation. I retain all ownership rights to the copyright of the thesis or dissertation. I also retain the right to use in future works (such as articles or books) all or part of this thesis or dissertation.

Signature

_____ _____

Hanchao Liu Date

Theoretical Studies of the Vibrational Spectra and Relaxation Dynamics of Ice and Water

By

Hanchao Liu
Doctor of Philosophy

Chemistry

Joel M. Bowman, Ph.D.
Adviser

Michael C. Heaven, Ph.D.
Committee Member

James T. Kindt, Ph.D.
Committee Member

Accepted:

Lisa A. Tedesco, Ph.D.
Dean of the James T. Laney School of Graduate Studies

Date

Theoretical Studies of the Vibrational Spectra and Relaxation Dynamics of Ice and Water

By

Hanchao Liu

B.S., Lanzhou University, 2010

Adviser: Joel M. Bowman Ph.D.

An Abstract of

A dissertation submitted to the Faculty of the

James T. Laney School of Graduate School of Emory University

in partial fulfillment of the requirements for the degree of

Doctor of Philosophy

in Chemistry

2015

Abstract

Theoretical Studies of the Vibrational Spectra and Relaxation Dynamics of Ice and Water

By Hanchao Liu

Recently, theoretical studies of condensed phase water have been advanced in two-fold, with the development of first the Wang-Huang-Braams-Bowman(WHBB) ab initio potential energy(PES) and dipole moment surfaces(DMS), and second the quantum Local-Monomer Model. The WHBB PES accurately describes the electronic energy of arbitrary number of water monomers using a many-body representation. The important intrinsic 2-body and 3-body interactions are permutationally invariant fits of tens of thousands ab initio energies. Very recently, a new dipole moment surface is reported using a spectroscopically accurate 1-body DMS and an intrinsic 2-body DMS fit. The quantum Local-Monomer Model uses a divide-and-conquer strategy and solves the Schrodinger equation for each water monomer embedded in its hydrated environment. This approach effectively reduces the formidable dimensionality of the condensed phase water to usually 3 to 6 and up to 9 degrees of freedom. The first half of the dissertation will review and formulate the WHBB PES and DMS and the Local-Monomer Model.

In the second half of the dissertation, we take advantage of this recent theoretical advancement and report several fully ab initio quantum studies of the vibrational spectra and dynamics of ice, liquid water and water hexamer. The topics include the infrared spectra of ice Ih and amorphous ice, vibrational density of states of neat and deuterated ice Ih and vibrational energy relaxation dynamics of HOD diluted ice, the infrared spectra of liquid water, and the infrared spectra and harmonic zero-point energies of HOD doped water hexamers.

Theoretical Studies of the Vibrational Spectra and Relaxation Dynamics of Ice and Water

By

Hanchao Liu

B.S., Lanzhou University, 2010

Adviser: Joel M. Bowman Ph.D.

A dissertation submitted to the Faculty of the
James T. Laney School of Graduate School of Emory University
in partial fulfillment of the requirements for the degree of
Doctor of Philosophy
in Chemistry
2015

Acknowledgement

I want to deliver my appreciation to many people. Without them, finishing this dissertation would not be possible.

First of all, I want to thank my adviser, Prof. Joel M. Bowman, for his patient guidance and continuous supports throughout my Ph.D. years. Under his tutelage, I not only become a better thinker, writer and presenter, but also learn how to appreciate and pursuit good science. I also want to thanks my other committee members, Prof. Michael C. heaven and Prof. James T. Kindt for their helpful suggestions. I want to thank Dr. Stuart Carter, Dr. Yimin Wang and Dr. Xinchuan Huang for their patient guidance on MULTIMODE and the potential energy surfaces.

I also want to deliver my appreciation to the current and past members of the Bowman's group whom I shared office with, Chen Qu, Xiaohong Wang, Dr. John Mancini, Dr. Yimin Wang, Dr. Riccardo Conte, Dr. Zahra Homayoon, Dr. Gabor Czako, Dr. Antonio de Oliveira Filho, Dr. Yongchang Han, Dr. Bina Fu, Dr. Eugene Kamarchik, Dr. Chao Chen, for countless helpful discussions and encouragements.

Last but not least, I want to thank my mother Hong for her love and support. I also want to thank Ann Dasher and Susan Browne for all the coordination work.

Table of Contents

List of Tables

Table 6.3. Harmonic zero-point energy (ZPE) and ΔZPE, relative to cage $(D_2O)_6$, of the twelve $HOD(D_2O)_5$ isotopomers of the cage hexamer. The site labels are given in Figure 6.1. The harmonic frequency for each OH is also shown.

Table 6.4. Harmonic zero-point energies (ZPE) and ΔZPE, relative to prism $(D_2O)_6$, of the twelve $HOD(D_2O)_5$ isotopomers of the prism hexamer. The site labels are given in Figure 6.1. The harmonic frequency for each OH is also shown.

List of Figures

results of LMon-4 calculations (black), MQC line shape (gray), and VDOS (gray dotted). The panels correspond, from top to bottom, to liquid water at 600 K, liquid water at 300 K, and ice Ih at 150 K. The integrated intensity of the OH stretch peak has been normalized to the same area.

Figure 3.3. Infra-red absorption spectrum of H_2O at three different thermodynamic conditions. From top to bottom: (compressed) liquid water at 600 K, liquid water at 300 K and ice Ih at 150 K. The curves correspond to TRPMD (blue), CMD (red), and LMon-4 calculations (black). Note in the middle panel the reduced red shift of the OH peak in CMD compared with the results in Ref. 22.

Figure 4.1. Local Minima structures of hexagonal and amorphous $(H_2O)_{192}$. The illustrative frames show the interior 105 and 100 core monomers selected in the hexagonal and amorphous clusters, respectively.

Figure 4.2. IR spectra of intramolecular bend modes of surface hexagonal ice. a) Local-monomer calculation for 87 monomers on the surface of 192-mer cluster. b) Experimental surface spectra in the bending region of crystalline ice at 120 K. (Ref. 42).

Figure 4.3. Total, surface and core smoothed IR spectra in the OH-stretching region of hexagonal 192-mer.

Figure 4.4. IR spectra in the OH-stretch region. (a) Theory. (b) Experimental crystalline ice at 16 K (Ref 3). (c) Experimental Ice Ih at 100K (Ref 2). (d) Theory (e) Experiment at 16K (Ref 3). (f) Experiment at 20 K (Ref 5). Blue solid lines in panels (a) and (d) are the calculated spectra with inclusion of the bending overtone. Red dashed lines are calculated spectra without the bending overtone. Black curves are experimental spectra.

Figure 4.5. Vibrational density of states of H_2O and D_2O ice Ih in the range 0–4200 cm^{-1}: calculated 192-mer (solid green curves), calculated core 105-mer (solid red curves), and experimental inelastic neutron scattering digitized from figure 2 of reference 10 (dashed curves). The 192-mer and experimental intensity is normalized to unity. The intensity of core 105-mer is in the same scale of the

192-mer.

Figure 4.6. Vibrational density of states of H_2O and D_2O ice Ih in the range 1000–4200 cm^{-1}: calculated harmonic and local-monomer from the core 105-mer (solid curves) and experimental inelastic neutron scattering (dashed curves). INS data are digitized from reference 10. H_2O is from Figure 6, D_2O is from Figure 10 with H_2O < 0.5%. Some small peaks in this spectrum are due to this H_2O contamination. Each curve is normalized to one at the maximum intensity.

Figure 4.7. Visualization of four eigenvectors from the core-105mer. (representative 6-member rings are shown) (a) Acoustic "translational" mode at 67 cm^{-1}, (b) Optical "translational" mode at 229 cm^{-1}, (c) Optical "translational" mode at 314 cm^{-1}, (d) Librating mode at 662 cm^{-1}

Figure 4.8. Fraction of mass-weighted normal mode eigenvectors projections on O and H (D) atoms for the core 105-mers as function of the corresponding harmonic frequency.

Figure 4.9. Depiction of all local-normal modes of the HOD monomer in ice environment. Abbreviation at top. Full description and harmonic frequency at bottom.

Figure 4.10. Time-dependent populations of the four excited non-stationary states and major population receivers. (a) OD fundamental (b) OH fundamental (c) OD overtone (d) OH overtone.

Figure 5.1. Harmonic vibrational density of states from normal mode analysis of the core 100-mer, and from local normal mode analysis of the 100 monomers. States are summed from 10 snapshots, as described in the text. For graphical purposes, imaginary frequencies are shown as negative numbers.

Figure 5.2. Depiction of the 9 lormal modes and frequencies of an example monomer.

Figure 5.3. Thermally averaged LMon-4 IR spectra of liquid water at 300K using WHBB potential and the new DMS. The experimental spectrum is from ref 1.

Figure 5.4. LMon-4 spectra containing transitions only from the ground state using

WHBB (with the new DMS), q-TIP4P/F and TTM3-F PESs and DMSs. The experimental spectrum is from ref 1.

Figure 5.5. Deconstruction of spectral bands, see text for more details.

Figure 5.6. IR spectra of 9 snapshots. The interval is 30 ps. Each spectrum is obtained in the same way as the one in Figure 5.4a with a FWHM of 70 cm^{-1}.

Figure 6.1. Structure and atom numbering for the cage (top) and prism (bottom) isomers of water hexamer.

Figure 6.2. IR spectra of cage $HOD(D_2O)_5$

Figure 6.3. IR spectra of prism $HOD(D_2O)_5$

Figure 6.4. OH stretch band of IR spectra of the cage and prism $HOD(D_2O)_5$.

Copyrights and Permissions

"Quantum Calculations of Intramolecular IR Spectra of Ice Models Using Ab Initio Potential and Dipole Moment Surfaces", H. Liu, Y. Wang and J. M. Bowman, J. Phys. Chem. Lett. **3**, 3671 (2012).

"Vibrational Analysis of an Ice Ih Model from 0 to 4000 cm^{-1} Using the Ab Initio WHBB Potential Energy Surface", H. Liu, Y. Wang and J. M. Bowman, J. Phys. Chem. B **117**, 10046 (2013).

"Ab Initio Deconstruction of the Vibrational Relaxation Pathways of Dilute HOD in Ice Ih", H. Liu, Y. Wang and J. M. Bowman, J. Am. Chem. Soc. **136**, 5888 (2014).

Chapter 5 uses contents from

"Quantum Calculations of the IR spectrum of Liquid Water Using *Ab Initio* and Model Potential and Dipole Moment Surfaces and Comparison with Experiment", H. Liu, Y. Wang and J. M. Bowman, J. Chem. Phys. **142**, 194502 (2015).

Chapter 6 uses contents from

"Local-Monomer Calculations of the Intramolecular IR Spectra of the Cage and Prism Isomers of $HOD(D_2O)_5$ and HOD and D_2O Ice Ih", H. Liu, Y. Wang and J. M. Bowman, J. Phys. Chem. B **118**, 14124 (2014).

Dedicated to my dear mother Hong

Chapter 1.

Introduction

Water is one of the most important substances on earth for enabling many geological and climate processes, sustaining life and civilizing human beings. Although everyone acknowledges the importance of water, no one really understands it. The evidence is that water has so many, the so-called anomalous behaviors.[1-2] For example, its density peaks at 4 C rather than continues to decrease as the temperature drops. It is able to carry huge amount of heat. It has unusual high surface tension. When freezing, it expands.

One unique feature of water is its complicated hydrogen bond networks. The traditional picture is that each water monomer is bounded to four others in tetrahedral arrangement, by donating two and accepting two hydrogen atoms. In liquid phase, this network constantly rearranges. This picture is supported by the neutron-scattering experiments and theoretical studies.[3] The structure of the H-bond network has been a frequently debated topic.[4-5] In 2004, studies using X-ray absorption spectroscopy suggest that at room temperature, only 20% of liquid water molecules are bounded by four H-bonds, whereas the remaining water

molecules has one strong and one weak H-bonds.[4] This was later disputed as an instantaneous effect and the long timescale picture is still compatible with the tetrahedral H-bonded liquid.[5]

The solid form of water, ice is perhaps even more complicated than the liquid form. On the phase diagram, at least 15 phases can be found.[6] Some of them exist on earth or in the space, whereas others are only made in lab. They differ mostly by its lattice type and hydrogen arrangement. For example, the hexagonal ice (ice Ih) is a hexagonal crystal with disordered proton arrangement. They are found in snow and ice on earth. If the protons in ice Ih are in order, the ice is the ice XI. There are at least three types of amorphous ice, low-density amorphous ice, high-density amorphous ice and very-high density amorphous ice.[7]

The structure, absorption and dynamics of water and ice attract many experimental studies, mostly by various spectroscopic and scattering techniques. Perhaps the most widely used one is the infrared spectra. The IR spectra have been collected for from small water clusters to liquid and various phases of ice.[8-9] Because the absorption features, e.g. the band frequency, are very sensitive to the structure, IR spectra is very useful to determine the phases of ice.[8] Raman spectra are also used to complement the IR spectra.[10] X-ray absorption spectra help interpretation the structures of the H-bond networks.[4] Inelastic neutron scattering experiments provide the vibrational density of states.[11-12] Time-resolved pump and probe

spectroscopy is very useful to study the dynamics of water and ice, for example, the vibrational relaxation and the H-bond reorientation.[13-14] Recently, the 2D-IR and 3D-IR spectroscopy are utilized to quantify the vibrational relaxation time.[15-16] The sum frequency generation spectra can give insights to the surface.[17] High-resolution rotational spectra have been used to characterize the low-lying isomers of water hexamer.[18]

Many theoretical studies have been performed in order to understand water and ice. The Born-Oppenheimer approximation allows the electronic and nuclear degrees of freedom to be treated separately; nonetheless, each part is very challenging. The first challenge is to describe the electronic energy in water. Modeling water is a huge topic in literature; there are many models developed from the simple fixed point-charge models to ab initio potential energy surfaces.

The simple, fixed point-charge models, such as SPC or TIP4P,[19] are popular in the field of water and hydration simulation. Originally in these models, fixed point-charges are placed on several sites of a rigid monomer. For example, in the TIP4P model, two positive point charges are on the two hydrogen atoms and a negative charge is on a virtual site M. With these point charges, monomers interact via pairwise Coulomb and Lennard-Jones potentials.

$$V = \sum_i \sum_{j>i} (4\varepsilon[(\frac{\sigma}{r_{ij}})^{12} - (\frac{\sigma}{r_{ij}})^6] + \sum_{m\in i} \sum_{n\in j} \frac{q_m q_n}{r_{mn}})$$

The simple function form of the TIP4P model makes it very efficient. It has been

implemented in many popular software suits, e.g. GROMACS,[20] and it is widely used in water and hydration simulation. Subsequent reparametrizations have been done for specific uses. For example, TIP4P-Ew model[21] is for Ewald summation methods, and TIP4P/Ice[22] is for ice simulations. TIP4P/2005 is designed for all phases of bulk water.[23]

One issue with the fixed point-charge models is that the monomers are rigid; therefore it cannot be used to study the intramolecular vibration and IR spectra. Efforts have been made to incorporate simple intramolecular potentials.[17, flexible tip4p] Examples of such extension include q-SPC/Fw[24] and q-TIP4P/F.[25] The former installs a harmonic potential into the SPC model. The latter adds Morse potentials for the OH stretch and harmonic potential for the monomer bend, as described by the following equation,

$$V_{monomer} = \sum_i \left[V_{OH}(r_{i1}) + V_{OH}(r_{i2}) + \frac{1}{2} k_\theta (\theta_i - \theta_{eq})^2 \right]$$

where

$$V_{OH}(r) = D_r \left[\alpha^2 (r - r_{eq})^2 - \alpha^3 (r - r_{eq})^3 + \frac{7}{12} \alpha^4 (r - r_{eq})^4 \right]$$

The q-TIP4P/F model has been used to calculate the water IR spectra using RPMD, CMD.[25] Recently, it has been used in a joint study comparing several dyanmics method including Local-Monomer, CMD, TRPMD.[26] The above studies show that this model is unable to predict correct IR intensity.[25-27] As shown recently,[27] this is because the fixed point-charge models are unable to predict

correct dipole derivatives for the OH stretch modes; at least the 2-body dipole terms are needed to obtain the correct derivatives. The other major issue for the fixed point-charge models is that they miss the 3-body interactions, which have been shown contributing about 20% of the total binding energy of water clusters and bulk water and ice.[28] It is clear that the fixed point-charge models over simplified the complicated physics of water and one needs to go beyond that for more accurate water simulations. Another evidence for this is that the TIP4P model fails to accurately predict many important properties of water. For example, the TIP4P model predicts the peak density of water at -25C.[29]

One direction that the field has headed is to include polarizability. One important example of these approaches is the TTM3-F water model.[30] In this model, the monomer potential is taken from the spectroscopically accurate Patridge-Schwenke one.[31] The pairwise interaction is describe by the Buckingham exponential-6 potential. The parameters are optimized against the MP2/aVDZ binding energies and the harmonic frequencies of water cluster from trimer to the 20-mer, and several other experimental properties of ice. Polarizable electrostatic interactions are included using this effective density

$$\rho(r) = \frac{1}{\tilde{A}^3}\frac{3a_s}{4\pi}e^{-a_s(\frac{r}{\tilde{A}})^3}$$

where $\tilde{A} = (a_i a_j)^{1/6}$ is the polarizability tensor.

TTM3-F is a successful semi-empirical model as it improves the accuracy over

the fixed point-charge models. A drawback of TTM3-F is that it is parametrized against classical MD simulations and IR spectra; therefore the peak positions from this model suffers from systematic blue-shifts. Due to the iterative induction scheme built in this model, it can be fairly computationally demanding when dealing with large-size systems.

Other efforts have been made to incorporate the important 3-body effects by adding an empirical rigid model of such effects. This is in the E3B potential developed by Skinner's group.[32-33] This model was parametrized to fit a serials of experimental properties such as the OO radial distribution functions, diffusion constant, rotational correlation time, liquid and ice density, surface tension and melting point. The function form of this 3b potential is an exponential one of the sum of two H-bond distances in each of the three scenarios of the 3b interactions due to the H-bond network arrangement, according to their classification. An example of one such term is showed as follow,

$$f(r_1, r_2) = E_A e^{-k(r_1+r_2)}$$

The E3B model has been applied in various water and ice studies, usually combined with classical MD simulations and the 1-dimensional local-mode model.[34-35] The applications include the IR spectra of ice[34] and the H-bond switching dynamics.[35]

Distinct from the above empirical or semi-empirical models, an ab initio potential energy surface has recently been reported,[36] which is based on the

many-body representation of the total potential energy of arbitrary number of water monomers

$$E = \sum_{i}^{N} V_{1-body}(i) + \sum_{i<j}^{N} V_{2-body}(i,j) + \sum_{i<j<k}^{N} V_{3-body}(i,j,k) + \sum_{n\geq 4}^{N} V_{n-body}$$

The 1-body potential uses a spectroscopically accurate one.[31] The intrinsic 2-body potential is a permutationally invariant fit of roughly 30 000 CCSD(T)/aVTZ data. The intrinsic 3-body potential is a permutationally invariant fit of roughly 40 000 MP2/aVTZ data. The 4- and higher-body terms are polarization energies borrowed from the TTM3-F potential. Denoted as WHBB water PES, it has been tested and applied for many water calculations, including the successful prediction of D_e for up to water 22-mer,[36] and D_0 of the water dimer and trimer and several low-lying water hexamers.[37-39] The PES has been used to calculate the IR spectra from water dimer up to an ice model consisting about 200-mer, along with the ab initio WHBB dipole moment surface.[40-42] The PES has also been applied to successfully predict the vibrational density of states of neat and deuterated Ih.[43] It has also been applied to study the vibrational energy relaxation processes for the dilute HOD monomers in the H_2O/D_2O ice, and provided accurate relaxation lifetime and detailed mechanisms.[44] Another ab initio many-body PES is the MB-pol PES. This one follows the WHBB PES, but with polarization terms included.[45-46]

Electronic properties are also important for water simulations. Some most relevant properties are dipole moment, polarizability and susceptibility. Perhaps the

majority of efforts have been spent on the dipole moment due to the prevalent use of IR spectra in both experimental and theoretical studies.[25,30,36] The simplest model is a fixed dipole moment, which is derived from the rigid fixed point-charge models. This is obviously unable to describe the IR spectra. Beyond that is the linear dipole from the flexible fixed point-charge models, such as the q-TIP4P/F model. The linear dipole has been used to simulate liquid water IR spectra.[25-27] The issue is that it significantly underestimates the intensity of OH stretch, therefore predicts qualitatively incorrect bend/stretch bands ratio. As pointed our recently, because of the strong effect of polarization and possible partial charge transfer in the complicated H-bond network in condensed-phase water, at least the 2-body dipole moment is needed to account for such effects. Therefore it is not very surprising that the linear dipole moment model fails to predict the correct IR intensity.

The TTM3-F dipole model[31] uses empirical approaches to fix the above issue by inserting artificial terms to mimic the charge transfer as the OH bond elongates along the H-bond. This approach improves the IR intensity liquid water, although in a heuristically way. The fully ab initio approach to describe the dipole moment of arbitrary water monomers has been reported along with the WHBB PES in 2011.[36] Like the PES, it uses a many-body representation of the dipole moment and it is truncated at the 2-body terms. To our knowledge this was the first time the dipole moment is described in this way. The DMS has been successful in describing the

static dipole of a series of small water clusters, and IR spectra up to 200-mer. Later the ab initio DMS has been improved by introducing an intrinsic fit of the 2-body dipole. The new DMS is very successful for liquid water IR spectra. Other ab initio DMS includes the MB-mu, which closely follows the WHBB DMS.[47]

The nuclear dynamics of condensed-phase water is perhaps even more challenging than the electronic structure calculations, due to the huge degrees of freedom. Classical MD simulation is very efficient and can be done for large systems with a empirical force field; therefore it has been used to study a wide range of topics including the phase transition,[48] vibrational spectra[49] and vibrational energy relaxations.[50-52] However, the classical MD simulation misses the quantum effects such as the zero-point energy and tunneling. To incorporate the quantum effects, many semi-classical[53,54] and approximate quantum methods have been developed. The approximate quantum methods include two types. The first type is the path-integral inspired molecular methods, such as centroid molecular dynamics (CMD) and ring-polymer molecular dynamics (RPMD).[25,26,55-57] These methods treat all the degrees of freedom in the same footing but in an approximate way. The second type is reduced dimensional quantum methods, which treats a subset of the degree of freedom exactly. Examples include the one-dimensional local-mode methods[58-61] and the Local-Monomer Model.[62] A review of these methods will be given in Chapter 3.

In this dissertation, a number of studies on water and ice will be presented. Quantum effects are considered for both the electronic and nuclear degrees of freedom, by using the ab initio potential and dipole moment surfaces, and the quantum Local-Monomer approach. The dissertation is organized as follow.

Chapter 2 summarizes the WHBB ab initio potential energy and dipole moment surfaces recently developed by our group, and presents a new dipole moment surface with test results. Chapter 3 presents the theories for the quantum Local-Monomer model, including the basic LMon-3 and the extended LMon-4 and LMon-6. A comparison of the LMon model with other popular dynamics methods in computing the IR spectra for water is also shown. Chapter 4 focuses on the vibrational spectra and relaxation dynamics of ice. The IR spectra of ice Ih and amorphous ice are presented, followed by the vibrational density of states of ice Ih. The vibrational energy relaxation dynamics of dilute HOD in ice Ih is discussed at the end of Chapter 4. In Chapter 5, the infrared spectrum of liquid water is discussed. Chapter 6 focuses on IR spectra of HOD doped water hexamer.

References

1. P. Ball, Nature **452**, 291 (2008).
2. I. Brovchenko and A. Oleinikova, Chemphyschem 9, 2660 (2008).
3. F. Franks, Water: A Comprehensive Treatise Vol. 1 (Plenum Press, New York, 1975).
4. P. Wernet, D. Nordlund, U. Bergmann, M. Cavalleri, M. Odelius, H. Ogasawara, L. Å. Näslund, T. K. Hirsch, L. Ojamäe, P. Glatzel, L. G. M. Pettersson and A. Nilsson, Science 304 995 (2004).
5. T. Head-Gordon and M. E. Johnson, Proc. Nat. Acad. Sci. **103**, 7973 (2006).
6. T. Bartels-Rausch, V. Bergeron, J. H. E. Cartwright, R. Escribano, J. L. Finney, H. Grothe, P. J. Gutiérrez, J. Haapala, W. F. Kuhs, J. B. C. Pettersson, S. D. Price, C. I. Sainz-Díaz, D. J. Stokes, G. Strazzulla, E. S. Thomson, H. Trinks and N. Uras-Aytemiz, Rev. Mod. Phys. **84**, 885 (2012).
7. V. Velikov.; S. Borick; C.A. Angell. *Science* **294** (2001).
8. E. Whalley, Can. J. Chem. **55**, 3429 (1977).
9. J. E. Bertie and Z. Lan, App. Spectr. **50**, 1047 (1996).
10. T. Shigenari and K. Abe, J. Chem. Phys. **136**, 174504 (2012).
11. J. Li and D. K. Ross, Nature **365**, 327 (1993).
12. J. Li, J. Chem. Phys. **105**, 6733 (1996).

13. J. C. Deàk, S. T. Rhea, L. K. Iwaki and D. D. Dlott, J. Phys. Chem. A **104**, 4866 (2000).

14. A. M. Dokter and H. J. Bakker, J. Chem. Phys. **128**, 024502 (2008).

15. F. Perakis and P. Hamm, Phys. Chem. Chem. Phys. **14**, 6250 (2012).

16. F. Perakis, J. A. Borek and P. Hamm, J. Chem. Phys. **139**, 014501 (2013).

17. M. Vinaykin and A. V. Benderskii, J. Phys. Chem. Lett., 3348 (2012).

18. C. Perez, M. T. Muckle, D. P. Zaleski, N. A. Seifert, B. Temelso, G. C. Shields, Z. Kisiel and B. H. Pate, Science **336**, 897 (2012).

19. W. L. Jorgensen, J. Chandrasekhar, J. D. Madura, R. W. Impey and M. L. Klein, J. Chem. Phys. **79**, 926 (1983).

20. D. Van Der Spoel, E. Lindahl, B. Hess, G. Groenhof, A. E. Mark and H. J. C. Berendsen, J. Comput. Chem. **26**, 1701 (2005).

21. H. W. Horn, W. C. Swope, J. W. Pitera, J. D. Madura, T. J. Dick, G. L. Hura and T. Head-Gordon, J. Chem. Phys. **120**, 9665 (2004).

22. J. L. F. Abascal, E. Sanz, R. García Fernández and C. Vega, J. Chem. Phys. **122**, 234511 (2005).

23. J. L. F. Abascal and C. Vega, J. Chem. Phys. **123**, 234505 (2005).

24. S. Amira, D. Spångberg and K. Hermansson, Chem. Phys. **303**, 327 (2004).

25. S. Habershon, T. E. Markland and D. E. Manolopoulos, J. Chem. Phys. **131**, 024501 (2009).

26. M. Rossi, H. Liu, F. Paesani, J. Bowman and M. Ceriotti, J. Chem. Phys. **141**, 181101 (2014).

27. H. Liu, Y. Wang and J. M. Bowman, J. Chem. Phys. Submitted.

28. K. Szalewicz, C. Leforestier and A. van der Avoird, Chem. Phys. Lett. 482, 1 (2009).

29. M. W. Mahoney and W. L. Jorgensen, J. Chem. Phys. 112 (2000).

30. G. S. Fanourgakis and S. S. Xantheas, J. Chem. Phys. **128**, 074506 (2008).

31. H. Partridge and D. W. Schwenke, J. Chem. Phys. **106**, 4618 (1997).

32. C. J. Tainter, P. A. Pieniazek, Y.-S. Lin and J. L. Skinner, J. Chem. Phys. **134**, 184501 (2011).

33. C. J. Tainter, L. Shi and J. L. Skinner, J. Chem. Theory. Comput. (2015).

34. L. Shi and J. L. Skinner, J. Phys. Chem. B **117**, 15536 (2013).

35. Y. Ni, S. M. Gruenbaum and J. L. Skinner, Proc. Natl. Acad. Sci. USA **110**, 1992 (2013).

36. Y. Wang, X. Huang, B. C. Shepler, B. J. Braams and J. M. Bowman, J. Chem. Phys. **134**, 094509 (2011).

37. Y. Wang and J. M. Bowman, J. Chem. Phys. **135**, 131101 (2011).

38. L. C. Ch'ng, A. K. Samanta, Y. Wang, J. M. Bowman and H. Reisler, J. Phys. Chem. A **117**, 7207 (2013).

39. Y. Wang, V. Babin, J. M. Bowman and F. Paesani, J. Am. Chem. Soc. **134**, 11116 (2012).

40. H. Liu, Y. Wang and J. M. Bowman, J. Phys. Chem. B **117**, 10046 (2013).

41. H. Liu, Y. Wang and J. M. Bowman, J. Phys. Chem. **3**, 3671 (2012).

42. Y. Wang and J. M. Bowman, J. Phys. Chem. **4**, 1104 (2013).

43. J. M. Bowman, Y. Wang, H. Liu and J. S. Mancini, J. Phys. Chem. 366 (2015).

44. H. Liu, Y. Wang and J. M. Bowman, J. Am. Chem. Soc. **136**, 5888 (2014).

45. V. Babin, C. Leforestier and F. Paesani, J. Chem. Theory. Comput. **9**, 5395 (2013).

46. V. Babin, G. R. Medders and F. Paesani, J. Chem. Theory. Comput. **10**, 1599 (2014).

47. G. R. Medders and F. Paesani, J. Chem. Theory. Comput. **11**, 1145 (2015).

48. M. Matsumoto, S. Saito and I. Ohmine, Nature **416**, 409 (2002).

49. H. Ahlborn, X. Ji, B. Space and P. B. Moore, J. Chem. Phys. **111**, 10622 (1999).

50. R. Rey and J. T. Hynes, J. Chem. Phys. **104**, 2356 (1996).

51. R. Rey, K. B. Møller and J. T. Hynes, Chem. Rev. **104**, 1915 (2004).

52. C. P. Lawrence and J. L. Skinner, J. Chem. Phys. **117**, 5827 (2002); **119**, 1623 (2003); **119**, 3840 (2003).

53. J. Liu, W. H. Miller, F. Paesani, W. Zhang and D. A. Case, J. Chem. Phys. **131**, 164509 (2009).

54. J. Liu, W. H. Miller, G. S. Fanourgakis, S. S. Xantheas, S. Imoto and S. Saito, J. Chem. Phys. **135**, 244503 (2011).

55. S. Habershon, G. S. Fanourgakis and D. E. Manolopoulos, J. Chem. Phys. **129**, 074501 (2008).

56. F. Paesani, S. S. Xantheas and G. A. Voth, J. Phys. Chem. B **113**, 13118 (2009).

57. F. Paesani and G. A. Voth, J. Chem. Phys. **132**, 014105 (2010).

58. A. C. Belch and S. A. Rice, J. Chem. Phys. **78**, 4817 (1983).

59. V. Buch, J. Phys. Chem. B **109**, 17771 (2005).

60. H. Torii, J. Phys. Chem. A **110**, 9469 (2006).

61. B. Auer, R. Kumar, J. R. Schmidt and J. L. Skinner, Proc. Natl. Acad. Sci. USA **104**, 14215 (2007).

62. Y. Wang and J. M. Bowman, J. Chem. Phys. **134**, 154510 (2011).

Chapter 2.

Ab Initio Potential Energy and Dipole Moment Surfaces

2.1. Potential Energy Surface

As describe in detailed in Ref 1, the WHBB PES can describe arbitrary number of water monomers using the following many-body representation

$$E = \sum_{i}^{N} V_{1-body}(i) + \sum_{i<j}^{N} V_{2-body}(i,j) + \sum_{i<j<k}^{N} V_{3-body}(i,j,k) + \sum_{n\geq 4}^{N} V_{n-body}$$

Here the 1-body terms are the monomer potential energies. The 2-body, 3-body and n-body terms are the intrinsic many-body energies. This representation for the potential had been shown previous to our work to be well-converged for moderate-sized clusters at the 3-body level.[1] The convergence of this representation of the electronic potential continues to be investigated for ever-larger clusters, where of course the number of 4, 5 and higher body interactions increases.[2-4]

The 1-body potential uses a spectroscopically accurate monomer potential due to Patridge and Schwenke (PS).[5] Using this PES, the calculated fundamentals transitions of a single water molecule are within 1 cm^{-1} to the experiment.[5]

An intrinsic 2-body interaction energy term is defines as

$$V_{2-body}(1,2) = V_{Dimer}(1,2) - V_{Monomer}(1) - V_{Monomer}(2)$$

Using this expression, the intrinsic 2-body energies are computed at the level of CCSD(T)/aVTZ. Roughly 30 000 ab initio energies are computed and used for fitting an analytical potential energy function. The fitting basis is same set as for the previous HBB2 dimer PES,[6] up to seven degrees of permutationally invariant polynomials of Morse variables $\exp(-r_{ij}/\lambda)$, where λ is fixed at 3.0 Bohrs and r_{ij} is the internulcear distance of atom i and j. Detailed fitting procedures are described in Ref.[7] The ab initio PES switches to the TTM3-F PES[8] when the dimer OO distance is longer than 6.5 Angstrom, in order to not only enforce the physically correct long range behaviors but also to accelerate the computational speed.[1]

The PES for intrinsic 3-body energies are built by fitting roughly 40 000 MP2/aVTZ ab initio points. The permutationally invariant polynomials basis is used as for the 2-body PES. Two sets of fitting are done, using the 5-th order and the 6-th order polynomials. For all applications of this dissertation, the 5-th order fit is used.

The 4- and higher-body terms are polarization induced interactions, borrowed from the TTM3-F potential.[8] These terms are not used in the calculations for ice and liquid water because these take huge computational efforts. These terms are used for all hexamer calculations, to be consistent with previous calculations on the same systems.[9,10]

The WHBB PES has been tested and applied in many studies. These include the successful prediction of D_e for up to water 22-mer,[1] and D_0 of the water dimer and trimer.[11,12] The ZPE-corrected most stable isomers of water hexamer are predicted using the PES and Diffusion Monte-Carlo calculations.[9] The PES has been used to calculate the IR spectra from water dimer up to an ice model consisting about 200-mer, along with the ab initio WHBB dipole moment surface.[13-15] It has recently been used for liquid water IR spectra at 300 K.[16] The PES has also been applied to successfully predict the vibrational density of states of neat and deuterate Ih.[17] It has also been applied to study the vibrational energy relaxation processes for the dilute HOD monomers in the H_2O/D_2O ice, and provided accurate relaxation lifetime and detailed mechanisms.[18] Recently the intrinsic 2-body and/or 3-body water PESs are transferred as part of the many-body PESs of several hydrated systems, e.g. mixed HCl-H_2O clusters, and successfully used for structure prediction and frequency calculations.[19]

2.2. Dipole Moment Surface

2.2.1. The WHBB Dipole Moment Surface

In the WHBB software, like the potential energy, the dipole moment of N H_2O monomers are represented using a many-body expansion. The many-body

representation of the dipole moment has not been extensively investigated. To the best of our knowledge this was first done, by Wang *et al*,[1] who proposed a 1 and 2-body representation.[1] Specifically, for *N* monomers the total dipole moment $\boldsymbol{\mu}$ is given by

$$\boldsymbol{\mu} = \sum_{i=1}^{N} \boldsymbol{\mu}_{monomer}(i) + \sum_{i \neq j}^{N} \boldsymbol{\mu}_{2-body}(i,j) \quad , \tag{1}$$

where the first (vector) summation is just the sum of 1-body, i.e., isolated gas-phase, dipole moments and the second summation is of intrinsic 2-body dipole moments. The latter is obtained from the equation,

$$\boldsymbol{\mu}_{2-body}(i,j) = \boldsymbol{\mu}_{dimer}(i,j) - \boldsymbol{\mu}_{monomer}(i) - \boldsymbol{\mu}_{monomer}(j), \tag{2}$$

where $\boldsymbol{\mu}_{dimer}(i,j)$ is the dipole moment of the dimer pair *i*, *j*. Clearly from this expression $\boldsymbol{\mu}_{2-body}(i,j)$ goes to zero as the dimer pair separate to infinite distance. As noted in the Introduction, the procedure followed in WHHB was first to fit $\boldsymbol{\mu}_{dimer}(i,j)$ to a set of roughly 30 000 MP2/aug-cc-pVTZ (aVTZ) dipole moments obtained over a large range of distorted monomer configurations and OO distances.

$$\boldsymbol{\mu}_{dimer} = \sum_{i=1}^{6} q_i(\{\boldsymbol{y}\})\boldsymbol{r}_i \quad , \tag{3}$$

where the summation is over the six atoms in the water dimer, and {*y*} represents the set of 12 "Morse" variables, y_{ij}, which are defined by $\exp(-r_{ij}/\lambda)$, where r_{ij} is the internuclear distance between atoms *i* and *j* and λ is a range parameter, typically set to 2 bohr. The effective charges q_i are determined by standard least-squares fitting to the data set of dipole moments and they are, like the potential, functions of

all the variables y_{ij}. Note the invariance under permutation in this case is different from the potential energy surface. To see this, consider a single monomer and a permutation of the two H atoms. The dipole moment transforms covariantly under this permutation, the effective charges on the two H atoms interchange; however, the charge on O atom is invariant under this permutation. This property of the dipole moment has been incorporated into the fitting routines.[1] Given that the dimer dipole moment has been precisely fit the monomer dipoles were obtained from the fit and were shown to represent the monomer dipole moment at the MP2/aVTZ level of theory. Further, the 1 and 2-body representation of the dipole moment was tested for a number of water clusters ranging in size from to the hexamer to the 20-mer and shown to be accurate to within less than 10% of directly calculated *ab initio* results.[1] This 1-body and 2-body dipole representation has also been shown to be accurate for other hydrated clusters.[20]

2.2.2. The New Dipole Moment Surface

Clearly, just the intrinsic 2-body dipole can be fit and combined with a highly accurate monomer dipole moment surface, exactly in the spirit of representing the potential, where the spectroscopically accurate monomer potential[1] is used. We take this approach for the new dipole moment surface here. Specifically, a new fit to the intrinsic 2-body dipole was done using the previous dataset of roughly 30 000

configurations and dimer MP2/aVTZ dipole moments. At each configuration new MP2/aVTZ calculations of the two 1-body dipole moments were done and then used in Eq. (2) to obtain the intrinsic 2-body dipole. Those data were fit using the approach briefly reviewed above using polynomials with maximum order of five. The RMS fitting error is a few hundreths of a Debye. A cut-off function is used in the range of 6.5-7.5 Angstrom of the O-O distance. As we will show later, the dipole moment is very small beyond this range.

Table 2.1. Double-harmonic IR frequencies and intensities for an isolated H_2O from the LTP2011 dipole moment surface[21] and directly from MP2/aVTZ calculations. For consistency, the normal mode analysis is done at MP2/aVTZ level.

mode	cm^{-1}	intensity (km/mol)	
		LTP2011	MP2/aVTZ
bend	1628	72	72
symm stretch	3822	3.5	5.6
asymm stretch	3948	57	75

For the 1-body dipole surface, we use the highly accurate one of Tennyson and co-workers,[21] denoted LTP2011, hereafter by “LTP”. This dipole moment surface is a precise fit to a dipole moment obtained using all-electron, internally contracted

multireference configuration interaction, including size-extensivity corrections in the aug-cc-pCV6Z basis set done at 2628 nuclear configurations. The decision to use this DMS is sensible in general terms, however, it was also made more compelling by making a comparison of the IR intensities of isolated water using it and directly from MP2/aVTZ theory. The comparison is shown in Table 2.1, and for simplicity using the double harmonic approximation. As seen, there is very good agreement for the bend but roughly 20% disagreement for the symmetric and anti-symmetric stretches. This absolute level of disagreement is not severe in our opinion, however, the unbalanced level of accuracy of MP2/aVTZ for the bend and the stretches is a concern, as these band intensities are of major interest for the IR spectra of liquid water and ice(s).

A detailed examination of this new DMS for water is given next. Since it consists of a very accurate 1-body dipole surface plus a 2-body one based on MP2/aVTZ it is not obvious how accurate the sum of these components is. That will be assessed below; however, the expectation is that the sum, which hereafter we will sometimes denote by DMS(1b-LTP,2b-MP2) for clarity or just DMS, should be more accurate than the previous WHBB fit to the full MP2/aVTZ dipole moment.

2.2.3. Tests of the New DMS

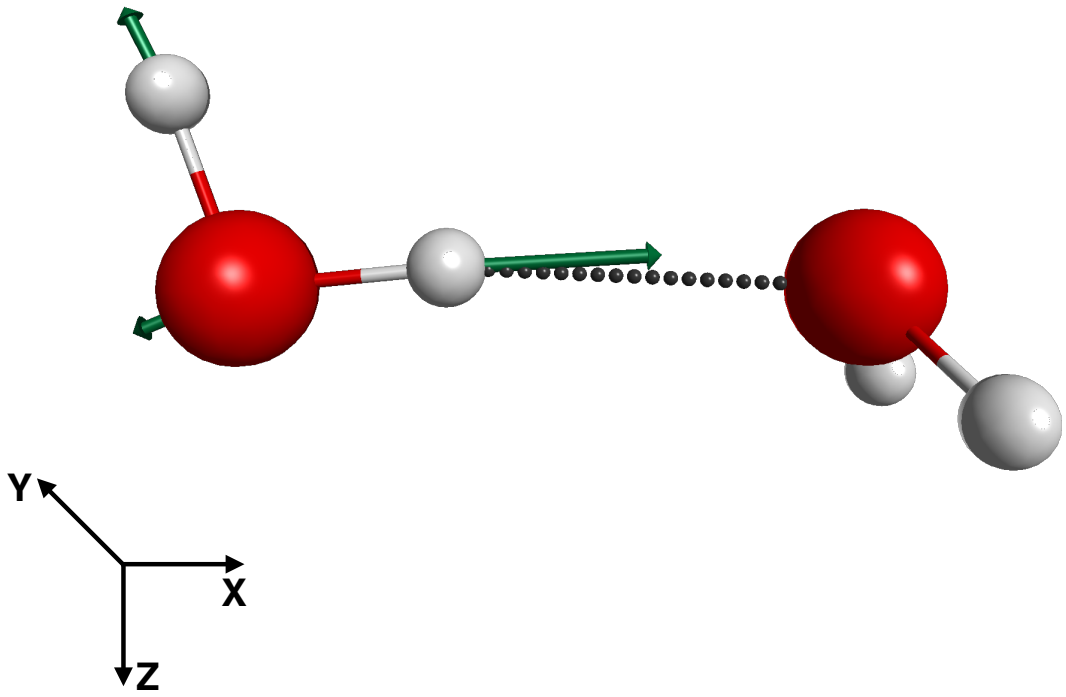

Figure 2.1. The water dimer at the global minimum. The monomer on the left is the H-bond donor and the monomer on the right is the H-bond acceptor. The H-bonded OH stretch local normal mode of the donor is shown in this figure.

We begin by assessing the accuracy of the intrinsic MP2/aVTZ 2-body dipole moment and also the precision of the fit to it. This is seen in Figure 2.2 where the 2-body dipole moment from direct MP2/aVTZ, CCSD(T)/aVTZ and the new fit are plotted versus the OO distance, with the internal configurations of the two monomers fixed at the global minimum structure (cf. Figure 2.1). As seen, there is excellent agreement, both for the MP2/aVTZ and the fitted dipoles, with the more

accurate CCSD(T)/aVTZ result. It is important to note that this excellent agreement between the MP2, the fit and CCSD(T) 2-b dipole moments does not imply that the full MP2/aVTZ dipole moment is in equally good agreement with the CCSD(T) one; it is not. However, that the MP2/aVTZ 2-body intrinsic dipole moment agrees well with the CCSD(T)/aVTZ one is not surprising (at least to us), as this is a difference quantity, see Eq. (2). As seen the 2-body DMS fit is quite precise. So, these results are quite encouraging because the full DMS(1b-LTP,2b-MP2) contains a highly accurate 1-body term and as shown in Figure 2.2 an accurate 2-body term as well. As expected, the intrinsic 2-body dipole decays to zero, albeit at fairly large OO distance of roughly 7 A. Note at the water dimer minimum, R_{OO} equals 2.92 A and there the 2-b dipole moment is roughly 0.5 D and displays a large increase with decreasing OO distance.

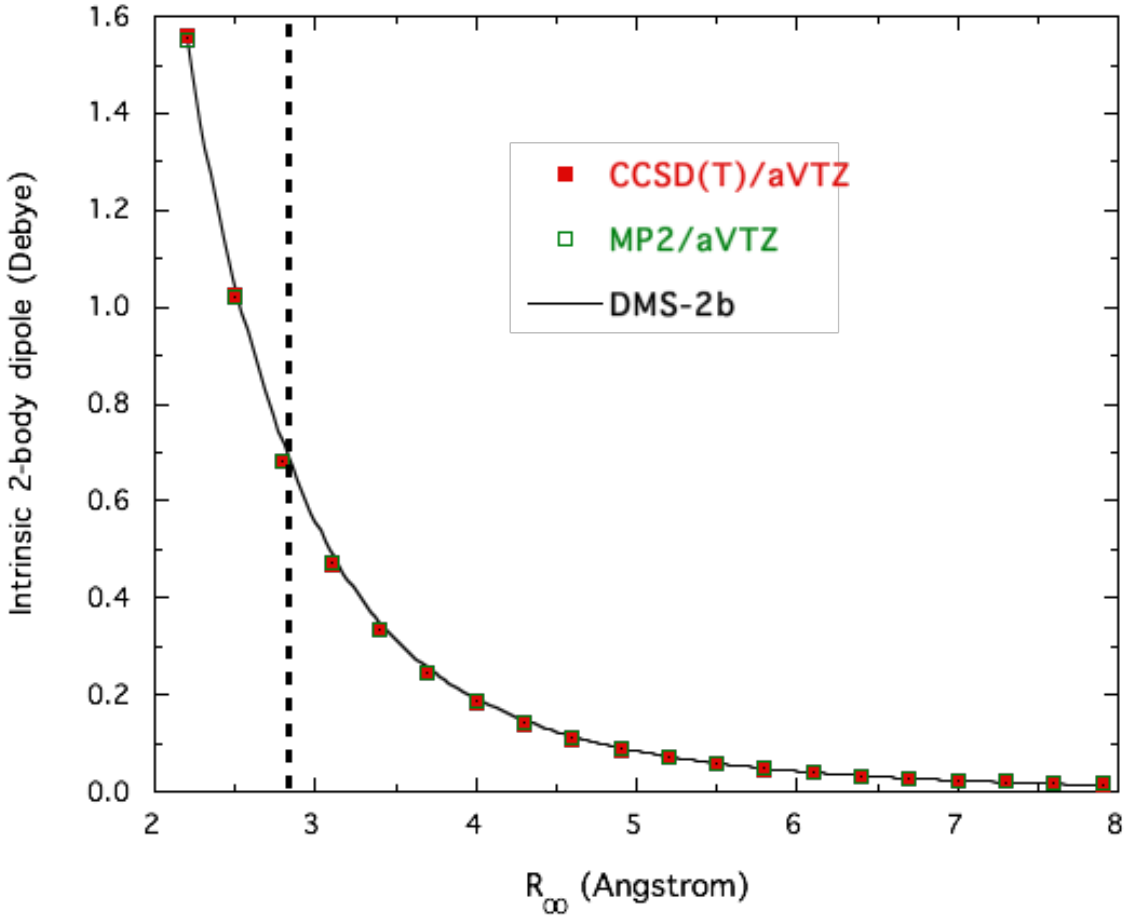

Figure 2.2. Intrinsic 2-body dipole magnitude from indicated sources for the water dimer as a function of the OO distance, with the monomers fixed at their internal structures at the dimer global minimum, shown in Figure 2.1. The dashed vertical line indicates the global minimum value of R_{oo}.

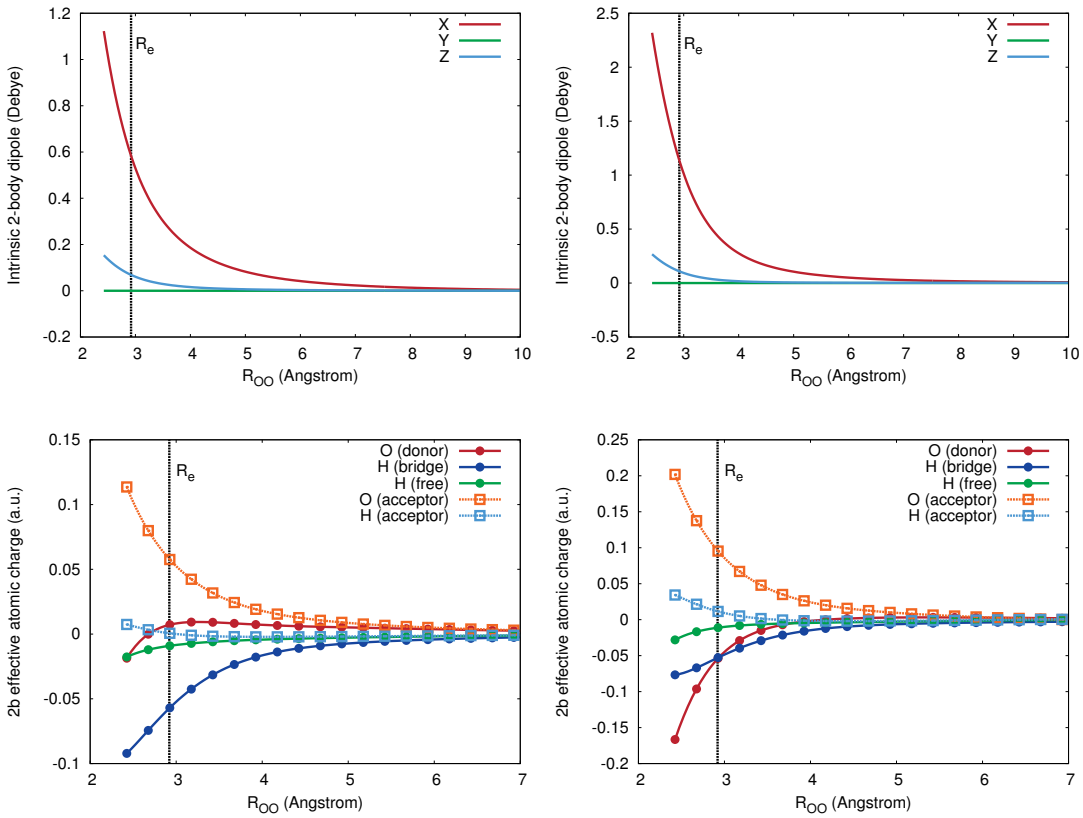

Figure 2.3. Intrinsic 2-body dipole cut and the effective atomic charge from the fitting for the 2-body dipole, along OO distance for water dimer. The directions of the three dipole components are indicated in Figure 2.1. Results of an undistorted monomer (the global minimum at equilibrium OO distance) are shown on the left. Results of a distorted example (the two local normal modes of the H-bond donor monomer, the H-bonded OH and free OH, are stretched by 0.4 a.u. away from the minimum) are shown on the right.

A more detailed analysis of the intrinsic 2-body dipole is shown in Figure 2.3

where the three dipole components (top panels) and the effective atomic charges (bottom panels) are plotted versus R_{OO}. In considering these effective charges it must be kept in mind that these are obtained from mathematical fitting of the intrinsic 2-body dipole moment. Note the charge on each atom is shown, except for one H on the acceptor monomer because it has the same charge of the other H on the acceptor due to the symmetry. We show the results for both the undistorted dimer (left panels) and an example of a distorted dimer (right panels), which the donor is stretched along its local normal (lormal) modes by 0.4 a.u. for both the H-bonded OH and free OH stretches. For the undistorted dimer, the dominant dipole component (upper left panel) is the one approximately along the H-bond, from the H-bonded (bridge) hydrogen pointing to the oxygen on the H-bond acceptor. For the effective charges of the undistorted dimer (bottom left panel), when the two monomers are close, we see some significant positive charge on the acceptor O atom and a correspondent negative charge on the bridge (H-bonded) H atom. This charge separation rapidly diminishes as the OO distance increases; when the monomers are dissociated, all effective atomic charges are zero, mathematically meaning the intrinsic 2-body dipole is zero. In literature, the dependence of transition dipole moments on the OO distance (or in general the translational and rotational coordinates of other monomers) has been occasionally referred to the so-called "Non-Condon effect".[22] For the distorted dimer, the 2-body dipole

components (top right panel) are larger than the values of the undistorted dimer. Also the effective 2-b charges (bottom right panel) are significantly different from the undistorted case. This observation fundamentally contrasts to the fixed point-charge models.

Table 2.2. Dipole moment magnitude (Debye) of the water dimer, trimer and prism hexamer. Shown in the table are the values directly from MP2/aVTZ, the values from 1-body and 2-body representation of MP2/aVTZ dipole, and the values from the present DMS. The geometries are the ones optimized from the PES.

	MP2/aVTZ				DMS(1b-LTP, 2b-MP2)
	μ	μ_{1b}	μ_{2b}	μ_{1b+2b}	μ
dimer	2.573	1.993	0.584	2.573	2.572
trimer	1.035	1.043	0.032	1.037	1.036
w6-prism	2.599	2.286	0.381	2.658	2.662

Next, we examine the accuracy of the 1,2-body representation of the dipole. This is done first by examining the dipole moment from direct MP2/aVTZ calculations and the 1,2-body representation using MP2/aVTZ calculations of several small water clusters, shown in Table 2.2. For the dimer, obviously the 1- and 2-body representation yields the exact dipole. The 1-body dipole is about 77%

while the intrinsic 2-body is about 23% of the total magnitude. For the trimer (up-up-down configuration), because the symmetry of the three H-bonds in the ring-like configuration, the vector sum of the three 2-body dipole moments nearly cancel. For the prism hexamer, the 2-body dipole contributes roughly 14% of the total dipole. For the trimer and hexamer, the 1- and 2-body representation only has roughly 2% error compared with the direct MP2/aVTZ calculation. Also shown in Table 2.2 are the dipole magnitudes from the new DMS. The 1- and 2-body MP2/aVTZ dipoles agree well with the new DMS dipoles for the three clusters, although we expect the DMS results may be the more accurate one.

Table 2.3. Double-harmonic IR frequencies and intensities for the water dimer from the present DMS(1b-LTP,2b-MP2), from direct MP2/aVTZ and CCSD(T)-F12b/aVDZ calculations. The normal mode analysis was done using the PES.

mode	cm^{-1}	intensity (km/mol)		
		DMS(1b-LTP,2b-MP2)	MP2/aVTZ	CCSD(T)-F12b/aVDZ
1	127	121	121	120
2	140	47	47	48
3	150	147	146	145
4	181	134	135	134
5	351	52	53	52

6	610	95	95	95
bend 1	1650	87	87	86
bend 2	1669	39	39	40
HB OH	3758	244	265	247
symm	3828	9	11	9
asymm	3917	106	127	108
free-OH	3935	77	98	82

More relevant to IR calculations is the dipole derivative. This is examined in a direct way by calculating the double-harmonic IR spectra of the water dimer (results in Table 2.3) and the hexamer prism (results in Table 2.4). Since the 1,2-body representation is exact for the dimer, the comparison is free of that approximation and in addition for that cluster efficient CCSD(T)-F12b/aVDZ calculations are feasible and so those are presented as the benchmark ones in Table 2.3. For this comparison we use the optimized geometry and normal modes from the WHBB PES. First, note the excellent agreement of the DMS intensities with the CCSD(T)-F12b/aVDZ results, especially for the intramolecular modes. By contrast the MP2/aVTZ intensities for these modes show some disagreements with the CCSD(T)-F12b/aVDZ one. The pattern of disagreement of the MP2 intensities is very similar to the monomer intensities shown in Table 2.1. So, the expectation of

greater accuracy of the present DMS compared to MP2/aVTZ is borne out in this comparison. Next, note the increased intensities of the OH-stretch modes compared with the monomer, especially for the H-bonded OH stretch. As shown in detail below, this large increase in the H-bonded OH stretch intensity is due to the 2-body dipole. For the six intermolecular modes, there is excellent agreement among all the calculations. The agreement between the DMS and MP2/aVTZ intensities is perhaps expected for these modes since the 2-body dipole is more significant for these modes than the 1-body dipole and the former is after all just a fit to the MP2/aVTZ 2-body dipole. That there is also excellent agreement with the CCSD(T) intensities is not obvious. However, as shown in Figure 2.2, MP2 and CCSD(T) give very close values for the intrinsic 2-body dipole; therefore it is not a surprise to see such excellent agreement for the intermolecular bands in Table 2.3, given the argument above that these modes are dominated by the 2-body dipole.

Table 2.4. Double-harmonic IR frequencies and intensities for the prism isomer of water hexamer from the new DMS and from direct full MP2/aVTZ, and 1-body and 2-body MP2/aVTZ calculations, denoted MP2/aVTZ (1,2). The normal mode analysis was done using MP2/aVTZ at the MP2/aVTZ minimum.

		intensity (km/mol)		
mode	cm^{-1}	DMS	MP2/aVTZ	MP2/aVTZ (1,2)

1	62	1.9	1.7	1.9
2	73	0.1	0.1	0.1
3	78	1.4	1.3	1.4
4	90	0.8	0.7	0.8
5	104	0.8	0.8	0.8
6	145	0.7	0.7	0.7
7	171	12	11	12
8	176	2.6	2.3	2.6
9	212	0.8	0.8	0.9
10	220	37	36	37
11	238	44	41	44
12	248	26	24	26
13	279	51	50	50
14	288	45	44	44
15	293	31	28	31
16	362	55	55	55
17	375	5.6	6.8	5.4
18	431	56	54	55
19	437	43	42	43
20	472	44	43	44

21	501	50	48	50
22	543	222	210	221
23	560	22	21	22
24	622	352	328	353
25	648	134	126	134
26	688	205	183	204
27	731	259	236	258
28	842	42	36	42
29	892	53	51	53
30	1035	61	63	62
31	1642	184	169	185
32	1655	56	50	55
33	1664	85	76	86
34	1679	14	14	14
35	1694	113	110	110
36	1714	41	43	41
37	3195	779	889	851
38	3443	684	746	745
39	3547	161	189	185
40	3572	536	557	574

41	3687	159	161	171
42	3701	220	234	242
43	3765	56	62	65
44	3782	413	462	478
45	3808	222	240	255
46	3891	57	80	74
47	3894	64	87	82
48	3896	78	100	96

The enhancement of the double-harmonic H-bonded OH intensity is even more pronounced for the prism hexamer as shown in Table 2.4. The intensities of two H-bonded OH stretches (mode 37 and 38) are about 700 km/mol, which is roughly three times larger than for the H-bonded OH stretch of the dimer. This is a result of the more elaborate 3D H-bonding network in the prism and therefore a larger contribution of the intrinsic 2-body interactions. These double-harmonic intensities also provide a test of the accuracy of the 1,2-body representation of the dipole moment for IR intensities. This test is between the 1- and 2-body MP2/aVTZ (denoted as MP2/aVTZ(1,2)) intensities versus the full MP2/aVTZ intensities. As seen, the agreement is generally within a few percent, with the worst agreement being around 10%. This indicates the 1- and 2-body

representation of dipole is also accurate for dipole derivatives. Also seen in Table 2.4, the DMS OH stretch intensities are in general lower than the corresponding MP2/aVTZ(1,2) results, while the bend intensities are quite similar. This is again due to the LTP monomer DMS, as already discussed in the monomer and the dimer cases. The H-bonded OH modes drop roughly 10% intensity, less than the roughly 20% drop seen in the free-OH modes, reflecting that the intensities of H-bonded OH stretch modes are dominated by the 2-body dipole.

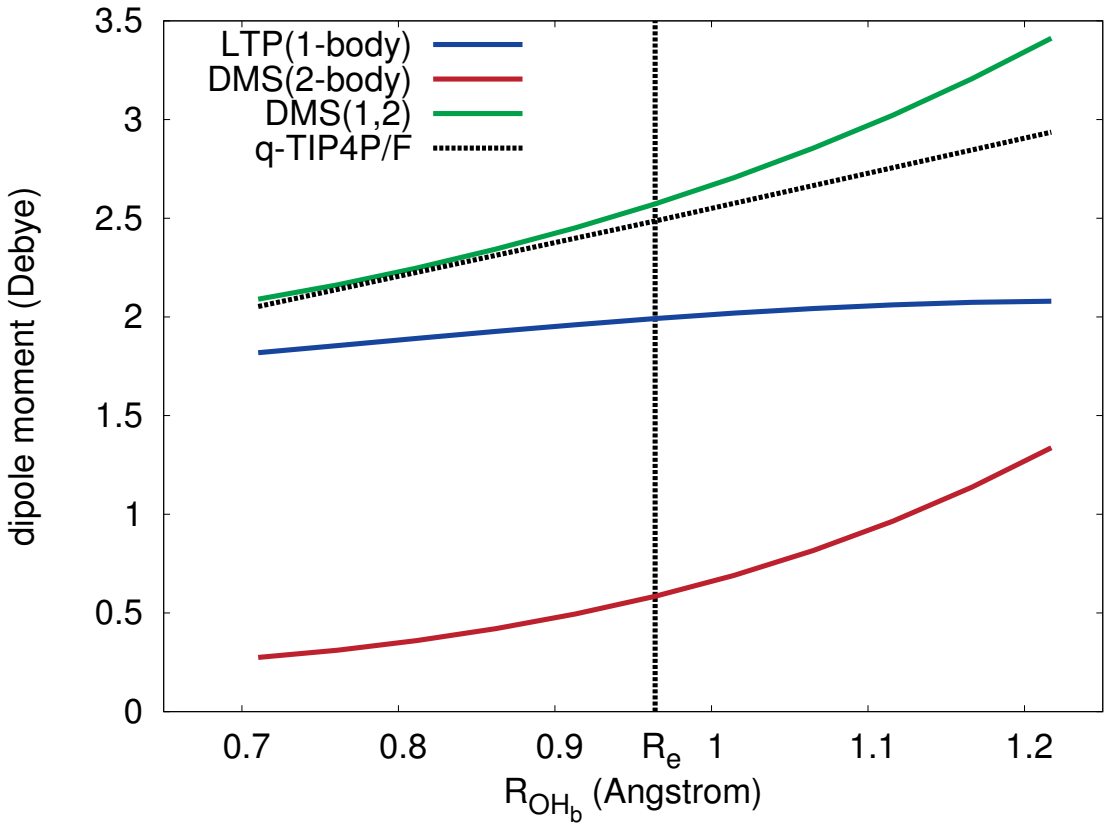

Figure 2.4. Dipole magnitude of water dimer as a function of the H-bonded OH-stretch of the dimer at the minimum as it varies along the local normal coordinate shown in Figure 2.1.

To probe deeper into these double-harmonic intensities, we plot the 1-body, 2-body, and the total dipole moment magnitude from the present DMS versus the lormal mode displacement of the H-bonded OH stretch of the dimer in Figure 2.4. The vector of this mode is illustrated in Figure 2.1. As seen, it is mainly the H bonded OH-stretch and so that distance (as it varies along that lormal mode) is plotted as the abscissa. At the equilibrium OH distance of 0.964 A, the 1-body dipole (LTP) is the major component of the total dipole. However, as the OH distance increases (increase in the local normal mode displacement), the intrinsic 2-body dipole grows much faster than the nearly linear increase of the 1-body dipole. Thus, the slope of the total dipole at equilibrium is mainly determined by the larger slope of the 2-body dipole. This explains the large increase of the OH intensity of the dimer over the monomer because the IR intensity is proportional the square of the dipole derivative. The dipole from the q-TIP4P/F model[23] is also plotted in Figure 2.4. This dipole is simply a sum of the two monomer fixed-charge dipoles. In the q-TIP4P/F model (actually TIP4P), the effective charges on the hydrogen and the oxygen atoms were empirically determined and we see in Figure 2.4 that its dipole agrees well with the new DMS dipole at equilibrium or shorter OH distance. However, the linear dipole from q-TIP4P/F fails to predict the dipole derivative that the present *ab initio* DMS predicts. Specifically the q-TIP4P/F

dipole derivative at the equilibrium is smaller than the present DMS. Given this underestimated dipole derivative for the H-bonded OH stretch mode, it is understandable why q-TIP4P/F underestimates the intensity for the OH stretch band in the IR spectrum.[23-24]

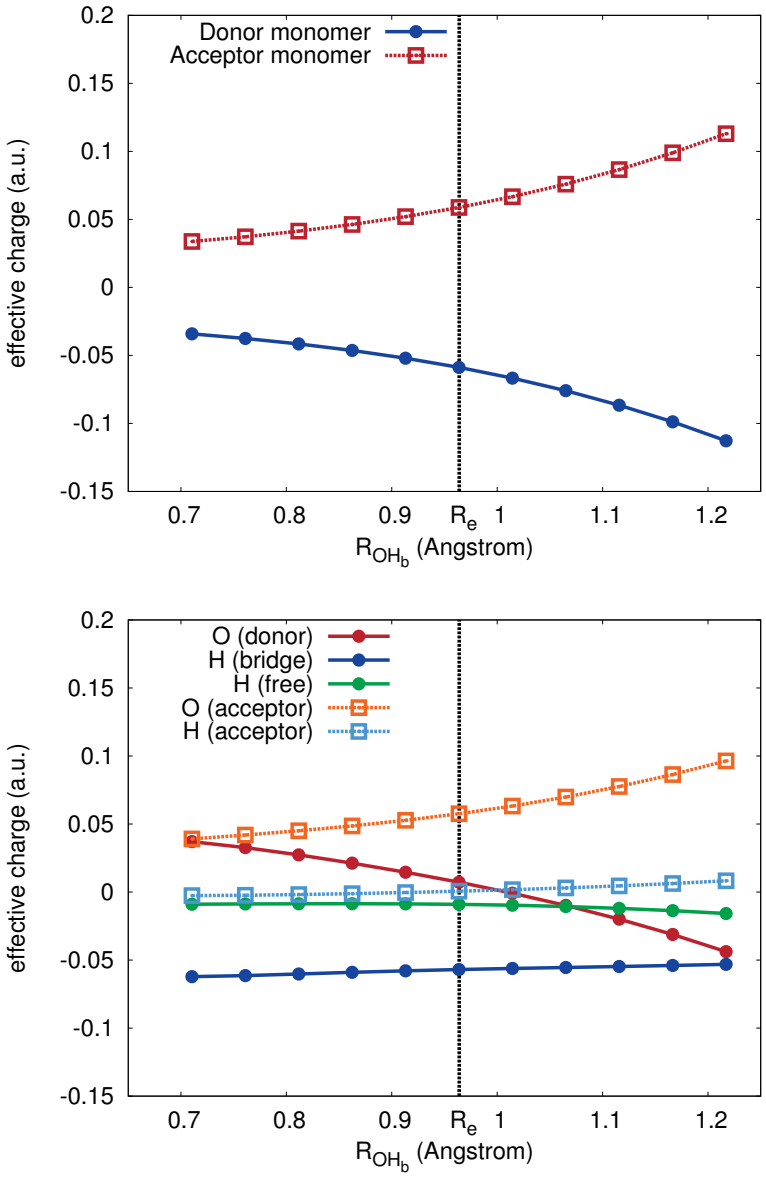

Figure 2.5. Effective 2-body charges from the present DMS as a function of the H-bonded OH-stretch of the dimer at the minimum as it varies along the local

normal coordinate shown in Figure 2.1. Top: the monomer total charges. Bottom: atomic charges. The atomic charge is same for the two H atoms on the acceptor monomer due to symmetry.

To give additional insight into the intrinsic 2-body dipole, we show the effective charges versus the same H-bond OH stretch in Figure 2.5. In this figure "Donor" refers to the hydrogen donor as usual, which is the monomer on the left in Figure 2.1, and "Acceptor" is the monomer on the right. Again, it is worth reminding that these effective charges are obtained from the mathematical fitting of the intrinsic 2-body dipole moment. In the top panel of Figure 2.5, the net charges on both monomers are shown as a function of R_{OH_b}. Note the sum of these adds to zero as it should. At the global minimum where the R_{OH_b} is 0.964 Angstrom, the net charges are not equal with positive charge on the acceptor and negative charge on the donor. This finding is in qualitative agreement with the conclusion of negative charge transfers from the H-bond acceptor to the donor from various energy decomposition analysis calculations. For a recent compilation results and discussion of these see ref. 25. (Note, in this paper, the H-bond donor is referred to "electron acceptor".) Also, as seen R_{OH_b} increases beyond the equilibrium value, the magnitude of charge separation from the donor and the acceptor monomers increases. This suggests that charge transfer increases as R_{OH_b} increases.

To provide more details, the effective charges of each atom of the intrinsic 2-body dipole, are shown in the bottom panel of Figure 2.5. Note at the global minimum, the positive net charge on the acceptor monomer mainly sits on the O atom, while the negative net charge on the donor monomer mainly sits on the bridging donor H atom. However, as as the OH distance increases, it is primarily the donor O atom that receives the negative charge transferred from the acceptor O atom, whereas the bridge H atom shows a steady negative charge on it.

To summarize this subsection, new tests confirm that the total dipole of water clusters can be accurately given by the 1-body and intrinsic 2-body representation. Including the 2-body dipole is essential to get the correct dipole derivative, or IR spectrum. Tests against the benchmark CCSD(T)/aVTZ results show the MP2 based 2-body DMS is accurate. The DMS describe the interaction of a monomer with others directly from *ab initio* 2-body dipole calculations, which is conceptually different from the empirical approaches that TTM3-F use. The fixed point-charge models such as q-TIP4P/F may be inappropriate for IR calculation because the important 2-body effect is missed.

References

1. Y. Wang, X. Huang, B. C. Shepler, B. J. Braams and J. M. Bowman, J. Chem. Phys. **134**, 094509 (2011).
2. J. Cui, H. Liu and K. D. Jordan, J. Phys. Chem. B **110**, 18872 (2006).
3. K. Szalewicz, C. Leforestier and A. van der Avoird, Chem. Phys. Lett. **482**, 1 (2009).
4. U. Góra, R. Podeszwa, W. Cencek and K. Szalewicz, J. Chem. Phys. **135** (2011).
5. H. Partridge and D. W. Schwenke, J. Chem. Phys. **106**, 4618 (1997).
6. X. Huang, B. J. Braams and J. M. Bowman, J. Phys. Chem. A **110**, 445 (2005).
7. B. J. Braams and J. M. Bowman, Int. Rev. Phys. Chem. **28**, 577 (2009).
8. G. S. Fanourgakis and S. S. Xantheas, J. Chem. Phys. **128**, 074506 (2008).
9. Y. Wang, V. Babin, J. M. Bowman and F. Paesani, J. Am. Chem. Soc. **134**, 11116 (2012).
10. Y. Wang and J. M. Bowman, J. Phys. Chem. Lett. **4**, 1104 (2013).
11. Y. Wang and J. M. Bowman, J. Chem. Phys. **135**, 131101 (2011).
12. L. C. Ch'ng, A. K. Samanta, Y. Wang, J. M. Bowman and H. Reisler, J. Phys. Chem.A **117**, 7207 (2013).
13. Y. Wang and J. M. Bowman, J. Chem. Phys. **134**, 154510 (2011).
14. H. Liu, Y. Wang and J. M. Bowman, J. Phys. Chem.. B **118**, 14124 (2014).
15. H. Liu, Y. Wang and J. M. Bowman, J. Phys. Chem.Lett. **3**, 3671 (2012).

16. H. Liu, Y. Wang and J. M. Bowman, J. Chem. Phys. submitted

17. H. Liu, Y. Wang and J. M. Bowman, J. Phys. Chem. B **117**, 10046 (2013).

18. H. Liu, Y. Wang and J. M. Bowman, J. Am. Chem. Soc. **136**, 5888 (2014).

19. J.S. Mancini, J.M. Bowman, J. Phys. Chem. Lett. **5**, 2247 (2014).

20. H. R. Leverentz, K. A. Maerzke, S. J. Keasler, J. I. Siepmann and D. G. Truhlar, Phys. Chem. Chem. Phys. **14**, 7669 (2012).

21. L. Lodi, J. Tennyson and O. L. Polyansky, J. Chem. Phys. **135**, 034113 (2011).

22. J. R. Schmidt, S. A. Corcelli and J. L. Skinner, J. Chem. Phys. **123**, 044513 (2005).

23. S. Habershon, T. E. Markland and D. E. Manolopoulos, J. Chem. Phys. **131**, 024501 (2009).

24. M. Rossi, M. Ceriotti and D. E. Manolopoulos, J. Chem. Phys. **140**, 234116 (2014).

25. E. Ronca, L. Belpassi and F. Tarantelli, Chemphyschem **15**, 2682 (2014).

Chapter 3.

The Quantum Local-Monomer Model

3.1. Overview

The huge dimensionality makes it very difficult to study the nuclear dynamics of condensed phase matter like liquid water or ice. Many methods have been applied to study the nuclear dynamics of water, including the classical, semiclassical, approximate quantum, and a mixture of them.

Classical MD simulation can be used to calculate the IR spectra for water by performing the Fourier transformation to the dipole auto-correlation function. For example, this approach has been used to parametrize the TTM3-F potential.[1] A well-known issue with classical calculations is that it causes systematical blue-shift of peak frequencies (on the order of 200 cm^{-1}) because without the zero-point energy the anharmonic region of the potential is not easily accessed. Clearly, in order to obtain accurate vibrational spectra, one has to go beyond the classical methods. Semiclassical initial value representation (IVR) approach has been used for the liquid water IR spectra with the SPC/Fw and TTM3-F potentials by the Miller group.[2,3] Other efforts include the path integral molecular dynamics (PIMD) inspired

methods, such as centroid molecular dynamics (CMD) and (thermostatted) ring-polymer molecular dynamics (TRPMD).[4-6] These methods have been applied along with the fixed point-charge water models as well as the TTM3-F model, for the liquid water IR spectra.

There are also several approximate quantum methods for vibrational spectra, performed in a reduced space of dimensionality. The most straightforward model is called the local-mode model, which treats the OH bond as a 1-dimensional chromophore. This method has been applied to calculate the OH(OD) stretch IR spectra, using thousands monomer configurations from classical MD trajectories.[7-10] The limitation of this model is that it is not able to describe spectral bands other than the OH stretch.

Beyond the 1-dimensional local-mode model is the Local-Monomer Model(LMon).[11] The LMon model couples at least three modes, the bend and two stretches, with options to couple more modes that describing the intermolecular vibrations. The LMon monomer Schrodinger equations are solved using the VSCF/VCI approaches using the software MULTIMODE. LMon method has been successfully applied, along with the WHBB ab initio PES and DMS, for IR spectra from water dimer to an ice model of roughly 200-mer. Some non-linear features, such as the bend overtone, have been shown to be important characteristics of the spectra of water hexamer and ice Ih.[11-15]

3.2. Theory

In the Local-Monomer model (LMon), the Schroedinger equation of a water monomer

$$[\hat{T}_m + U_m(Q_m) - E_i^{(m)}]\phi_i^{(m)}(Q_m) = 0$$

is solved, where $\hat{T}_m$ is the Watson kinetic operator, U_m is the potential energy of monomer *m* in terms of the local normal (lormal) modes of monomer *m*, Q_m. These modes are obtained from a lormal mode analysis of monomer *m*. U_m is the potential of the water cluster, only varying along lormal modes of monomer *m*, Q_m, with all other monomers fixed at their (perturbed) structures. If using a many-body PES, such as the WHBB PES, the potential U_m is given by the following expression:

$$U_m = V_{1-body}(m) + \sum_{i=1,i\neq m}^{N} V_{2-body}(m,i) + \sum_{i<j,i\neq m,j\neq m}^{N} V_{3-body}(m,i,j)$$

Note that while U_m depends explicitly on the lormal modes of monomer *m,* the potential, as seen above, depends on interactions of momoner *m* with other monomers in the cluster.

The local normal modes are obtained from diagonalization of the 9 x 9 mass-scaled Hessian matrix of monomer *m.* To see how this arises formally, we write the full Hessian matrix for *N* momomers as

$$\mathbf{H} = \begin{bmatrix} \mathbf{H}_{11} & \mathbf{H}_{12} & \cdots & \mathbf{H}_{1N} \\ \mathbf{H}_{21} & \mathbf{H}_{22} & \cdots & \mathbf{H}_{2N} \\ \vdots & \vdots & \ddots & \vdots \\ \mathbf{H}_{1N} & \mathbf{H}_{2N} & \cdots & \mathbf{H}_{\mathrm{NN}} \end{bmatrix}$$

where the mass-scaled coordinates are arranged in terms of the monomers so that each diagonal block is just the mass-scaled Hessian for each monomer. Thus H can be written as $H = H_M + H'$ where H_M is the block-diagonal matrix of monomer Hessians and H' is the remainder. Then, if H_M diagonalized by the matrix L_M, we have

$$L_M^t H L_M = \Lambda_M + L_M^t H' L_M,$$

where Λ_M is the matrix of eigenvalues of H_M and $L_M^t H' L_M$ is the coupling matrix, which if neglected gives the local monomer approximation to the full normal modes analysis. (Note the coupling matrix or approximations to it can and have been used to incorporate monomer-monomer coupling.[16]) For a cluster of N water monomers, there are $9N$ local modes and harmonic frequencies, which are obtained from the diagonalization of N 9 x 9 Hessians, compared to diagonalizing a $9N$ x $9N$ Hessian in the usual standard normal-mode analysis.

There are totally 9 modes for each monomer; 3 are intramolecular modes and 6 are intermolecular modes. Ideally, the LMon Schroedinger equation is solved using all 9 lormal modes. However, because the cost grows steeply with the size of the quantum space, a fully coupled LMon-9 calculation is costly and the total cost for say

1000 monomer calculations becomes borderline prohibitive. The minimum approach, denoted as LMon-3, is to couple the three intramolecular modes, the bend and two OH stretches. LMon-3 is a powerful tool for intramolecular bands of vibrational spectra, e.g. the OH stretch and bend. In other applications such as vibrational energy relaxation or the low-frequency region of the IR spectra, the intermolecular modes are important so we also developed strategies to include them in the LMon model. Two types of extensions will be described in detail in the next two sections.

The LMon-4 Schroedinger Eq. 4 is solved using vibrational self consistent field (VSCF) followed by virtual state configuration interaction (VCI) methods with the code MULTIMODE.[17-19] The potential energy is treated as a many-mode expansion in monomer's lormal modes[17]. For LMon-3 applications, using the 3-mode representation (3MR) is exact. For LMon applications with large quantum space (described in next two sections), usually using up to 3MR gives converged results. The VSCF basis functions are expanded in a primitive basis of harmonic oscillator functions. The natural choice of method to evaluate the matrix elements over the potential is the Gaussian-Hermite quadrature. Optimized "HEG" quadrature can be used to further improve the efficiency.

To calculate the IR spectra, the dipole transition strength from the ground vibrational state is obtained by the usual expression

$$R_{0\to f_m} = \sum_{\alpha}^{x,y,z} \left| \langle f_m | \mu_{\alpha,m} | 0_m \rangle \right|^2 \quad ,$$

where 0_m is the monomer ground-state wavefunction. f_m is the monomer final-state wavefunction, and $\mu_{\alpha,m}$ is Cartesian component of the dipole moment of monomer *m*, which depends on the lormal modes. Like the potential, we only evaluate the dipole terms $\bar{\mu}(m)$ that have coordinate dependency of monomer *m*, but not the full dipole

$$\boldsymbol{\mu}_m = \boldsymbol{\mu}_{1-body}(m) + \sum_{k\neq m} \boldsymbol{\mu}_{2-body}(m,k) \quad .$$

3.3. Extension 1: LMon-4

As mentioned above, some applications require some or all of the 6 intermolecular lormal modes to be included. Directly performing a 9 modes coupled LMon-9 calculation would be very computationally expensive. Therefore, we developed an approximate approach LMon-4, which allows us to consider all the 6 intermolecular modes, but only one mode at a time. In each LMon-4 calculation, 1 out of 6 intermolecular modes is coupled to the 3 intramolecular modes. 6 sets of LMon-4 calculations are performed for each monomer configuration, in order to cover all the 6 intermolecular modes. All the vibrational stats from the 6 sets of LMon-4 calculations are collected.

To obtain the spectrum from these LMon-4 calculations requires some care, as simply adding the spectra from the 6 sets of LMon-4 calculation would be incorrect.

This is because each LMon-4 calculation contains the intramolecular modes but only 1 of each of the six intermolecular modes. Thus, simply adding the LMon-4 spectra would over-count the contributions of intramolecular modes. The calculations find that the frequency and intensity of these intramolecular bands (the stretch and bend fundamentals and bend overtone are the bands of interest) from the 6 LMon-4 calculations are all similar and in fact similar to LMon-3 calculations (using the subspace of only bend and two stretches). There are of course some important differences from due to the "perturbation" of the different intermolecular modes. A straightforward procedure is done account for this. It is to apply a weighting factor to the IR intensity of each of the final states obtained from all the 6 sets of LMon-4 calculations

$$W_{f_m} = \begin{cases} 1/6 & \text{intramolecular state} \\ 1 & \text{intermolecular state} \end{cases}$$

The procedure to identify intramolecular states is almost by inspection, based on the energy and intensity, since we are restricted to considering the portion of the IR spectrum that contains the high-frequency stretch and bend fundamentals and bend overtone. However, a state was assigned to be "intramolecular" based on an examination of the VCI coefficients of eigenfunctions. For the monomer bend and stretches the eigenfunctions contain little (but not zero of course) mixing with intermolecular states. All other states that have non-zero quanta in the intermolecular mode in the largest VCI coefficient, are defined as intermolecular

states. Finally a Gaussian lineshape function is applied to each intensity-weighted stick, usually with a FWHM of 70 cm^{-1} and the final spectrum is then just the weighted sum of LMon-4 spectra for each monomer for a given configuration of monomers.

In order to compute the IR spectrum of liquid water, evolving monomer configurations must be taken into consideration. With these, the LMon-4 IR spectrum is obtained from this expression

$$I(\nu) \propto \sum_{t=0}^{T} \sum_{m=1}^{N} \sum_{f_m < 4000\,cm^{-1}} \nu_{0\to f_m}(t) R_{0\to f_m}(t) W_{f_m} g(\nu - \nu_{0\to f_m})$$

where the additional sum is over an ensemble of molecular configurations corresponding to a thermal distribution of liquid water. For example, one can sample monomer configurations is to use snapshots from classical MD trajectories. As noted already, f_m is a final state vibrational wavefunction, $\nu_{0\to f_m}$ is the transition frequency and $R_{0\to f_m}$ is the transition dipole moment. These are all obtained from LMon-4 calculations. W_{f_m} is the weighting factor and $g(\nu - \nu_{0\to f_m})$ is the Gaussian lineshape function.

The above equation and related expressions are given for transitions from the ground vibrational state. However, the LMon-4 calculations also describe transitions from excited initial states and the expressions for the IR spectra from those are the obvious and usual generalization of the ones given above.

3.4. Extension 2: LMon-6 and Wave Packet Dynamics

The standard LMon-3 and LMon-4 approaches can be further extended to study the quantum dynamics of vibrational energy relaxation (VER). For the VER of ice and water, we reasonably assume, as others have,[20 and references therein] the relaxation is via the intramolecular modes and eventually to the intermolecular modes. Therefore we expand the quantum space of LMon model to 6 modes, consisting 3 intra- and 3 inter-molecular modes. The LMon-6 Schrodinger equation is solved using the same VSCF/VCI methods in the code MULTIMODE. The wavepacket calculations are straightforward in the basis of eigenstates of the Hamiltonian, once a choice for the wavepacket at t = 0 is made. For this a virtual state is selected that represents the OD or OH stretch with fundamental or overtone excitation at 0 K. This non-stationary state is then propagated in the basis of eigenstates. The details are given is described as follow.

To start with, we write down the VCI molecular eigenstate ψ_j as follows:

$$\psi_j = \sum_{i=1}^{N} c_{ji}\phi_i ,$$

where the basis functions ϕ_i are virtual states, *N* is the number of basis functions and c_{ji} are the coefficient of the eigenvector matrix.

A non-stationary virtual state is used to represent the initial wave packet of OD/OH excitation. It is expanded in the space of N eigenstates

$$\Psi_k(0) = \phi_k = \sum_{i=1}^{N} c_{ki}^{-1} \psi_i$$

Because the eigenvector matrix is orthogonal $C^{-1} = C^T$,

$$\phi_k = \sum_{i=1}^{N} c_{ki}^{T} \psi_i = \sum_{i=1}^{N} c_{ik} \psi_i$$

The time-dependent wave packet is given by

$$\Psi_k(t) = \sum_{i=1}^{N} c_{ik} \psi_i e^{-iE_i t/\hbar}$$

and the auto-correlation function is given by

$$C_k(t) = \langle \Psi_k(0) | \Psi_k(t) \rangle = \sum_{i=1}^{N} c_{ik}^2 e^{-iE_i t/\hbar} .$$

$C_k(t)^2$ is the population decay of the initial wave packet $\Psi_k(0)$. In addition, projecting $\Psi_k(t)$ onto another VSCF virtual state ϕ_m give the cross-correlation

$$C_k^m(t) = \langle \phi_m(0) | \Psi_k(t) \rangle = \sum_{i=1}^{N} c_{im} c_{ik} e^{-iE_i t/\hbar} .$$

$C_k^m(t)^2$ represents the time-dependent population in state ϕ_m. It is easily shown that the sum of populations in all VSCF virtual states is equal to one.

3.5. Tests and Comparisons

3.5.1. Local Harmonic Analysis

To assess the accuracy of the local harmonic analysis, we show in Figure 3.1 a comparison of the harmonic vibrational density of states from a local-monomer and full harmonic vibrational analysis of a 192-mer model of Ice Ih[21] using the WHBB potential. As seen, there is excellent agreement above 1500 cm^{-1}; this was

anticipated since this region is the intramolecular bend on OH-stretch region. These modes are the three high-frequency modes of each monomer. Agreement is good between 500 and 1000 cm^{-1}; an examination of the normal modes[21] reveals that these modes are librational modes and these are captured by the frustrated rotational local normal modes. Below roughly 400 cm^{-1}, the accuracy of the local mode model deteriorates and misses the peak at roughly 60 cm^{-1}. The region of discrepancy is characterized by low-frequency acoustic (~60 cm^{-1}) and optical (200-300 cm^{-1}) lattice modes, which are collective monomer translational modes. (A detailed analysis of these modes is given in Chapter 4) Thus, these modes are not expected to be well described by the local-monomer modes. So, for the IR (and Raman) spectral bands corresponding to the intramolecular modes, the local monomer approach is well justified, and even for the next lower band of intermolecular modes it should provide good accuracy.

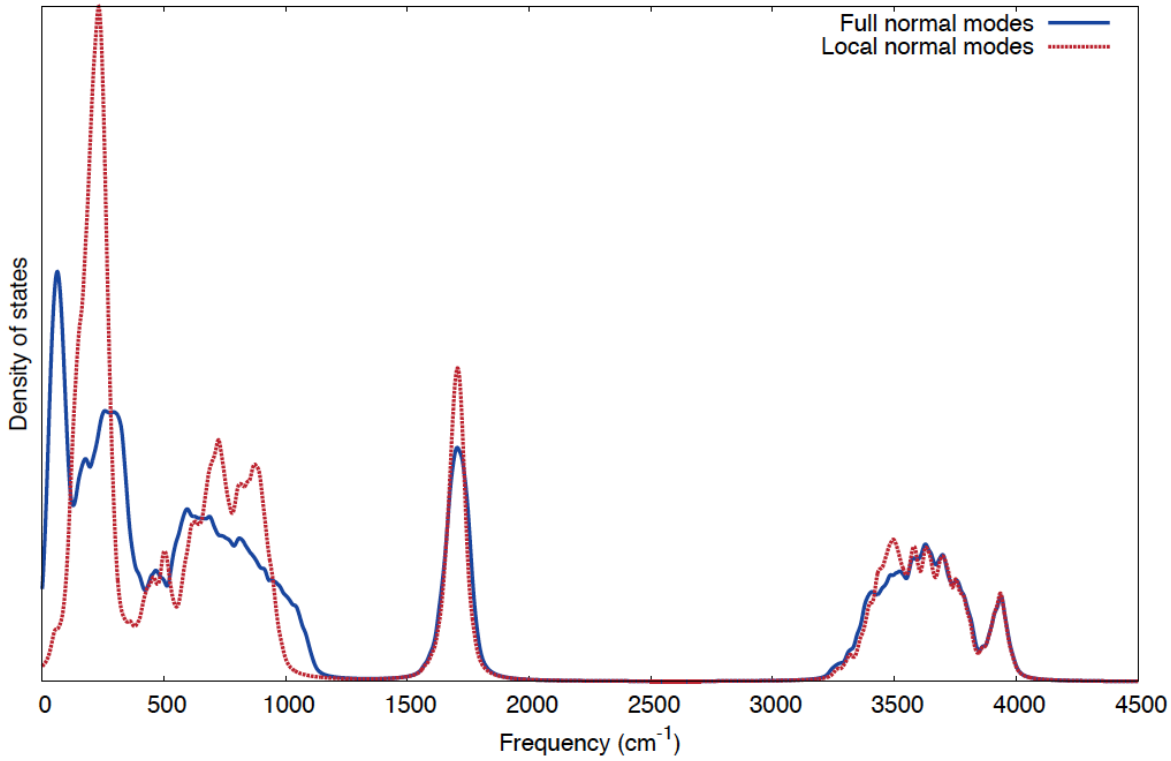

Figure 3.1. Comparison of full and local-normal mode harmonic density of states for H_2O 192-mer cluster with an Ice Ih configuration

3.5.2. Compare Local-Monomer Model with Other Methods for Vibrational Spectra in the Condensed Phase

Here, we perform such cross-validation, comparing the behavior of MQC, LMon, CMD, and TRPMD when modeling a physical observable that is particularly sensitive to the description of nuclear quantum dynamics—the infra-red absorption spectra of hydrogen-containing compounds.[4,22-25] We focused on prototypical hydrogen-bonded condensed phase systems—HOD in D_2O and neat water—describing them with the inexpensive q-TIP4P/F potential,[5] and using the

corresponding linear dipole moment surface (DMS) to evaluate the IR absorption. The rationale for this simplistic choice is that we are not so much interested in comparing with experimental data, but only to nail down differences between methods for condensed-phase quantum dynamics. The simplicity of the potential and the linear DMS make it possible to guarantee thorough statistical sampling and to focus on the problem of modeling the dynamics on a complex, anharmonic potential energy surface, rather than on the fact that CMD and (T)RPMD are much harder to justify when computing correlation functions of nonlinear operators.[26-28] It also allows us to test extensively the dependence of TRPMD, CMD, and LMon on the precise details of the calculations. To validate the two philosophies over a broad range of conditions, and draw conclusions that are not purely anecdotal, we considered three very different thermodynamic regimes: ice Ih at 150 K, liquid water at 300 K, and the hot liquid at 600 K at the experimental liquid/vapor coexistence density. To assess the importance of these approximate nuclear quantum dynamics, we also compare our results to classical MD simulations.

CMD and TRPMD simulations were performed using the i-PI code,[29] and LAMMPS as the force back-end.[30] Standard LMon-4 calculations were performed. Note in this application, only three intermolecular modes with highest frequencies are considered. Details of the CMD, TRPMD, MQC and LMon-4 calculations are described in Ref [12, joint].

Let us start by considering a single HOD molecule solvated in H_2O. This system (and its counterpart, HOD in H_2O) is commonly used as a probe for studying the local structure of liquid water theoretically and experimentally.[23,31] The OH stretch is dynamically uncoupled with the environment, making this system well-suited for both MQC and LMon calculations.[20]

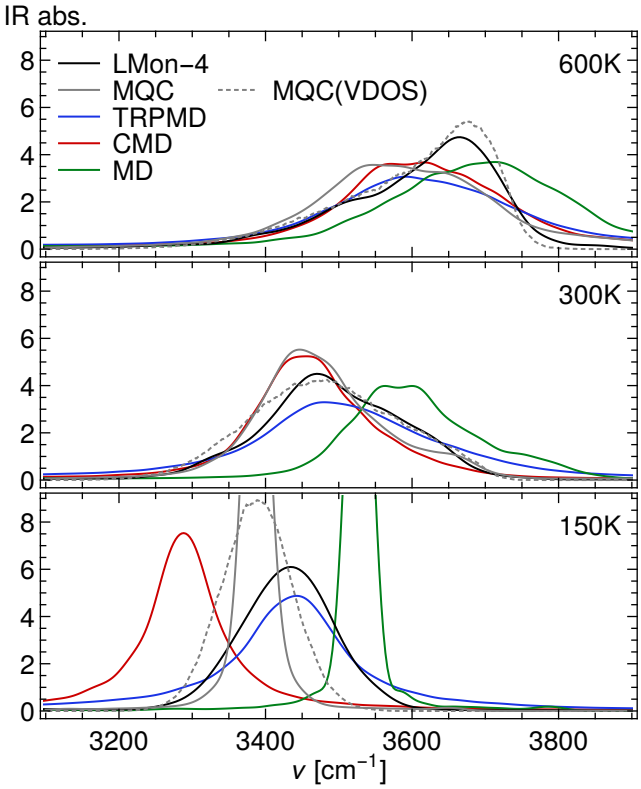

Figure 3.2. Comparison between the OH stretch IR absorption spectrum for a single HOD molecule in bulk D_2O, modeled using the q-TIP4P/F potential. Absorption spectra were computed from the dipole derivative autocorrelation, using classical molecular dynamics (green), CMD (red), and TRPMD (blue), and compared with the results of LMon-4 calculations (black), MQC line shape (gray), and VDOS (gray

dotted). The panels correspond, from top to bottom, to liquid water at 600 K, liquid water at 300 K, and ice Ih at 150 K. The integrated intensity of the OH stretch peak has been normalized to the same area.

The results for classical MD, CMD, TRPMD, MQC, and LMon are shown in Figure 3.2. Starting from the highest temperature, 600 K, with a hot and compressed liquid, we observe that classical MD is blue-shifted by around 50 cm^{-1} with respect to all quantum methods. Even at this high temperature nuclear quantum effects affect the calculation of dynamical properties. The blue shift of the classical simulation gets more pronounced by lowering the temperature, as expected, amounting to approximately 100 cm^{-1} at 150 K. At 600 K all quantum methods show a large blue-shift, increased band width and asymmetric or structured line shapes, compared to those at 150 and 300 K. The LMon-4 band intensity falls-off faster than other line shapes at the high-frequency edge of the band, and shows a sharper maximum which is 30–50 cm^{-1} to the "blue" of the CMD and TRPMD maxima, which are not sharp. Considering that the influence of low-frequency intermolecular modes, e.g., hot bands, additional dipole variation, vibrational relaxation, etc., becomes more important with increasing temperature and that LMon-4 is only partially describing this coupling, the limitations in the LMon-4 theory are also

expected to be become more apparent. The importance of inter-molecular couplings and of the dynamics of the environment at the higher temperature is also suggested by the large difference we observe between the MQC line shape, the Condon approximation to the MQC line shape, and MQC vibrational density of states.

At 300 K the agreement between different quantum techniques is perhaps even better. MQC and CMD overlap almost perfectly. The LMon peak is some 20–40 cm^{-1} higher in frequency, and the difference between the LMon and MQC line shapes is much less dramatic than at 600 K. At 300 K, in- homogeneous broadening effects (i.e., effects *not* related to vibrational relaxation or motional narrowing) are dominant. The TRPMD peak is further blue-shifted (by 20–40 cm^{-1}, depending on whether one considers the maximum or the mean position of the peak) and artificially broadened by the strong thermostatting of non-centroid modes.

In ice Ih at 150 K TRPMD and LMon still are in remarkable—although perhaps fortuitous—agreement. CMD shows a pronounced red shift of 180 cm^{-1}, which should probably be attributed to the curvature problem.[22,24] The MQC peak is red-shifted by about 60 cm^{-1} relative to LMon and TRPMD. One possible explanation for this shift is the description of the environment based on centroid configurations that are very close to classical. Contrary to higher temperatures, the LMon spectrum also depends on whether the environment configurations are obtained from the

beads of the PIMD simulation, or from the centroid. In the latter case, as when using configurations from classical MD, the OH stretch peak is red-shifted by 25 cm^{-1}. It is arguable which choice is more physically justified. On one hand, bead positions provide a statistically accurate snapshot of the quantum environment. On the other hand, centroids can be seen as a mean-field average of the quantum fluctuations of the neighboring molecules, closer perhaps to the spirit of a quantum-classical model. In the absence of a rigorous justification we can see this discrepancy as a sign of the break-down of the classical model for the environment, and consider the difference between the two spectra as an estimate of the reliability of LMon (and MQC) in this low temperature regime.

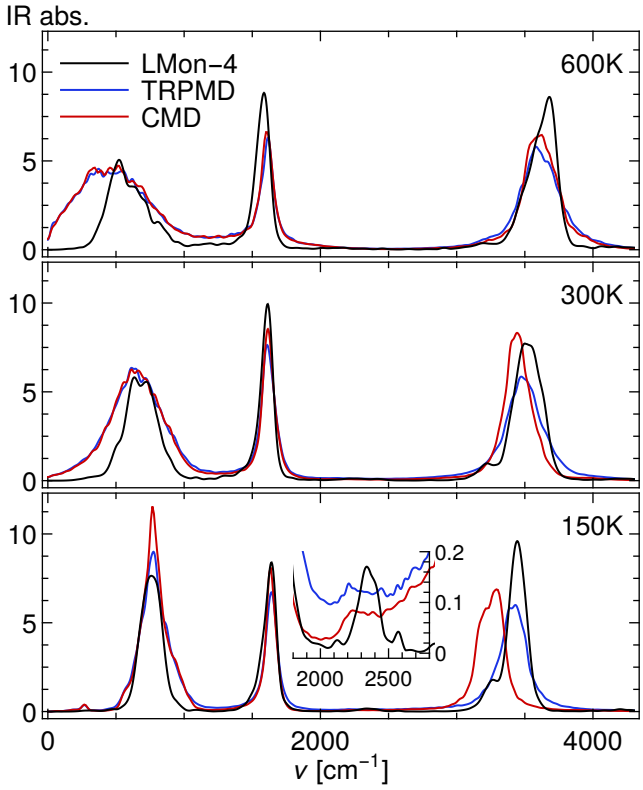

Figure. 3.3. Infra-red absorption spectrum of H_2O at three different thermodynamic conditions. From top to bottom: (compressed) liquid water at 600 K, liquid water at 300 K and ice Ih at 150 K. The curves correspond to TRPMD (blue), CMD (red), and LMon-4 calculations (black). Note in the middle panel the reduced red shift of the OH peak in CMD compared with the results in Ref. 22.

Having compared all methods for the HOD:D_2O bench- mark, we consider in Figure 3.3. the spectra of water in the three thermodynamic regimes discussed above. We did not perform MQC simulations, since the isolated chromophore assumption is less justified in H_2O. Let us start by discussing the OH band that shows similar trends to those observed for HOD in heavy water. At 600 K, CMD and TRPMD are in near-perfect agreement, and the peak maxima are slightly red-shifted relative to LMon-4 by about 50 cm^{-1}. This is consistent with our observations in HOD case, and the discrepancy can be attributed to the lack of homogeneous broadening and dynamical couplings in LMon. At 300 K TRPMD and LMon-4 are close to each other, while CMD shows a small red shift of less than 50 cm^{-1}, which is consistent with what we observed in HOD:D_2O. In the case of low- temperature ice the CMD peak is red shifted by 150 cm^{-1} compared to both LMon-4 and TRPMD that agree well with each other—even though the TRPMD peak is considerably broader. The

intensity of the stretching band is much under- estimated relative to experiments. This is due to the linear DMS of q-TIP4P/F, as evidenced by comparison with more sophisticated models,[32] but is irrelevant for our comparison of approximate methods for quantum dynamics.

Moving on to the bend, we observe good agreement in the peak position and width among all the quantum methods. All predict a slight red shift with increasing temperature (in qualitative agreement with experiment). TRPMD and CMD give peaks positions at 1640 cm^{-1} at 150 K and about 1610 cm^{-1} in at 600 K. LMon-4 gives 1640 cm^{-1} at 150 K and 1590 at 600 K. The peak at 600 K is further lowered to 1570 cm^{-1} when using LMon-3, indicating the growing importance of inter-molecular coupling at high temperature, and suggesting that this slight discrepancy between LMon-4 and PIMD- based methods could be resolved by increasing further the dimensionality of the quantum subspace. Finally, in the low- frequency region CMD and TRPMD are almost identical. In this region one cannot expect LMon-4 to yield quantitative accuracy. The quantum sub-space does not contain the collective modes of the hydrogen-bond network, nor the translation modes of individual monomers.

Within the LMon scheme it is straightforward to treat effects beyond linear absorption, and to give a clear physical attribution of specific features of the

spectrum. For in- stance, all of the spectra display a distinct bump or shoulder around 3200 cm^{-1}, which corresponds to the first overtone of the bend. An interesting feature captured by LMon-4 (but not by LMon-3) is the small peak around 2350 cm^{-1}, which is evident at 150 K and becomes less clear-cut with raising temperature. This feature is due to the combination band of bending and librational modes, and demonstrates how increasing the dimensionality of the quantum subspace progressively includes additional physical effects in LMon calculations. Both CMD and TRPMD display non-zero absorption in this region, but further analyses would be needed to attribute that spectral density to a precise physical origin.

The conclusions of our comparison of approximate quantum dynamics simulation methods are overall optimistic: all the methods we considered are generally consistent with each other, while the difference with the position of the OH stretching peak observed in classical molecular dynamics confirms the importance of including nuclear quantum effects to reproduce quantitatively spectroscopic measurements of hydrogen- containing systems. TRPMD and LMon agree within a few tens of cm^{-1} over a range of thermodynamic conditions going from ice Ih at 150K to water at 300K and finally to the hot, compressed liquid at 600 K. So do CMD down to room temperature, and MQC in the cases where we could apply it. Furthermore, this analysis reinforces the notion that performing

PIMD-based and quantum-subspace simulations in tandem does not only provide a degree of cross-validation, but also makes it possible to profit simultaneously from the complete (albeit approximate) description of the absorption spectrum given by the former family of methods, and from the interpretation of distinct spectral features that is enabled by an explicit quantum treatment.[33]

References

1. G. S. Fanourgakis and S. S. Xantheas, J. Chem. Phys. **128**, 074506 (2008).
2. J. Liu, W. H. Miller, F. Paesani, W. Zhang and D. A. Case, J. Chem. Phys. **131**, 164509 (2009).
3. J. Liu, W. H. Miller, G. S. Fanourgakis, S. S. Xantheas, S. Imoto and S. Saito, J. Chem. Phys. **135**, 244503 (2011).
4. S. Habershon, G. S. Fanourgakis and D. E. Manolopoulos, J. Chem. Phys. **129**, 074501 (2008).
5. S. Habershon, T. E. Markland and D. E. Manolopoulos, J. Chem. Phys. **131**, 024501 (2009).
6. M. Rossi, H. Liu, F. Paesani, J. Bowman and M. Ceriotti, J. Chem. Phys. **141**, 181101 (2014).
7. A. C. Belch and S. A. Rice, J. Chem. Phys. **78**, 4817 (1983).
8. V. Buch, J. Phys. Chem. B **109**, 17771 (2005).
9. H. Torii, J. Phys. Chem. A **110**, 9469 (2006).
10. B. Auer, R. Kumar, J. R. Schmidt and J. L. Skinner, Proc. Natl. Acad. Sci. U S A **104**, 14215 (2007).
11. Y. Wang and J. M. Bowman, J. Chem. Phys. **134**, 154510 (2011).
12. Y. Wang and J. M. Bowman, J. Chem. Phys. **135**, 131101 (2011).
13. H. Liu, Y. Wang and J. M. Bowman, J. Phys. Chem. Lett. **3**, 3671 (2012).

14. Y. Wang and J. M. Bowman, J. Phys. Chem. Lett. **4**, 1104 (2013).

15. H. Liu, Y. Wang and J. M. Bowman, J. Phys. Chem. B **118**, 14124 (2014).

16. Y. Wang and J. M. Bowman, J. Chem. Phys. **136**, 144113 (2012).

17. S. Carter, S. J. Culik and J. M. Bowman, J. Chem. Phys. **107**, 10458 (1997).

18. S. Carter, J. M. Bowman and N. C. Handy, Theor. Chem. Acc. **100**, 191 (1998).

19. J. M. Bowman, S. Carter and X. Huang, Int. Rev. Phys. Chem. **22**, 533 (2003).

20. H. Liu, Y. Wang and J. M. Bowman, J. Am. Chem. Soc. **136**, 5888 (2014).

21. H. Liu, Y. Wang and J. M. Bowman, J. Phys. Chem. B **117**, 10046 (2013).

22. M. Rossi, M. Ceriotti and D. E. Manolopoulos, J. Chem. Phys. **140**, 234116 (2014).

23. F. Paesani and G. A. Voth, J. Chem. Phys. **132**, 014105 (2010).

24. A. Witt, S. D. Ivanov, M. Shiga, H. Forbert and D. Marx, J. Chem. Phys. **130**, 194510 (2009).

25. S. D. Ivanov, A. Witt, M. Shiga and D. Marx, J. Chem. Phys. **132**, 031101 (2010).

26. S. Jang, A. V. Sinitskiy, and G. A. Voth, J. Chem. Phys. **140**, 154103 (2014).

27. B. J. Braams and D. E. Manolopoulos, J. Chem. Phys. **125**, 124105 (2006).

28. T. J. H. Hele and S. C. Althorpe, J. Chem. Phys. **138**, 084108 (2013).

29. M. Ceriotti, J. More, and D. E. Manolopoulos, Comput. Phys. Commun. **185**, 1019 (2014).

30. S. Plimpton, J. Comput. Phys. **117**, 1 (1995).

31. H. Bakker and J. Skinner, Chem. Rev. **110**, 1498 (2010).

32. Y. Wang, X. Huang, B. C. Shepler, B. J. Braams, and J. M. Bowman, J. Chem. Phys. **134**, 094509 (2011).

33. F. Paesani, S. S. Xantheas, and G. A. Voth, J. Phys. Chem. B **113**, 13118 (2009).

Chapter 4.

The Vibrational Spectra and Relaxation Dynamics of Ice

In this chapter, we will present three applications using the ab initio WHBB PES and DMS and the quantum Local-Monomer model on ice. Section 4.1. will focus on the infrared spectra of ice Ih and amorphous solid water using the WHBB potential energy and dipole moment surfaces and the Local-Monomer Model. Section 4.2 will discuss the vibrational density of states of ice Ih and compare with inelastic neutron scattering experiments. Section 4.3 will show the studies on vibrational energy relaxation dynamics from the excited OD/OH stretch of in dilute HOD in ice Ih. A detailed analysis of the relaxation pathway is presented.

4.1. Infrared Spectra of Ice Ih and Amorphous Solid Water

4.1.1. Overview

The Infrared spectra of ice have been of great interest for experimentalists[1-6] and theorists[7-19] for more than half a century. It has been discovered that the IR

spectra strongly depend on the structures of ice. Therefore, spectroscopists use IR spectra as a probe of ice structures, often with a focus on the OH-stretching region.[3-6] The complex hydrogen-bonding network in these systems makes it very challenging to interpret the spectra and thus the analysis requires high-level theoretical approaches.

In 1970-80s, Rice and co-workers modeled spectra for several condensed phase water systems, including hexagonal ice (Ice Ih), amorphous solid water (ASW) and liquid water.[7-11] The OH stretches were treated as one-dimensional oscillators, while the intra- and intermolecular coupling between OH bonds were described semi-empirically. From these calculations, the intermolecular interactions were considered as a major factor to the peak positions and shapes of ice spectra and the calculated stretching states successfully overlapped the experimental frequency range. Buch, Devlin and co-workers approached the condensed phase water by focusing on large water clusters.[12-15] Using the TIP4P water potential and the local-mode model in an exciton model to describe intermonomer OH-coupling, a clear size dependence of the minimum cluster structure and OH-stretching IR spectra was identified. This dependence is illustrated with both simulated and experimental decomposed spectra of core, subsurface and surface parts of water clusters and recently supported by an experiment.[20] Inspired by earlier work of Buch and co-workers, Skinner and co-workers approach this research using a

QM/MM approach where the OH-stretch of monomers (treated quantum mechanically) are perturbed by the electric field of the surrounding monomers and where the monomer dynamics are otherwise treated using classical molecular dynamics with the TIP4P potential plus a semi-empirical rigid monomer 3-body interaction, confirming the strong intermolecular coupling between OH bonds in crystalline ice.[17,18] Morita and co-workers also use a QM/MM method and calculated the sum frequency generation spectra at ice surface.[19]

The fundamental of the bend appears as a prominent feature in the IR spectrum. In addition, the bend overtone has been observed experimentally in the IR spectra of hydrated ion clusters.[21-24] The perturbed local-mode models briefly reviewed above has the monomer bend frozen and thus are silent on these aspects of the IR spectrum. Previous very approximate calculations concluded that the $2\nu_b$ frequencies are $\sim$200 cm^{-1} higher than stretching frequencies and thus have only has small effect to the stretching band on H_2O systems, while the effect is larger on D_2O systems.[9-11] However, these conclusions are limited by the approximations in the water potential and the local-mode model. Fully coupled quantum calculations including the three intramolecular modes are thus desired to extend the coverage of the IR spectrum of water.

4.1.2. Ice Models

Two ice models are considered here and their construction used two different recipes. For the hexagonal ice Ih the initial structure of 192-mer was taken from the model created by Hayward and Reimers,[25] and then locally optimized on the WHBB potential. As expected, the original perfectly crystalline structure becomes disordered on the surface. The OH bonds at the surface reorient to form H-bonds, whereas the monomers in the core still maintain a crystalline arrangement. This structural preference is consistent with Buch's previous results.[15] (Figure 4.1)

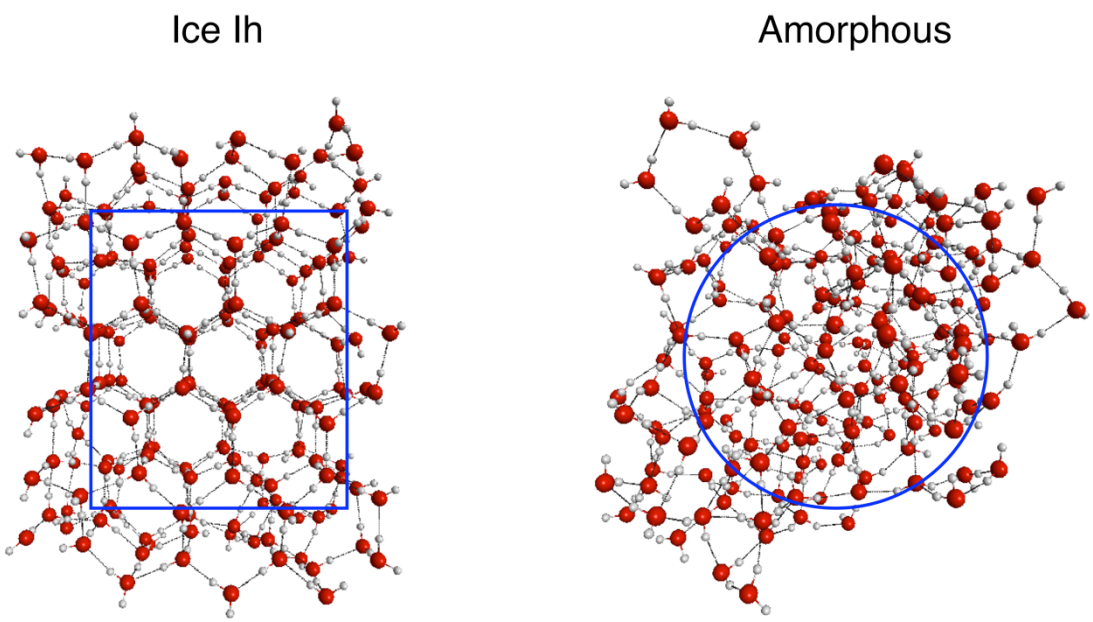

Figure 4.1. Local Minima structures of hexagonal and amorphous $(H_2O)_{192}$. The illustrative frames show the interior 105 and 100 core monomers selected in the

hexagonal and amorphous clusters, respectively.

It should be noted that this optimization is not a global one and so the resulting structure is not significantly different from the initial one. The second ice cluster is an amorphous one. It was created in a three-step process. First, 192 water molecules were place randomly in a $20A \times 20A \times 20A$ box, with some restrictions, using the software Packmol.[26] Second, unstable cluster was optimized using the empirical potential energy surface, AMOEBA, provided by Tinker.[27-28] Finally, this structure was optimized using the WHBB potential. The resulting configurations are shown in Figure 4.1, where "core" and "surface" regions for each cluster are indicated. These are described in detail below. The potential energy of the optimized amorphous cluster is -11.8 kcal/mol per monomer, which is slightly lower than the surface-disordered hexagonal cluster (-11.6 kcal/mol).

Local-monomer calculations were done for each monomer in each cluster. For each monomer IR transition intensities were calculated for the fundamental of the two stretch modes and the bend, and also for the overtone of the bend. Thus, for each ice cluster we obtained 768 IR intensities. As a first step in the analysis of results, we divided each cluster into core and surface regions, shown in Figure 4.1. To define a core of the hexagonal 192-mer, we first located the plane of a central slice perpendicular to the c-axis, a square frame is defined such that the maximum

number of tetrahedrally hydrogen-bonded monomers is included. Then, the 2-D frame is extended along the c-axis through the entire cluster, containing 120 monomers. This extension over-counted the under-coordinated monomers on the other two surfaces. After removing them, 105 monomers are left as "core monomers". For the amorphous cluster, according to the criteria that the distance between the oxygen and the center of the cluster is smaller than 8.5A, 100 monomers were defined as core monomers. Corresponding spectra for will be presented below.

4.1.3. Infrared Spectra

Next, we present local-monomer spectra and comparisons with experiment. First, we consider the region of the intramolecular bends. An experiment has reported this spectrum for the surface of crystalline ice at 120 K.[29] The calculated spectrum for 87 surface monomers from the hexagonal cluster, and the comparison with experiment is shown in Figure 4.2. On the top panel, the 87 intramoleclular bending modes from quantum calculation are shown as red sticks. To facilitate the comparison with experiment, the stick spectrum is smoothed with Gaussian line shapes as described above. We defer a discussion of this broadening to the end of this section; however, broadening was done to bring the calculated spectrum into registration with the experimental one. As seen, the calculated band center is in

excellent agreement with the experimental band, with both peaking at roughly 1650 cm^{-1}. The experimental shoulder at ~1690 cm^{-1} is qualitatively reproduced. Interestingly, the calculated spectrum does not extend as far to the blue, i.e., higher than 1725 cm^{-1}, as experiment. This could be evidence of combination bands of the pure bend plus an intermolecular mode. The involvement of such modes has been surmised in ice spectra,[14] however, such combination bands are not described by the present local-monomer calculations.

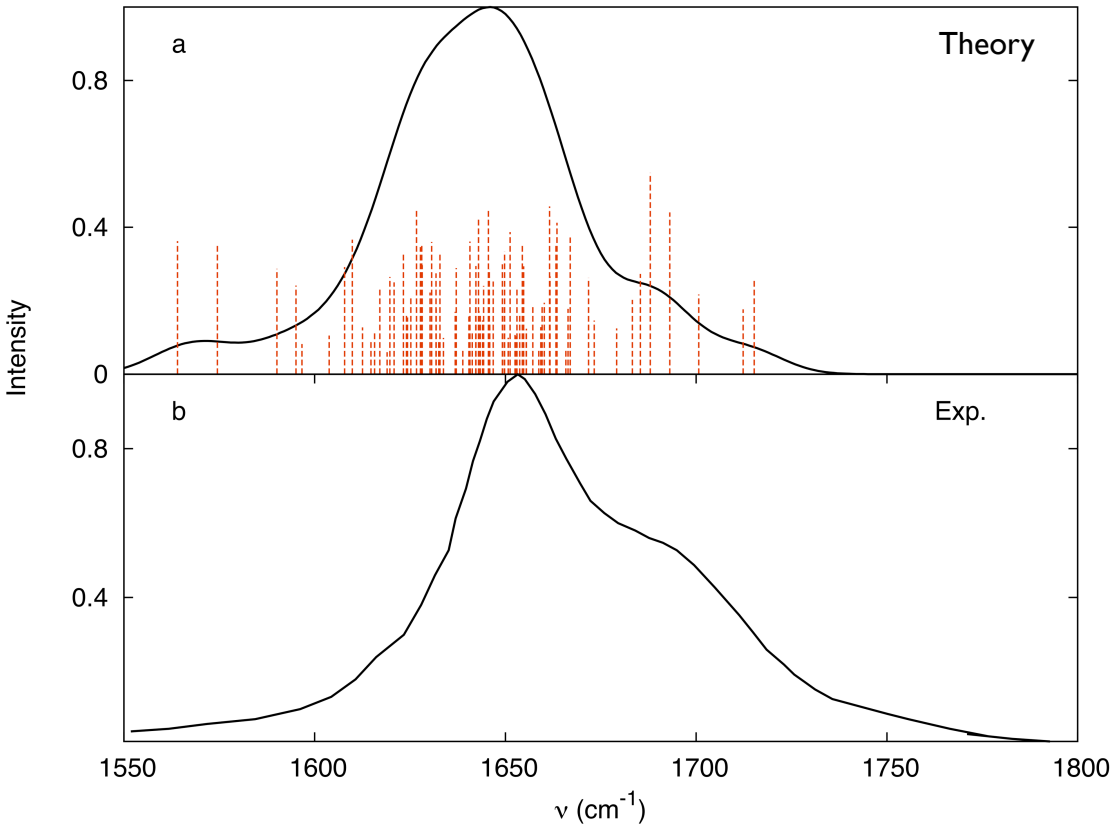

Figure 4.2. IR spectra of intramolecular bend modes of surface hexagonal ice. a) Local-monomer calculation for 87 monomers on the surface of 192-mer cluster. b) Experimental surface spectra in the bending region of crystalline ice at 120 K. (Ref.

42).

Next, consider the OH-stretch region of the IR spectra. In Figure 4.3, we show the calculated, Gaussian-broadened IR spectra of the hexagonal 192-mer for all, and the core and surface monomers. The decomposed spectra indicate that the group of surface monomers contributes solely to the 3700 cm^{-1} band, while at lower-frequencies, both groups contribute to this part of the band. Therefore, the 3700 cm^{-1} band is assigned to the mode of free OH stretching, which reaffirms the previous assignments.[29-34] Interior monomers are considered more analogous to water

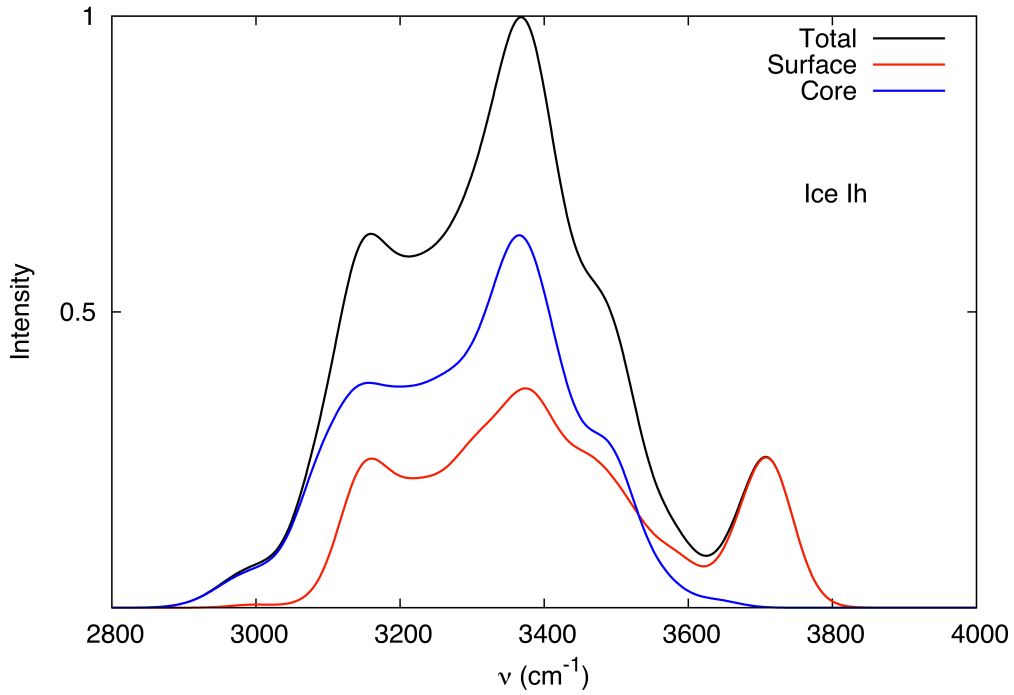

Figure 4.3. Total, surface and core smoothed IR spectra in the OH-stretching region of hexagonal 192-mer.

molecules in bulk ice in terms of the local environment, since the surface-area-to-volume ratio approaches zero as the cluster size increases from the finite to the bulk. Therefore, core monomers are used here to characterize the morphology of hexagonal and amorphous ice.

In Figure 4.4, we compare the calculated local-monomer spectra of core monomers with four available experimental spectra of crystalline and amorphous ice.[2,3,5] It should be mentioned here that the experimental spectra[3] in panel (b) is

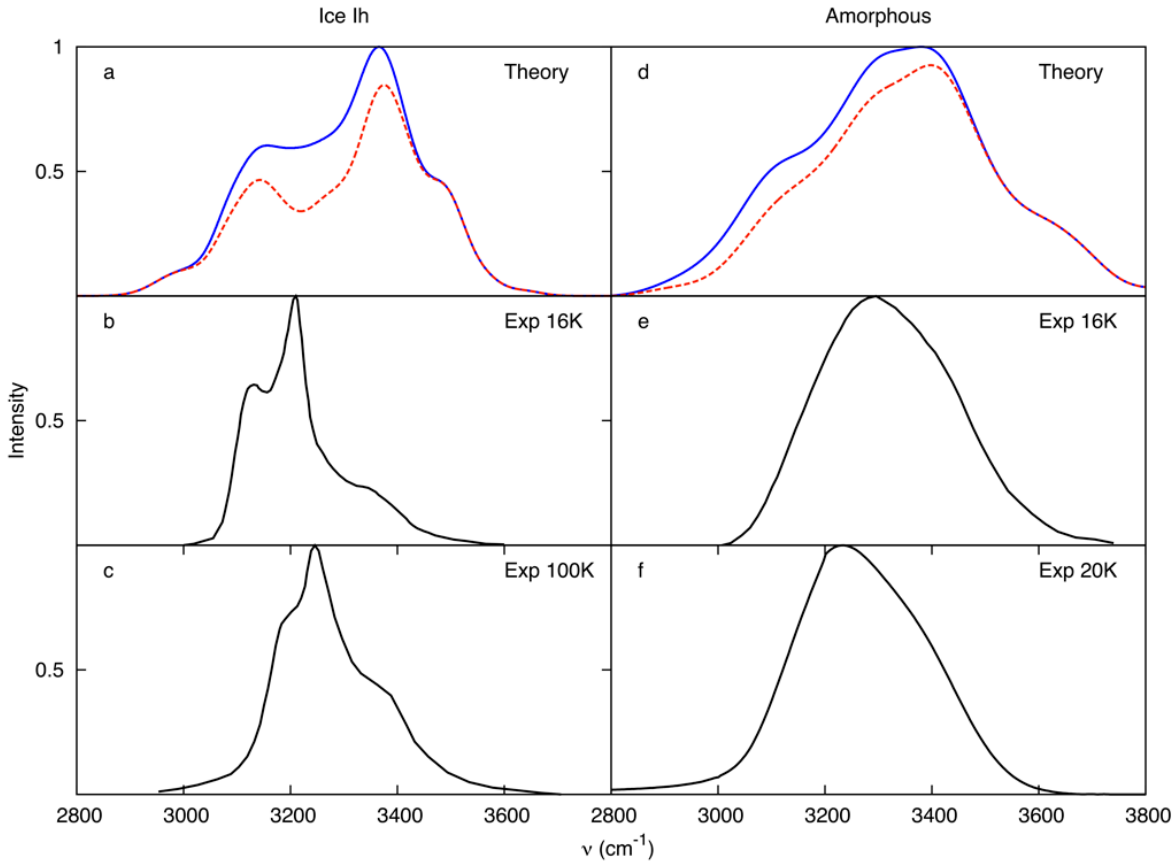

Figure 4.4. IR spectra in the OH-stretch region. (a) Theory. (b) Experimental crystalline ice at 16 K (Ref 3). (c) Experimental Ice Ih at 100K (Ref 2). (d) Theory (e) Experiment at 16K (Ref 3). (f) Experiment at 20 K (Ref 5). Blue solid lines in panels (a) and (d) are the calculated spectra with inclusion of the bending overtone. Red dashed lines are calculated spectra without the bending overtone. Black curves are experimental spectra.

measured for another crystalline form, namely cubic ice, which spectra is considered experimentally indistinguishable from hexagonal ice.[15] For the

amorphous ice, we compare our calculations with two experimental spectra, both reported for the "Amorphous Solid Water" form of amorphous ice.[3,5] It is important to keep in mind that the present clusters are approximations to the experimental ice samples, which contain elements of disorder ("proton disorder" in the case of Ih and random disorder for the amorphous ice). With this in mind, we conclude that the experimental IR spectra are well reproduced by the present calculations. The comparisons can be summarized as follows. 1) The calculated most red-shifted peak in ice Ih, at around 3150 cm^{-1}, agrees very well with the 16 K-experimental peak position. 2) The local-monomer IR spectrum of ice Ih is wider than the two experimental spectra. 3) The high-frequency peak of ice Ih at ~3380 cm^{-1} and the little shoulder to its right are present in the local-monomer spectra, although the positions are blue-shifted from experiments. 4) The relative intensity of the three peaks of ice Ih is in agreement with experiments. 5) The calculated spectrum for the amorphous ice shows broader and featureless characteristics, intuitively explained by the fact that the structure of this cluster is more disordered than Ih. 6) The peak position and the broader characteristics in the calculated spectrum for amorphous ice match the two experimental spectra at 16 K and 20 K quite well. 7) The overtone of the bend contributes to both spectra. The range of the bending overtone in the present calculations for Ice Ih (3200-3300 cm^{-1}) disagrees with the assignments from Hornig[1] (3140 cm^{-1}) and Rice[9] (3430 cm^{-1}). In addition,

the bend overtone does mix with the lower-energy stretch mode, especially in the range 3200-3300 cm^{-1}, and so even the spectrum shown in Fig. 5a without the bend overtone does contain the effect of this mixing.

The calculated spectrum in Fig. 5a agrees fairly well with one reported recently by Skinner and co-workers,[18] based on their coupled local-mode model, which we reviewed briefly above. Their results and the present ones show good overall agreement with experiment. Both sets of results focus on the strong intermolecular perturbations, albeit from different perspectives, and both sets of results show some differences with experiment. Here, while the three "bumps" are reproduced, there is roughly a 100 cm^{-1} blue-shift in the prominent peak in the Ih spectrum. There are several possible sources for this difference with experiment. One is the size and structure of the ice model used in the calculations. It is widely acknowledged that there is disorder in both ice forms considered here, as already noted. The present calculations consider one configuration for each ice cluster. For the amorphous ice spectrum, one could argue that a sufficient degree of disorder is already present in the single sample considered. Indeed, calculations we have done on smaller amorphous clusters of 96 monomers, with different configurations, certainly support this. In addition, the absence of structure in the calculated and experimental spectra appears to also support this argument. However, more investigation of the effect of different configurations is clearly

warranted as are studies with larger clusters so that the approach to the bulk can be examined. Hopefully, these can be done in the not-too-distant future. Also, there is the effect of temperature to consider. This can be accounted for theoretically; however, at the experimental temperatures of 16 and 20 K it seems to us that cluster size and configurations are more important and are of higher priority for future work.

4.1.4. Summary

We conclude with some comments about the two features seen in the ice Ih spectrum. We examined the perturbed, intramolecular lormal modes of the core monomers, as well as the VSCF/VCI mixing of the stretch and bend states of interest here. Based on that, we conclude that, in general, the lower-frequency feature is dominated by the perturbed in-phase monomer stretch mode and the bend overtone, which are also fairly strongly coupled to each other, whereas the higher frequency feature is dominated by the perturbed out-of-phase stretch mode. To be sure there is significant overlap of these modes across the band and we stress that these lormal modes and their mixings are strongly perturbed, via intermolecular potential coupling, from the isolated monomer modes. It should be noted again that the local-monomer model does not describe what we termed dynamical coupling to other monomers. Thus, by definition, the lormal modes are localized to

a single monomer. Delocalization is possible and this is incorporated approximately in the coupled-monomer theory we formulated and applied to small water clusters. For those clusters, delocalization was only seen for the highly symmetric tetramer and ring hexamer. Here the similarity of the lormal and normal mode double harmonic spectra was the evidence presented for the validation of the former. It would be of interest to apply the local-monomer model to D_2O and/or dilute HOD in D_2O where the assumption of monomer localization would appear to be very secure.

4.2. Vibrational Density of States of Ice Ih

4.2.1. Overview

Understanding the vibrational dynamics of ice is one of the central goals in ice research. The complexity in structures and molecular interactions, especially through hydrogen-bond networks, makes this study challenging for both experimentalists and theorists. Experimentally, infrared and Raman spectroscopy are the two most popular techniques to probe the vibrational properties of ice.[2,35-38] These spectroscopies are especially useful for studying the intramolecular vibrations of ice.[37,38] However both techniques are limited in the low frequency region.[2,35,36] This is due to IR and Raman selection rules specifically for ice,[39] and in general, the intensities are governed by the well-known matrix elements and

selection rules and so they do not "report" the entire vibrational density of states (DOS). Inelastic neutron scattering (INS) spectroscopy can, in principle directly provide the complete vibrational DOS, and thus is more direct tool for obtaining this important quantity. The INS spectra of several phases of ice have been measured,[39-47] including hexagonal ice (ice Ih),[39-43] which is the focus of this paper.

Previous interpretations of the INS spectra were based on calculations using empirical model water potentials, mostly using rigid monomers, from 1970s-2000s.[44-50] Recently, density functional theory calculations (with several functionals) were undertaken by Li and co-workers to obtain the vibrational DOS of ice Ih in the range 0-3500 cm^{-1}.[51] These calculations used a 64-monomer super-cell and, in part, were aimed at addressing (and contradicting) the conjecture of two types of hydrogen bonding in ice proposed in the 1990s.[41,42] These calculations "overestimate" the vibrational frequencies, that is, they are systematically blue-shifted by roughly 100 cm^{-1} relative to experiment. In addition, the calculations show a doublet structure in the monomer bend and OH-stretch regions, roughly 1600 and 2800-3300 cm^{-1}, respectively, in qualitative disagreement with experiment for those bands. Shortly after those calculations were reported, Hirata, Xantheas and co-workers reported MP2/aug-cc-pVDZ calculations of the harmonic vibrational DOS (and IR and Raman spectra).[55] They also employed a super-cell of 64 monomers, which was subjected to external self-consistent charged environment

using the binary interaction method (BIM).[56,57] In this method the electronic energy of water monomers is obtained by one and two-body interactions in a periodic lattice, perturbed by the electric field of surrounding charges. These calculations obtained the geometry of ice Ih in very good agreement with the value inferred from experiment. In addition, the calculated vibrational DOS is overall in good agreement with experiment, with the exception of not getting the sharp peak in the experimental spectrum at roughly 60 cm^{-1}. As expected with the harmonic approximation, the peaks in the monomer bend and OH-stretching regions are substantially blue-shifted relative to experiment. As these authors noted, there are several sources of error in these state-of-the-art, direct calculations. To quote, these are the "inherent error in MP2 theory, a moderate basis size, embedded-fragment scheme and quasi-periodicity of the proton positions"). In addition, the authors noted the lack of anharmonicity in their calculations. Other important approximations of the model include 1) using a modest size cluster of 64 water monomer and 2) not explicitly including a 3-body potential. This group also focused on the two now-"infamous" experimental peaks in the INS at 229 and 306 cm^{-1} and also concluded that they are not signatures of two types of hydrogen bonding.

Inspired by the steps taken by Hirata, Xantheas and co-workers, we were motivated to extend our recent study of the IR spectra of ice Ih and amorphous solid

water in the monomer bend and "O-H stretch" regions,[58] to a calculation of the vibrational DOS of a model for ice Ih. As with the earlier calculation, we use a 192-monomer model with the *ab initio* WHBB potential energy surface,[59] which is briefly reviewed below. A group of 105 core monomers has been selected[58] and is also used here for the vibrational analysis. The results from this smaller core cluster are considered under the assumption that they are the ones directly comparable to the INS experimental data.

Specifically, we calculated the vibrational DOS in the range 0-4000 cm^{-1}, using standard and local harmonic normal-mode analysis and also using the coupled, anharmonic local-monomer model in the range 1500-4000 cm^{-1}. We use LMon-3 here and the bend and two OH stretches are coupled, as reviewed in Chapter 3. In addition, we calculated the vibrational DOS for pure D_2O and compare both spectra with experimental INS spectra. The character of the vibrational states in different frequency ranges is analyzed from the normal-mode eigenvectors. A short summary and conclusions are given in the last section.

The paper is organized as follows. The computational details are given in the next section. This consists of a brief review of the WHBB potential and the 192-model of ice Ih using it. Then details of the harmonic and coupled-anharmonic calculations of the vibrational DOS are given. The results and comparisons with experiment are given in Section III. An analysis of the normal mode eigenvectors is

also given in that section with the aim of assigning the nature of the modes in four regions of vibrational DOS spectrum.

4.2.2 Full Normal Mode Analysis

With the *ab initio* potential energy surface in hand, performing a normal-mode analysis is a straightforward, almost trivial task compared to a direct *ab initio* calculation of the force constant matrix (and subsequent trivial diagonalization), e.g., the recent one carried out by He *et al*.[55] A standard finite-difference approximation was used to evaluate the mass-weighted Hessian of the 192-mer and 105-mer clusters. For both calculations, every monomer is included in the Hessian calculation, so the matrix dimension is 1728 for the former and 945 for the latter cluster. Diagonalization of the mass-weighted Hessians generates 1728 and 945 harmonic frequencies and corresponding mass-weighted normal mode eigenvectors, respectively.

4.2.3. Results and Discussion

Table 4.1. Geometry of the model ice Ih with standard deviation in parentheses and comparison with experiment.

	Exp[a]	192-mer	core 105-mer

O-H length(A)	0.985 (0.006)	0.971 (0.007)	0.973 (0.005)
O-O length(A)	2.75	2.77 (0.06)	2.74 (0.05)
HOH angle (deg)	106.6 (1.5)	104.8 (1.7)	104.8 (2.0)

[a] Taken from reference 55.

The structure of the optimized hexagonal 192-mer is shown in Figure 4.1. The 105 monomers that define the core region are highlighted. There is considerable relaxation at the periphery of the cluster, owing to substantial relaxation of the free O-H stretches there. Average O-H, O-O distances and monomer bond angles for both for the entire cluster and the 105-core region are given in Table 4.1, along with comparisons with experiment. (Recall that the core region consists of monomers that do not have any free O-H-stretch modes, as described in detail in ref. 27.) The calculated results are an average over all the monomers and the standard deviations are also given. As seen, the 192-mer and the core 105-mer do not show significant differences. They agree reasonably well with the experimental values, which are taken from a compilation given in ref. 55. In considering these comparisons it is perhaps worth making several points. First, the experimental values are for samples at non-zero temperature and thus represent averages for zero-point plus thermal motion. Second, some adjustments

were made to the "direct measurements" for the O-H (actually O-D) distance based on experiments in the liquid phase. The O-D internuclear distance for Ice Ih was reported as 0.976 A;[60] however, after making an adjustment to account for interference terms, by which the "the apparent O-D distance in liquid water increases by 0.009 A.", the reported value for Ice Ih is 0.985 A, assuming the same "correction" applies. This is the result shown in the table. We do not question that value; however, it may be that the standard deviation of (0.006 A) is an underestimate of the true uncertainty. Other values for the core region are in closer agreement with experiment. We note that the structures reported by He *et al*. are in excellent agreement with the experimental values shown in the table. Given the uncertainties in making these comparisons, we suggest caution in making conclusions about the accuracy of one method over another. However, we do note that WHBB does not incorporate many-body effects beyond three. It is worth noting that for an isolated water molecule the equilibrium O-H distance and H-O-H angle are 0.958 A and 104.5 deg, respectively.[61] That the equilibrium O-H distance increases by roughly 0.02 A in ice is both significant and understandable given the strong H-bonding interaction.

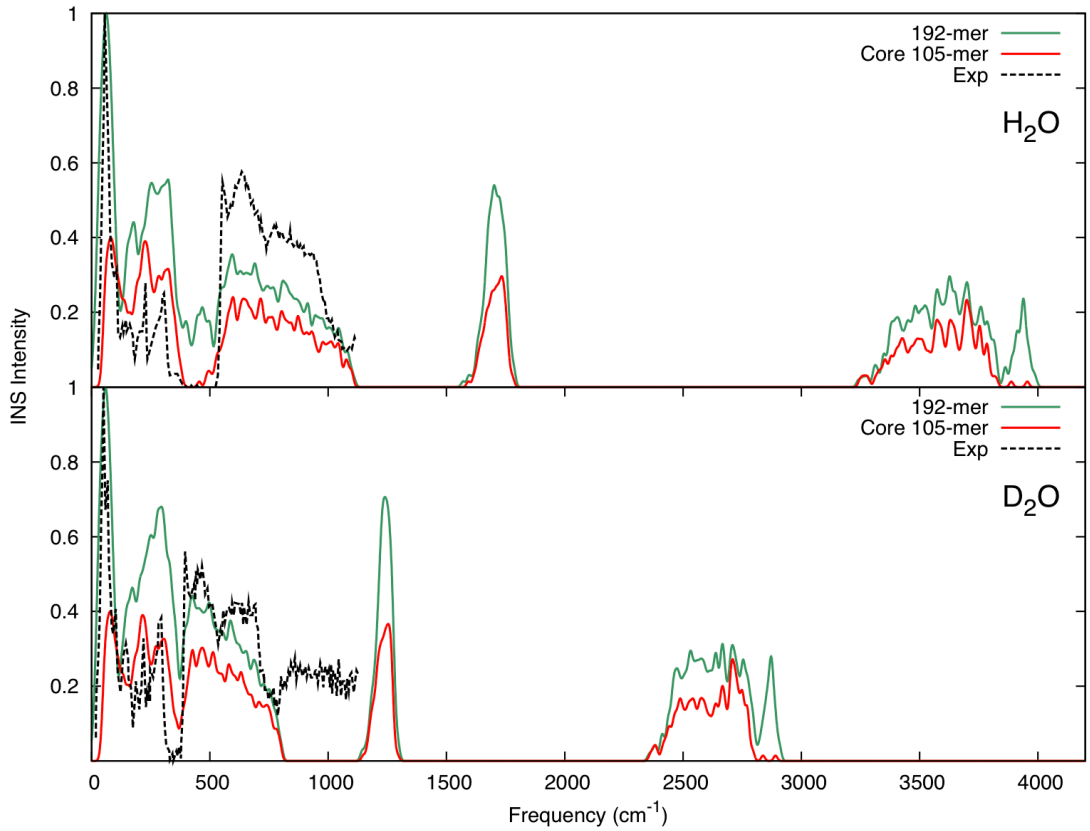

Figure 4.5. Vibrational density of states of H_2O and D_2O ice Ih in the range 0–4200 cm^{-1}: calculated 192-mer (solid green curves), calculated core 105-mer (solid red curves), and experimental inelastic neutron scattering digitized from figure 2 of reference 10 (dashed curves). The 192-mer and experimental intensity is normalized to unity. The intensity of core 105-mer is in the same scale of the 192-mer.

Next, consider the vibrational DOS. We show these from harmonic normal-mode analysis for the 192- and 105-mer clusters and compare the results

with inelastic neutron scattering experiments[10] in Figure 4.5. We show results from both clusters since similarities and differences presumably reveal features of the surface of the 192-mer cluster not present in the core. Before making detailed comparisons between theory and experiment, we note that the INS experiments are energy transfer cross sections over a range of scattering angles and in principle report on all fundamental, combination, and overtone transitions in the energy range indicated. However, the expectation is that fundamental transitions are the most probable ones, and since the experiments were done at 15 K, contributions from hot bands can be neglected. The calculations are for the harmonic fundamental excitations and the thus these differences with the INS experiment should be kept in mind when comparing theory and experiment. Also, the calculated stick spectra are broadened by a Gaussian function in order to roughly match the experimental widths. Finally, on the matter of normalization, we normalized the maximum in the INS scattering intensity to 1.0. The maximum in the 192-mer DOS is also set to 1.0, and as seen in Figure 4.5 both of these spectra have their maximum at the lowest energy peak. However, as discussed below, we believe that this apparent agreement *may* be fortuitous. The normalization of the core 105-mer was set differently so that the DOS in the O-H stretch region agrees roughly with 192-mer one, instead of normalizing to the lowest-frequency peak. The reason for not doing that is we believe that peak intensity is not well converged

for the 105-mer. This is discussed in more detail below. With these remarks in mind, we note that the present calculations are in good agreement with experiment, starting with the three prominent peaks in the frequency region below 400 cm^{-1}. The lowest frequency peak from experiment is at roughly 60 cm^{-1} and the calculated peaks are both at roughly 70 cm^{-1}. The previously-mentioned controversial features in the region below 400 cm^{-1} are the two peaks at 229 and 306 cm^{-1}.[41,42,54,55] The calculated vibrational density of states does show two peaks at 226 and 316 cm^{-1}, in fortuitously excellent agreement with experiment. More discussion of these peaks, based on an examination of the normal modes is given later. Also, below roughly 400 cm^{-1} the calculated and experimental spectra of H_2O and D_2O are nearly identical; this is a consequence of the nature of the normal modes in this region of the spectra, also as discussed below and also previously in the literature.[39,42] The gap seen in the H_2O spectrum between roughly 400 and 550 cm^{-1} is also seen in H_2O INS experiment. There is a small peak between roughly 450 and 550 cm^{-1} seen in the calculation. In the D_2O spectrum the gap is narrower with significant intensity at roughly 400 cm^{1} instead of roughly 550 cm^{-1}. That the ratio of these two values is roughly $2^{1/2}$ is not an accident and signals a qualitative change in the nature of the dominant normal modes. We return to this below. The calculated libration bands are in good agreement with experiments. The H_2O libration band starts from 510 cm^{-1} and ends at 1114 cm^{-1}, which lines up with the experimental assigned band in

the range 548-1008 cm^{-1}.[42] The D_2O libration band is narrower, extending from 368-618 cm^{-1}, which is in good agreement with the experimental assignment of 395-710 cm^{-1}.[42] The first intramolecular vibrational band for H_2O is the bend at 1550-1700 cm^{-1}, followed by the O-H stretch at 3200-3800 cm^{-1}. D_2O has the expected shift to the red of about $2^{1/2}$. The intramolecular bend band is at 1100-1250 cm^{-1} and stretch is at 2400-2800 cm^{-1}. We discuss the intramolecular vibrations in detail below.

Overall, the core 105-mer DOS are in better agreement with experiment than the 192-mer one, except for the lowest energy peak, where the 192-mer spectrum *appears* to be in better agreement with experiment. Comparing the two calculated spectra, we note two major differences. First, as expected, the 192-mer shows the signature of "free-OH" states at ~3800 cm^{-1}. Second, the 192-mer has a higher density of states at the lowest frequency peak at roughly 60 cm^{-1} (in fortuitously good agreement with experiment). An inspection of the corresponding normal modes indicates that this apparent shift in the direction of experiment is *probably* a surface effect, i.e. an artifact of the less confined surface monomer. Further, it is likely the vibrational DOS for 105-mer has not fully converged this peak. As we shall discuss later, the modes below 400 cm^{-1} are due to monomer "translations" and librations and it likely that these converge slowly with cluster size. We examined the vibrational DOS for a smaller 34-core cluster embedded in a 96-mer and indeed

find that the lowest energy peak is relatively smaller in intensity than in the 105-mer core.

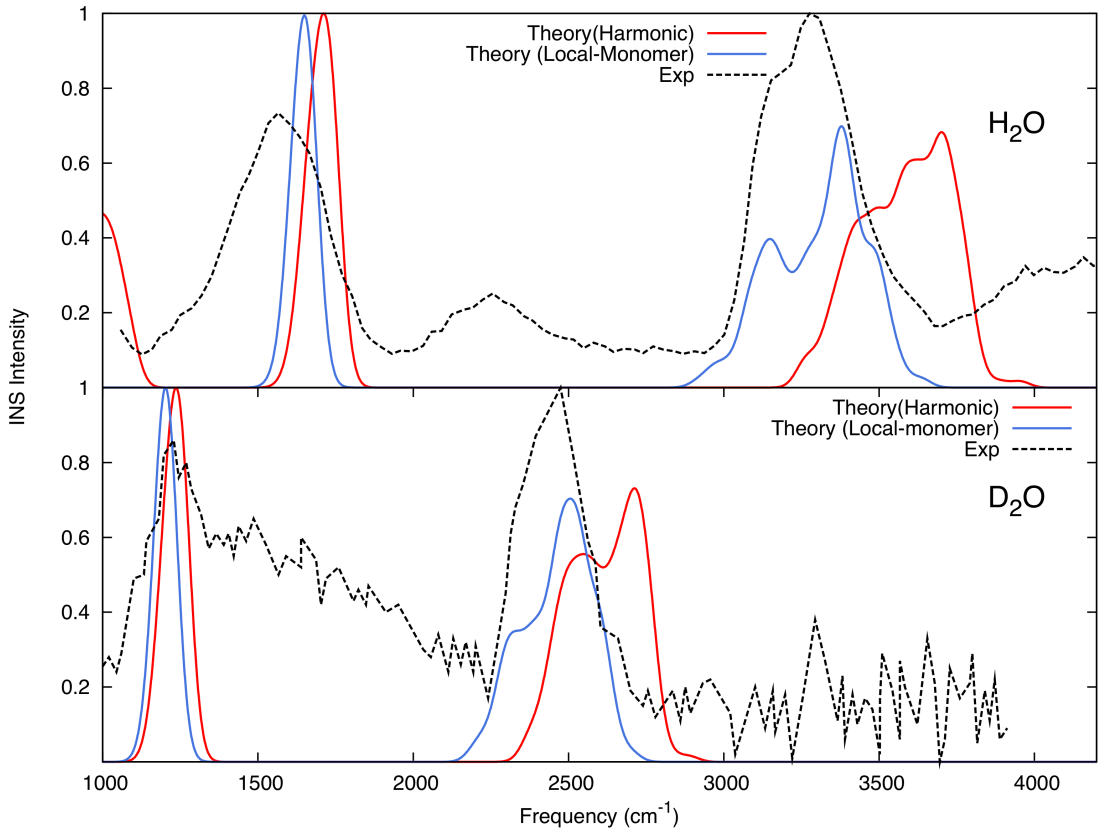

Figure 4.6. Vibrational density of states of H_2O and D_2O ice Ih in the range 1000–4200 cm^{-1}: calculated harmonic and local-monomer from the core 105-mer (solid curves) and experimental inelastic neutron scattering (dashed curves). INS data are digitized from reference 10. H_2O is from Figure 6, D_2O is from Figure 10 with H_2O < 0.5%. Some small peaks in this spectrum are due to this H_2O contamination. Each curve is normalized to one at the maximum intensity.

Next, consider the high-frequency monomer bend and O-H stretch region. The harmonic and local-monomer vibrational DOSs for H_2O and D_2O are shown in Figure 4.6, along with comparisons to the INS experiments. To be clear, we note that the LMon DOS in the O-H stretch region includes only the O-H stretch fundamentals. As seen, the harmonc, LMon and experimental peaks in bend regions for H_2O are 1710, 1650 and 1565 cm^{-1}, respectively. Note; however, the large difference in the width of the calculated and experimental band. This and the prominent experimental peak at roughly 2200 cm^{-1} clearly indicate the presence of combination excitations in this region in the experiment that are not included in the calculations. Thus, these combinations excitation very likely account for the difference in the experimental and theoretical bandwidth of the bend region. Similar remarks apply to the D_2O bend region, where the corresponding peaks are all at roughly 1200 cm^{-1}. In this case the experimental bandwidth is even broader than the one for H_2O.

Consider now the the O-H and O-D stretch bands. For H_2O, the LMon two-peak band is in good agreement with experiment. The LMon peaks are 3148 and 3379 cm^{-1}, while the experimental ones are at 3202 and 3339 cm^{-1}. As expected, the harmonic results are substantially blue-shifted relative to experiment and the LMon peaks. Also, note the additional intensity in the experiment to the blue of the main features, which indicates, as with the bend, substantial intensity

from combination excitations (with low-frequency intermolecular modes), not present in the calculations. The vibrational DOS for the O-D stretch region of D_2O is analogous to H_2O with the expected isotopic shift. The LMon calculation shows two peaks at 2320 and 2505 cm^{-1}; the expermintal one is at ~2470 cm^{-1} and the harmonic peaks are roughly 242 cm^{-1} blue-shifted from the LMon ones. Note that the lower energy peak in the theoretical spectra is less pronounced than the one seen for H_2O in rough accord with experiment where the smaller peak in experiment for H_2O is evidently not resolved for D_2O.

It is of interest to compare the present theoretical and published experimental results for the vibrational DOS in these monomer bend and stretch regions to the corresponding IR spectra. We presented a comparison of these IR spectra recently using the 192 and 105-mer models used here.[58] While these spectra all show very similar band structures, the peak positions are, not surprisingly, not the same. The experimental peaks are: (1565, 1653 cm^{-1}), (3202, 3131 cm^{-1}) and (3339, 3209 cm^{-1}), where the first entry in each pair is from 15 K INS spectrum and the second is from 16 K IR spectrum. The corresponding calculated results are: (1650, 1648 cm^{-1}), (3148, 3157 cm^{-1}) and (3379, 3365 cm^{-1}). First, consider the experimental results. There is a ~ 90 cm^{-1} red-shift in going from the IR to the INS results for the bend and ~45 and 130 cm^{-1} blue-shifts for the corresponding O-H stretch peaks. The calculated results show, in contrast, small

shifts for the two spectra. Interestingly, the calculated peak in the bend band is closer to the IR peak than the INS one. The difference with the INS spectrum is probably due to the to the importance of combination excitations in the INS spectrum that are not present in the calculated one and the IR spectrum (which agree well in peak position and bandwidth). The calculated peak position for the lower-frequency O-H stretch is in good agreement with both experiments but somewhat closer to the IR one. The high-frequency O-H stretch peak is quite different in the experiments, and the present calculations are much closer to the INS experimental peak than to the corresponding IR one. So clearly, there is some sensitivity in the position of this peak that perhaps warrants more investigation, both experimentally and theoretically.

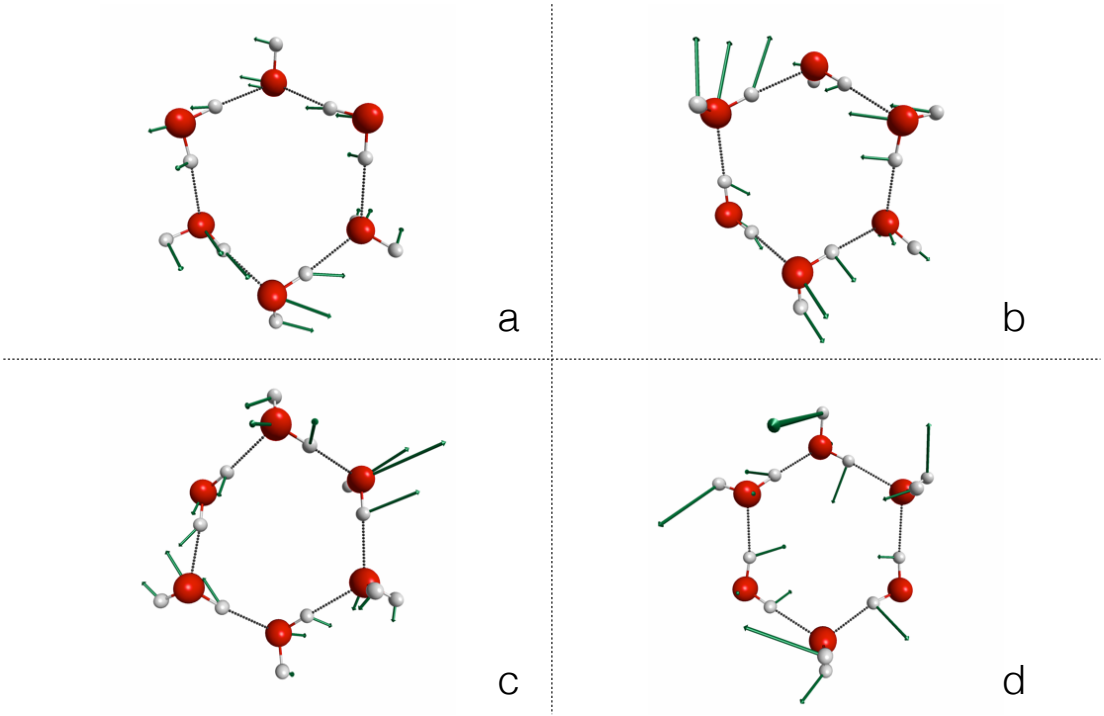

Figure 4.7. Visualization of four eigenvectors from the core-105mer. (representative 6-member rings are shown) (a) Acoustic "translational" mode at 67 cm^{-1}, (b) Optical "translational" mode at 229 cm^{-1}, (c) Optical "translational" mode at 314 cm^{-1}, (d) Librating mode at 662 cm^{-1}

Next, to give additional insight into of the nature of the vibrational modes of the H_2O core 105-mer ice model in the region below 400 cm^{-1}, four "zoomed views" of normal modes are depicted in Figure 4.7. These are not mass-scaled normal modes. This "unscaling" of the eigenvectors of the mass-scaled Hessian is done to

that the frustrated "translational" motion of each monomer is clear. It is important to note that each of the modes involves motion of all the monomers, of which the ones shown in the figures are representatives. Each mode corresponds to one of four prominent features in the spectrum peaks representative mode is selected at each of the three prominent peaks in the region below 700 cm^{-1}. A close inspection of the three lowest-frequency modes indicates that each monomer is displaced in a translational fashion; however, the collective monomer motion differs. The mode at 67 cm^{-1} is from the first peak in the DOS and, as seen, the monomer motion is essentially in-phase translational motion of monomers, or "acoustic mode". The mode at 229 cm^{-1} also shows features of monomer translation. The difference is the angle between the vectors of some neighboring monomers are greater than 90 degree. This trend becomes more prominent in the mode at 314 cm^{-1}. This feature characterizes the out-of-phase monomer translation, and corresponds to "optical modes". Compared with the three "translational" modes, the librational mode at 662 cm^{-1} shows less displacement of oxygen atoms and more hydrogen atom motion. The collective motion can be characterized as rotation of each monomer around a axis almost through oxygen atoms. This motion is usually referred as "hindered rotation of water molecules" because they cannot freely rotate like molecules in gas phase due to the H-bonding constrains. This has been discussed in detail in ref. 62. Eigenvectors for bend and stretch modes on each monomer are similar to the ones

of gas molecules and so are not shown.

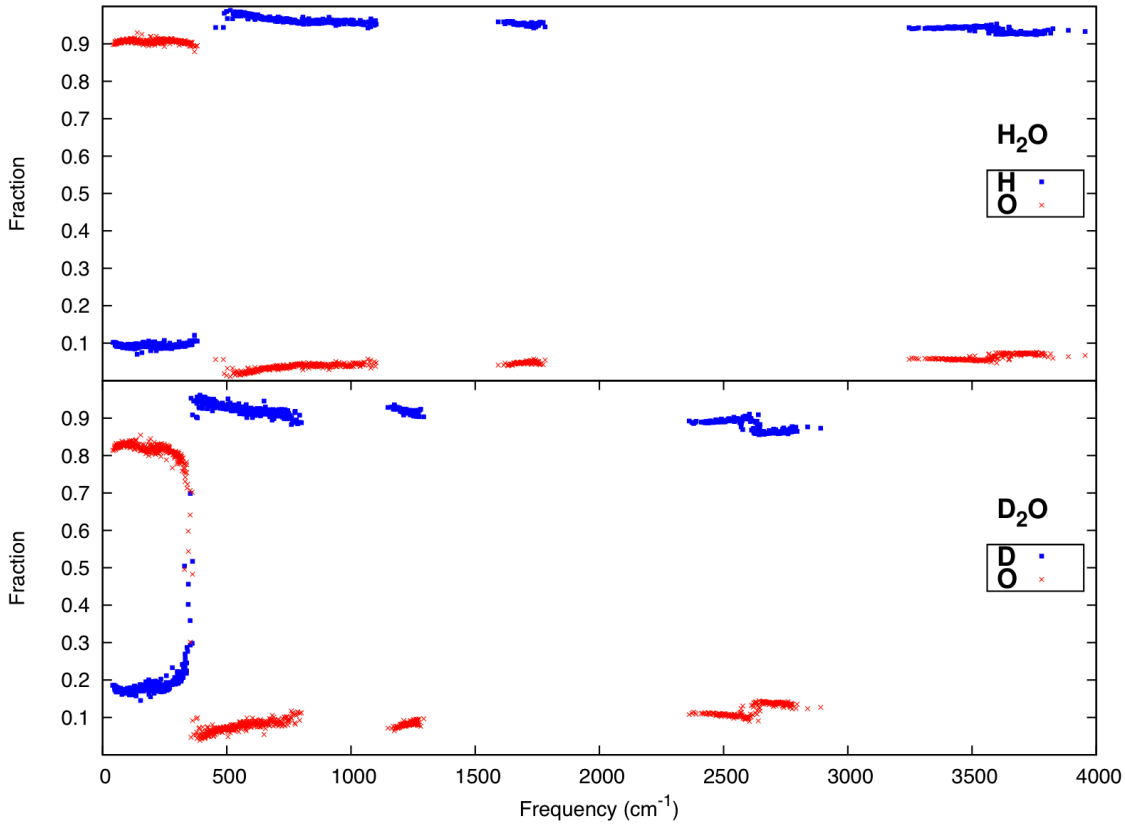

Figure 4.8. Fraction of mass-weighted normal mode eigenvectors projections on O and H (D) atoms for the core 105-mers as function of the corresponding harmonic frequency.

Finally, we present a quantitative characterization of the mass-scaled normal modes, which are all of unit norm. This is done by simply summing the squares of the O atom and H(D) atom contributions to a given normal mode. The results are given in Figure 4.8 for the core 105-mer for H_2O and D_2O. At overview of these

figures shows a clear boundary between modes dominated by O-atom motion and H-(D-) atom motion. For both H_2O and D_2O there is a common boundary at roughly 400 cm^{-1}. Below roughly 400 cm^{-1}, the normal modes are, as noted already, essentially motion of the monomers, the mass of which is mainly given by the O atom. (The slightly larger contribution of the D-atoms in this region compared to H-atom is simply due to the larger contribution of the D-atoms to the monomer mass.) Above 400 cm^{-1}, the light atoms, H or D-atom motions dominate the normal modes, even in the mass-weighted eigenvectors. Also, the narrower gap in the D_2O DOS above 400 cm^{-1}, seen in Figure 4.5, versus H_2O correlates exactly with the projection gaps shown in Figure 4.8. And, as expected, the "blue-edge" of the H_2O frequency-gap comes at a frequency that is roughly $2^{1/2}$ the corresponding value for D_2O.

4.2.4. Summary

The vibrational density of states of H_2O and D_2O ice Ih for a 192-mer and 105-mer core region have been presented, using the *ab initio* WHBB potential energy surface. The harmonic VDOS were presented in the range 0-4000 cm^{-1} and coupled-anharmonic DOSs were presented in the monomer bend and O-H and O-D stretch regions. The calculated spectra show good agreement with Inelastic Neutron Scattering experiments. In particular, the density of states from the core

105-mer reproduce the three prominent experimental peaks below 400 cm^{-1}, however, the intensity of the lowest frequency peak is probably not well-converged. Four examples of normal modes for H_2O ice below 1000 cm^{-1} were given to illustrate the character of monomer motions. The visual and the quantitative analyses of the normal-mode eigenvectors shows the below 400 cm^{-1} the vibrational states are monomer translational motion, and modes above that are mainly due to hydrogen (deuterium) motion. This is consistent with the fact that below 400 cm^{-1} the H_2O and D_2O are nearly identical, whereas above a $2^{1/2}$ isotopic shift appears in spectra.

These calculations and comparisons with experiment also show that the accuracy of the WHHB PES extends to the lowest frequencies of interest for ice Ih. It is worth noting that the present results appear to capture the fine details of the experimental INS spectra, e.g., the two peaks at 229 and 306 cm^{-1}, more accurately than previous calculations using the TTM3-F semi-empirical potential.[63]

4.3. Vibrational Energy Relaxation of Dilute HOD in Ice Ih

4.3.1. Overview

The dynamics and spectroscopy of vibrational excitation and relaxation in liquid and solid water are a central research theme in Chemistry, both experimentally[64-76] and theoretically.[77-81] The ability to dope neat water with HOD in dilute amount has opened a window on this research by isolating the excitation and relaxation to this

dopant. This had lead to a number of important experimental and theoretical studies of this system in particular.[67-79] Simplified interpretations of HOD vibrational relaxation invoking two modes, e.g., the initially excited OH stretch and the OO stretch in the H-bond network, as described by the phenomenological Lippencott-Schroeder (L-S) potential,[82] have recently been reported in connection with state-of-the-art 3D IR experiments.[76] This simplified description, which was applied successfully, is at odds with the alternate analyses of Rey and Hynes,[77-78] and Lawrence and Skinner,[79] albeit in the context of relaxation in the liquid phase. These analyses suggest a more complex relaxation pathway involving intramolecular as well as intermolecular modes. These seminal works invoked perturbative treatments of couplings together with experimental data to obtain relaxation times in reasonable agreement with experiment. Ultrafast resonant vibration-to-vibration (VV) transfer of H_2O in neat water has been investigated using a quantum harmonic model by Poulsen et al.[80-81]

Given the surprising success of the recent application[76] of the two-mode L-S potential, we undertook state-of-the-art ab initio quantum calculations of the vibrational relaxation of HOD in ice and present the results in this Communication. The calculations are in very good accord with experiment and elucidate the relaxation pathways.

4.3.2. Computational Details

We apply the LMon Model and the WHBB PES here, to study vibrational energy relaxation. We do this considering up to six of the nine local normal modes of one HOD monomer embedded in the ice Ih model of 116 monomers. We perform LMon-6 calculations for the embedded HOD monomer. The formulation of LMon-6 is described in Chapter 3. Note the position of the HOD is the center of the cluster and thus the HOD is fully H-bonded. Experimentally there is no such uniquely defined location, of course. We comment on this briefly at the end and describe future work to investigate site inhomogeneity.

First, we present calculated three-(intramolecular)-mode HOD fundamental and overtone OD and OH-stretch excitation energies in the gas phase and in ice Ih, obtained with a small VCI basis of order 729 and compare to experiment in Table 4.2. Agreement with experiment for isolated HOD is excellent; this is expected because the monomer potential is, as noted above, of spectroscopic accuracy for isolated H_2O.[83] Much more significant is the agreement with experiment for the fundamentals of HOD in ice. This level of agreement is further validation of the accuracy of the current approach. Note the large red-shifts (437 and 304 cm^{-1}) from the gas-phase of OH and OD-stretch fundamentals. This is consequence of the strong hydrogen bonding of these modes in the ice environment. It is also important to note that the eigenstates of these fundamentals and overtone states

are quite pure in both the gas-phase and 3-mode embedded cases. (The VCI expansion coefficients are given in the SI.)

Having validated the approach for the HOD fundamentals and overtone in ice, the goal is to study the vibrational relaxation. Since it is known experimentally that this relaxation is in the sub-picosecond timescale (and clearly does not involve a simple VV resonant relaxation), we reasonably

Table 4.2. Energy differences in cm^{-1} of gas HOD and HOD in ice Ih from 3-mode MULTIMODE (MM) calculations and experiments.

	n_{f-i}	Gas MM	Gas exp	Ice Ih MM	Ice Ih 2D-IR[a]
OD(v)	1-0	2723	2724	2419	2415
	2-1	2640	2640	2315	2251*
OH(v)	1-0	3707	3707	3270	3279
	2-1	3536		3087	3123*

a. Ref. 12. *Estimated from the experimental band.

assume, as others have,[75-78] that the relaxation is via coupling to localized intermolecular modes and so the local monomer description of these modes should be reasonable. The six intermolecular modes along with three intramolecular ones are given in Figure 4.9, along with the harmonic frequencies. Including all 9 modes

in a fully coupled calculation is too computationally intensive and so proceeded as follows. We began by adding one intermolecular mode at time to the 3-mode calculation and investigated the level of mixing in the eigenstates of the corresponding Hamiltonian. Based on this approach, we found that 6-mode calculations provide reasonably converged results. The 6-mode calculation is done with a 24 199 VCI basis. Details of the intermolecular mode couplings are presented in the SI.

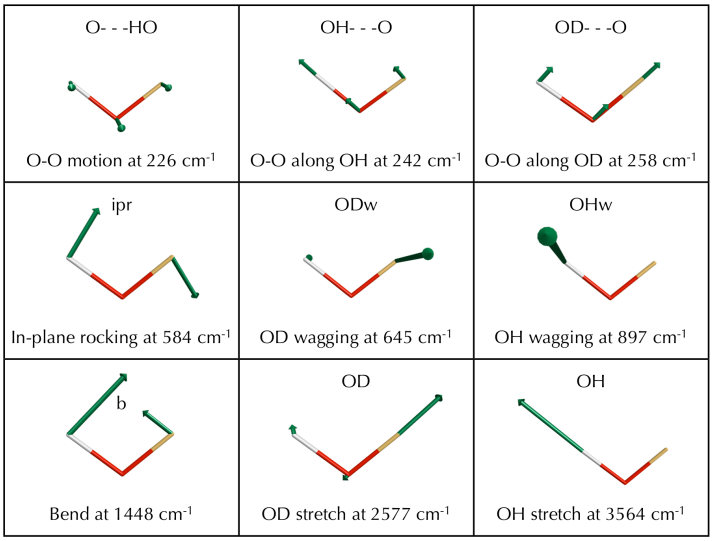

Figure 4.9. Depiction of all local-normal modes of the HOD monomer in ice environment. Abbreviation at top. Full description and harmonic frequency at bottom.

4.3.3. Vibrational Relaxation Lifetimes and Pathways

The dynamics of OD/OH relaxation is characterized by the time-dependent decay of the initial state population. This is shown in Figure 4.10 for the four initial states of interest. First, note the relaxation occurs in the sub-picosecond time frame and that the two overtones relax faster than the corresponding fundamentals. To quantify the relaxation time, we fit the data with mono- and bi- exponential functions, as suggested in previous experiments.[73-75] The fitted lifetimes are summarized in Table 4.3 and compared with experiments. (Details of data fitting are given in SI.) First, we see the lifetime for the OD and OH fundamentals agree well with both 2D-IR and pump-probe experiments. The lifetime of the OD overtone also agrees well with the recent 3D-IR experiment,[76] which as noted above used the 2-mode L-S model potential in wavepacket calculations to "successfully" capture this rapid decay. A fast relaxation rate on the order of 100 fs is seen for the OH overtone. No direct measurement of this has been performed so far. However, an estimate based on lineshape fitting also predicts extremely fast rate.[73]

Table 4.3. Lifetime (fs) of OD/OH (v=1 and v=2) from wavepacket calculations and experiments.

	n_{f-i}	This work[a]	2D-IR[b]	3D-IR[c]	Pump-probe
OD(v)	1-0	422,373	410		480[d]
	2-1	223,296		~200	
OH(v)	1-0	430,447	590		420[e]
	2-1	146,64			20[f]

[a]The two lifetimes at 0 K are obtained by fitting the population decay curves in Figure 4.10, using both monoexponential and biexponential functions (see SI), respectively. [b]Biexponential fit at 80 Kelvin, from Ref. 75. [c]Estimation at 258 K, from Ref. 76. [d]Monoexponential fit at 25 K, from ref. 74. [e]Monoexponential fit at 180 K from Ref. 73. [f]From ref. 73, an estimated value to fit the transient line shapes.

Also shown in Figure 4.10 are the populations of initially unpopulated virtual states. The expressions to obtain these are standard, but are given in detail in the SI. These are the detailed pathways for the vibrational relaxation. For the OH fundamental, as seen from Figure 4.10(b), the major pathway is $v_{OH} \rightarrow v_{ipr}+2v_b$, and subsequently to $v_{OD\text{---}O}+3v_{ipr}+v_b$. This short-time decay pathway is in accord with

Hynes[77,78] and Skinner[79], who proposed the relaxation of the OH stretch fundamental to the bend overtone in liquid phase. For the OD fundamental, the dominant relaxing pathway is the high overtone of intermolecular OD wagging mode, as seen from Figure 4.10(a). Clearly other mixed inter and intramolecular states contribute at longer times.

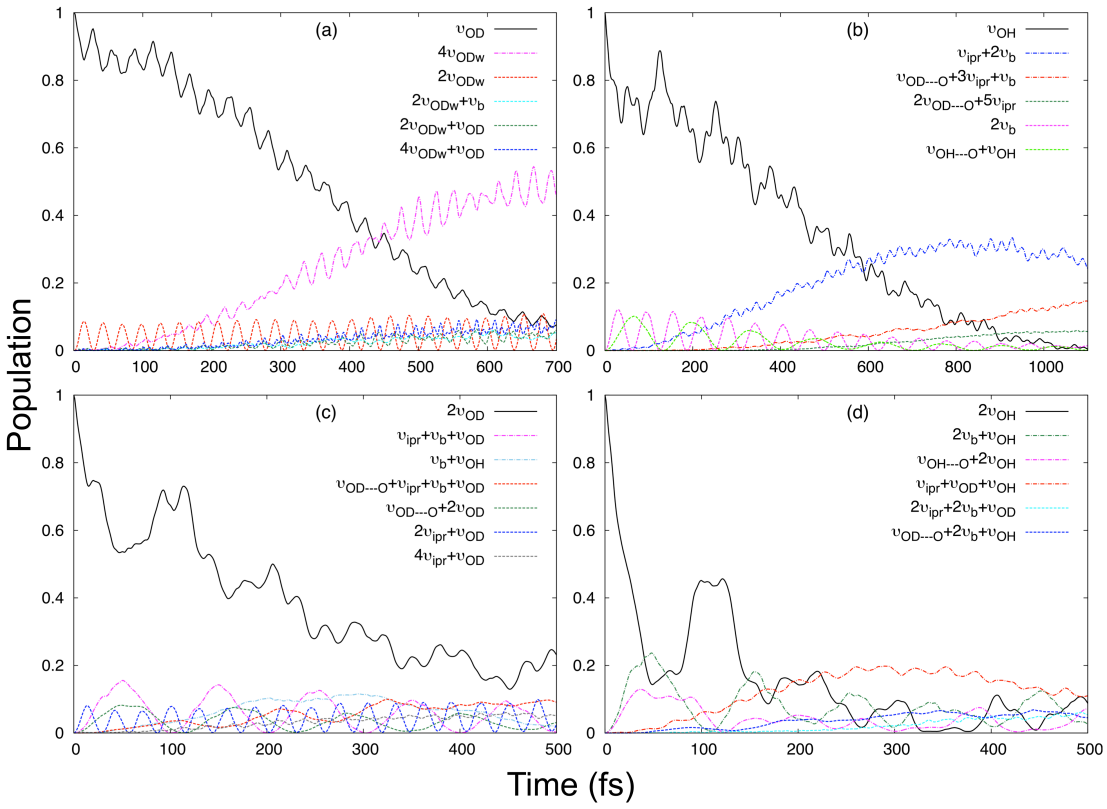

Figure 4.10. Time-dependent populations of the four excited non-stationary states and major population receivers. (a) OD fundamental (b) OH fundamental (c) OD overtone (d) OH overtone.

The relaxation pathways for the OD and OH overtones show distinctive features. As seen from Figure 4.10(d), the decay of the OH overtone is strongly correlated with the rise of $2v_b + v_{OH}$ and $v_{OH\cdots O} + 2v_{OH}$. This clearly indicates the mixing of the OH overtone with these two states. For the OD overtone, as shown in Figure 4.10(c), the relaxation is not due to a dominant pathway. This finding is clearly in opposition to the simple 2-mode analysis using the L-S potential, reported by Hamm et al.[76]

4.3.4. Summary

To conclude, both intra and intermolecular couplings in HOD are responsible for the vibrational relaxation dynamics of the OH and OD stretch excitations of HOD in ice Ih. The details of the relaxation pathways are, as expected, sensitive to whether the excitation is fundamental or overtone and also specific to OH and OD. Further, it is clear that such complex dynamical process cannot be described by coupling a single OD/OH stretch with a single intermolecular mode, which has been recently suggested in the literature.[75,76] The calculations again demonstrate the accuracy and extendibility of the WHBB water potential and the local monomer quantum dynamical model in the broad research field of the dynamics and spectroscopy of liquid water and ice. Future calculations will address spectral inhomogeneity by

considering additional sites for HOD. Recent 2D-IR spectra[75] and approximate calculations[84] indicate that this broadening is of the order of 25 cm^{-1}.

References

1. C. Haas and D. F. Hornig, J. Chem. Phys. **32**, 1763 (1960).
2. E. Whalley, Can. J, Chem. **55**, 3429 (1977).
3. G. Leto and G. A. Baratta, Astro. and Astrophys. **397**, 7 (2003).
4. E. H. Backus, M. L. Grecea, A. W. Kleyn and M. Bonn, Phys. Rev. Lett. **92**, 236101 (2004).
5. F. o. Cholette, T. Zubkov, R. S. Smith, Z. Dohnálek, B. D. Kay and P. Ayotte, J. Phys. Chem.B **113**, 4131 (2008).
6. J. P. Devlin, J. Geophys. Res. **106**, 33333 (2001).
7. R. McGraw, W. G. Madden, M. S. Bergren, S. A. Rice and M. G. Sceats, J. Chem. Phys. **69**, 3483 (1978).
8. M. S. Bergren, D. Schuh, M. G. Sceats and S. A. Rice, J. Chem. Phys. **69**, 3477 (1978).
9. M. S. Bergren, J. Chem. Phys. **77**, 583 (1982).
10. G. Nielson, J. Chem. Phys. **78**, 4824 (1983).
11. S. A. Rice, M. S. Bergren, A. C. Belch and G. Nielsen, J. Phys. Chem.**87**, 4295 (1983).
12. M. J. Wojcik, V. Buch and J. P. Devlin, J. Chem. Phys. **99**, 2332 (1993).
13. V. Buch and J. P. Devlin, J. Chem. Phys. **110**, 3437 (1999).
14. J. P. Devlin, C. Joyce and V. Buch, J. Phys. Chem. A **104**, 1974 (2000).

15. V. Buch *, B. Sigurd, J. Paul Devlin, U. Buck and J. K. Kazimirski, Int. Rev. Phys. Chem. **23**, 375 (2004).

16. M. J. Wójcik, K. Szczeponek and S. Ikeda, J. Chem. Phys. **117**, 9850 (2002).

17. F. Li and J. L. Skinner, J. Chem. Phys. **133**, 244504 (2010).

18. L. Shi, S. M. Gruenbaum and J. L. Skinner, J. Phys. Chem. B (2012).

19. T. Ishiyama, H. Takahashi and A. Morita, J. Phys. Chem. Lett., 3001 (2012).

20. C. C. Pradzynski, R. M. Forck, T. Zeuch, P. Slavíček and U. Buck, Science **337**, 1529 (2012).

21. P. Ayotte, G. H. Weddle, J. Kim and M. A. Johnson, J. Am. Chem. Soc.**120**, 12361 (1998).

22. W. H. Robertson, G. H. Weddle, J. A. Kelley and M. A. Johnson, J. Phys. Chem. A **106**, 1205 (2002).

23. J. D. Rodriguez, T. D. Vaden and J. M. Lisy, J. Am. Chem. Soc.**131**, 17277 (2009).

24. J. S. Prell and E. R. Williams, J. Am. Chem. Soc.**131**, 4110 (2009).

25. J. A. Hayward and J. R. Reimers, J. Chem. Phys. **106**, 1518 (1997).

26. L. Martínez; R. Andrade; E.G. Birgin; J.M. Martínez, J. Comput. Chem. **30**, 2157 (2009).

27. J.W. Ponder, TINKER: Software Tools for Molecular Design, version 5.0; Washington University School of Medicine: St. Louis, MO, 2009.

28. P. Ren and J. W. Ponder, J. Phys. Chem. B **107**, 5933 (2003).

29. J. Hernandez, N. Uras and J. P. Devlin, J. Chem. Phys. **108**, 4525 (1998).

30. J. P. Devlin and V. Buch, J. Phys. Chem.**99**, 16534 (1995).

31. J. P. Devlin and V. Buch, J. Phys. Chem. B **101**, 6095 (1997).

32. C. Steinbach, P. Andersson, J. K. Kazimirski, U. Buck, V. Buch and T. A. Beu, J. Phys. Chem. A **108**, 6165 (2004).

33. V. Buch, T. Tarbuck, G. L. Richmond, H. Groenzin, I. Li and M. J. Shultz, J. Chem. Phys. **127**, 204710 (2007).

34. H. Groenzin, I. Li and M. J. Shultz, J. Chem. Phys. **128**, 214510 (2008).

35. J. E. Bertie, J. Chem. Phys. **46**, 1271 (1967).

36. J. E. Bertie, J. Chem. Phys. **50**, 4501 (1969).

37. K. Abe and T. Shigenari, J. Chem. Phys. **134**, 104506 (2011).

38. H. J. Prask, J. Chem. Phys. **56**, 3217 (1972).

39. B. Renker, In Lattice Dynamics of Hexagonal Ice; Symposium on the Physics and Chemistry of Ice, Ottawa, Canada, Aug 14–18, 1972; Whalley, E., Jones, S. J., Gold, L. W., Eds.; Royal Society of Canada: Ottawa, 1973, pp 82–86.

40. D. Klug, E. Whalley, E. Svensson, J. Root and V. Sears, Phys. Rev. B **44**, 841 (1991).

41. J. Li and D. K. Ross, Nature **365**, 327 (1993).

42. J. Li, J. Chem. Phys. **105**, 6733 (1996).

43. A. I. Kolesnikov, V. V. Sinitsyn, E. G. Ponyatovsky, I. Natkaniec and L. S. Smirnov, J. Phys.: Cond. Matt. **6**, 375 (1994).

44. J. C. Li, C. Burnham, A. I. Kolesnikov and R. S. Eccleston, Phys. Rev. B **59**, 9088 (1999).

45. H. Fukazawa, S. Ikeda, M. Oguro, S. M. Bennington and S. Mae, J. Chem. Phys. **118**, 1577 (2003).

46. S. Klotz, T. Strässle, C. G. Salzmann, J. Philippe and S. F. Parker, Europhysics Letters (EPL) **72**, 576 (2005).

47. M. Koza, H. Schober, S. Parker and J. Peters, Phys. Rev. B **77** (2008).

48. G. Nielson, R. M. Townsend and S. A. Rice, J. Chem. Phys. **81**, 5288 (1984).

49. J. S. Tse, M. L. Klein and I. R. McDonald, J. Chem. Phys. **81**, 6124 (1984).

50. I. Morrison and S. Jenkins, Physica B: Condensed Matter **263–264**, 442 (1999).

51. S. Dong, Y. Wang and J. Li, Chemical Physics **270**, 309 (2001).

52. A. S. Cote, I. Morrison, X. Cui, S. Jenkins and D. K. Ross, Can. J. Phys. Chem. **81**, 115 (2003).

53. W. A. Adeagbo, A. Zayak and P. Entel, Phase Transitions **78**, 179 (2005).

54. P. Zhang, L. Tian, Z. P. Zhang, G. Shao and J. C. Li, J. Chem. Phys. **137**, 044504 (2012).

55. X. He, O. Sode, S. S. Xantheas and S. Hirata, J. Chem. Phys. **137**, 204505 (2012).

56. S. Hirata, J. Chem. Phys. **129**, 204104 (2008).

57. O. Sode and S. Hirata, Phys. Chem. Chem. Phys. **14**, 7765 (2012).

58. H. Liu, Y. Wang and J. M. Bowman, J. Phys. Chem. Lett. **3**, 3671 (2012).

59. Y. Wang, X. Huang, B. C. Shepler, B. J. Braams and J. M. Bowman, J. Chem. Phys. **134**, 094509 (2011).

60. M. A. Floriano, D. D. Klug, E. Whalley, E. C. Svensson, V. F. Sears and E. D. Hallman, Nature **329**, 821 (1987).

61. A.G. Csaśzaŕ; G. Czako;T. Furtenbacher;J. Tennyson; V. Szalay; S.V. Shirin; N.F. Zobov; O.L. Polyansky. **122**, 214305 (2005).

62. M. W. Severson, J. P. Devlin and V. Buch, J. Chem. Phys. **119**, 4449 (2003).

63. S. Imoto, S. S. Xantheas and S. Saito, J. Chem. Phys. **138**, 054506 (2013).

64. K. L. Vodopyanov, J. Chem. Phys. **94**, 5389 (1991).

65. C. J. Fecko, J. D. Eaves, J. J. Loparo, A. Tokmakoff and P. L. Geissler, Science **301**, 1698 (2003).

66. M. L. Cowan, B. D. Bruner, N. Huse, J. R. Dwyer, B. Chugh, E. T. J. Nibbering, T. Elsaesser and R. J. D. Miller, Nature **434**, 199 (2005).

67. E. T. J. Nibbering and T. Elsaesser, Chem. Rev. **104**, 1887 (2004).

68. S. Woutersen, U. Emmerichs, H.-K. Nienhuys and H. J. Bakker, Phys. Rev. Letters **81**, 1106 (1998).

69. G. M. Gale, G. Gallot and N. Lascoux, Chem. Phys. Lett. **311**, 123 (1999).

70. J. C. Deàk, S. T. Rhea, L. K. Iwaki and D. D. Dlott, J. Phys. Chem. A **104**, 4866 (2000).

71. D. Schwarzer, J. Lindner and P. Vohringer, J. Chem. Phys. **123**, 161105 (2005).

72. G. Seifert, K. Weidlich and H. Graener, Phys. Rev. B **56**, R14231 (1997).

73. A. M. Dokter and H. J. Bakker, J. Chem. Phys. **128**, 024502 (2008).

74. W. J. Smit and H. J. Bakker, J. Chem. Phys. **139** (2013).

75. F. Perakis, S. Widmer and P. Hamm, J. Chem. Phys. **134**, 204505 (2011).

76. F. Perakis, J. A. Borek and P. Hamm, J. Chem. Phys. **139**, 014501 (2013).

77. R. Rey and J. T. Hynes, J. Chem. Phys. **104**, 2356 (1996).

78. R. Rey, K. B. Møller and J. T. Hynes, Chemical Reviews **104**, 1915 (2004).

79. C. P. Lawrence and J. L. Skinner, J. Chem. Phys. **117**, 5827 (2002); **119**, 1623 (2003); **119**, 3840 (2003).

80. J. A. Poulsen, G. Nyman and S. Nordholm, J. Phys. Chem.A **107**, 8420 (2003).

81. C. Bäcktorp, J. A. Poulsen and G. Nyman, J. Phys. Chem.A **109**, 3105 (2005).

82. E. R. Lippincott and R. Schroeder, J. Chem. Phys. **23**, 1099 (1955).

83. H. Partridge and D. W. Schwenke, J. Chem. Phys. **106**, 4618 (1997).

84. L. Shi and J. L. Skinner, J. Phys. Chem. B **117**, 15536 (2013).

Chapter 5.

The Infrared Spectra of Liquid Water

5.1. Overview

The IR spectrum of water at 298 K has been known since at least 1997.[1-4] And at the risk of oversimplifying (especially given the results herein), it is typically divided into two regions, the intramolecular one and the intermolecular one. The former is above roughly 1600 cm^{-1}, where two broad features are assigned as the monomer bend (at around 1600 cm^{-1}) and the H-bonded OH-stretches (very broad feature at around 3400 cm^{-1}). This region is aptly named because the isolated water molecule has a bend fundamental at 1595 cm^{-1} and two stretch fundamentals at 3657 and 3756 cm^{-1}. The large down-shift of the experimental "OH-stretch" band in the liquid, relative to the gas-phase, is securely known to be due to the strong hydrogen bonds, which in the core region of the liquid every OH-stretch in H_2O experiences. Of these spectral regions, the OH-stretch region has received the greatest attention by theorists and experimentalists because of this strong down-shift and also because the band is so broad. A feature of these bend and stretch bands relative to the gas phase that has not received as much attention is the

marked differences in intensity. In the gas-phase the bend fundamental is roughly 25% more intense than the sum of the intensities of the (weak) symmetric and anti-symmetric OH-stretch fundamentals. By contrast, in liquid water the peak in the OH-stretch band is roughly five times as intense as the bend peak.[1-4] Clearly there is some important information in this observation that tells us that the dipole moment (more specifically its variation in the bend and stretch coordinates) in the liquid is substantially different than in the gas phase. Manolopoulos and co-workers[5] noticed this, albeit indirectly, in a comparison of the calculated IR spectrum of water using ring polymer molecular dynamics (RPMD) using a modified, flexible version of the very popular TIP4P and SPC fixed-charged potentials. They wrote "The relative intensities of the intramolecular bending and stretching bands also disagree with experiment in both simulations, and this again arises from the neglect of electronic polarization." The suggestion here as well as widespread in the literature that polarization of the monomers is what is "missing" in fixed point-charge models.

As reviewed in Chapter 2 and Chapter 3, the theoretical studies have largely relied on the fixed point-charge and empirical polarizable models; the q-SPC/Fw, q-TIP4P/F and TTM3-F PESs and their associated dipole moment surfaces have been used in several semi-quantum and semi-classical calculations of the IR spectrum of water.[6-17] Specifically, the linearized semi-classical Initial Value

Representation (LSC-IVR) method,[6,7] Centroid molecular dynamics (CMD),[8,9] and (thermostatted) ring-polymer molecular dynamics(TRPMD)[5,10,11] have been all applied to calculate the IR spectrum of liquid water. These have all employed the semi-empirical TTM3-F model and either or both q-SPC/Fw and q-TIP4P/F models. The results of those calculations will be briefly discussed later in this Chapter. Classical[12] and mixed quantum and classical[13-17] calculations of the OH stretch band have also been reported. Each method has advantages and drawbacks and we refer the reader to the literature for the discussion of these.[6,7,11,18,19] The Local Monomer approach that we have developed[19] was applied recently in a joint study[20] that compared the performance of the CMD and RPMD and LMon methods in calculating the IR spectra of ice at 150 K, liquid water at 300 K, and liquid-vapor interface at 600 K. These calculations were done using the q-TIP4P/F potential and DMS, in part because this model had been used previously in CMD and RPMD[11] and also because it is computationally fast to evaluate. The study shows pure classical MD (which was also done) is unreliable even up to 600 K because it gives a significant blue-shifted spectrum as a result of missing the important anharmonicity. The CMD, TRPMD and LMon methods give consistent spectra at least for the liquid water at 298 K, although some significant inconsistencies were seen for ice Ih at 150 K.

In this Chapter, the IR spectrum of liquid water using the WHBB PES and the

new DMS is presented and compared with the experiment and the q-TIP4P/F and TTM3-F spectra. We will also provide a deconstruction of the spectrum and give assignments to each spectral band. Finally, concluding remarks will be made at the end of the Chapter.

5.2. Computational Details

The LMon-4 method is used to obtain the IR spectrum. Details description of this method is given in Chapter 3. The Details of the classical MD sampling is given below. In the present calculations, we use snapshots from an extensive, long-time classical NVT molecular dynamics simulation at 300 K done by Skinner and co-workers.[22] Details of this simulations are the following. Five hundred H_2O monomers were contained in a cubic box of sides 24.6671 Angstrom, allowing the experimental density to be reproduced. Usual periodic boundary conditions were applied. The monomers are kept rigid, and the intermolecular interactions were described by the E3B potential,[22] which contains an empirical 2-body potential based on TIP4P and a rigid 3-body potential. The trajectory was propagated for 300 ps using the velocity Verlet algorithm with a stepsize of 1 fs. The simulation was performed using the GROMACS 4.5.5 software. For each snapshot, 100 monomer configurations in the central region of the box, out of the 500 total monomer configurations, were selected for LMon calculations. A total of ten snapshots were

used, separated by an interval of 30 ps.

Finally, calculations using q-TIP4P/F and TTM3-F potentials follow the above procedures with WHBB and the new dipole moment surface replaced by the potential and dipole moment surfaces contained in those models.

5.3. Results and Discussion

One measure to assess the applicability of the LMon approach to the water spectrum, is to compare the harmonic vibrational density of states (VDOS) from the local normal mode analysis with a full normal mode analysis. This was done on the core 100 monomers that are embedded in the box of 500 liquid water monomers for each of ten equally-spaced MD snapshots. Thus, there are a total of 900 harmonic frequencies for each snapshot. To obtain a smoothed VDOSs from these, we first represent each mode by a stick with a height of 1 and then multiply it by a Gaussian function with FWHM=70 cm^{-1}. Therefore, the unit of the VDOS is number of states per cm^{-1}. Results for the 10 snapshots mentioned are summed in the two VDOSs. Comparing the two in Figure 5.1, we see good agreement in the region of the OH stretch and the bend, i.e., above 1500 cm^{-1}. The doublet band in the OH-stretch region is familiar from numerous other simulations. The higher frequency band has significantly greater IR intensity and so the very good agreement between the two VDOSs for that band is perhaps re-assuring. For the low-frequency,

intermolecular region (below 1500 cm^{-1}), the two sets of results are in good agreement with each other, but there are some differences. The lormal VDOS shows a narrower peak at ~175 cm^{-1} and also shows more density in the region of 350-650 cm^{-1}.

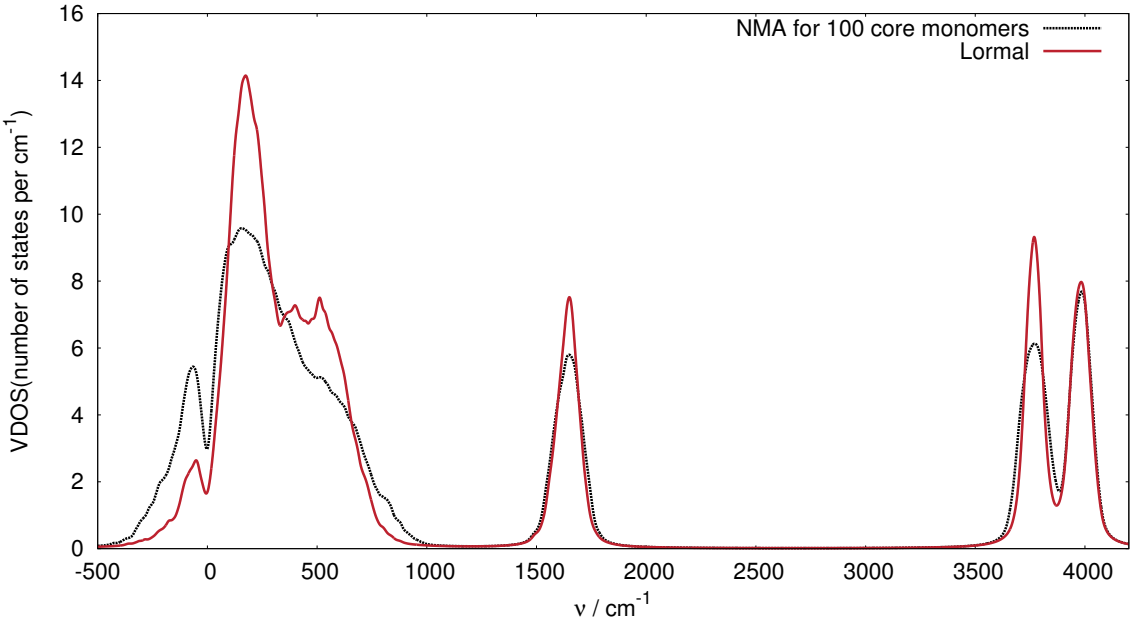

Figure 5.1. Harmonic vibrational density of states from normal mode analysis of the core 100-mer, and from local normal mode analysis of the 100 monomers. States are summed from 10 snapshots, as described in the text. For graphical purposes, imaginary frequencies are shown as negative numbers.

The nine lormal modes of a typical monomer in the core sample set are shown in Figure 5.2. The three in the bottom panel are clearly identified as the monomer bend, symmetric stretch and asymmetric stretch. The other modes are "frustrated"

translational and rotational modes. The latter ones are higher frequency ones and these are more commonly referred to as the librational modes.

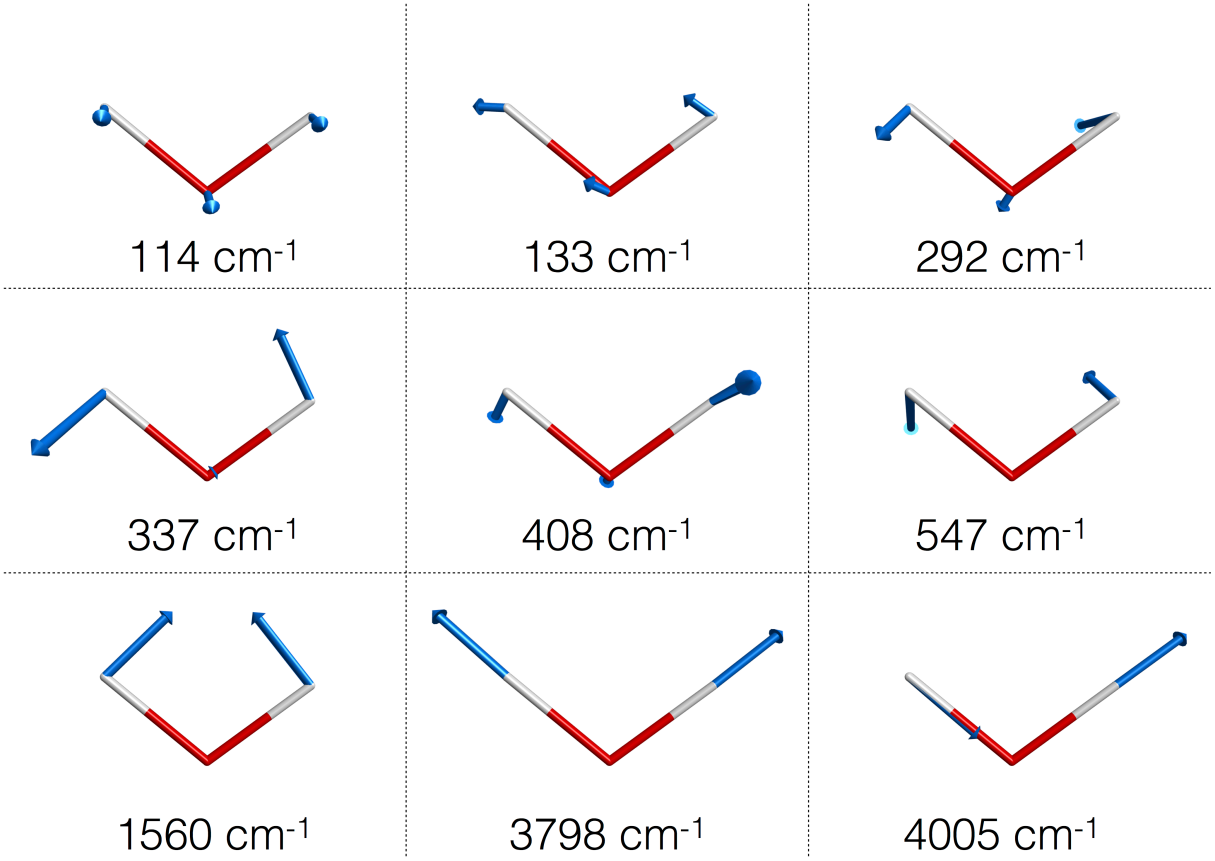

Figure 5.2. Depiction of the 9 lormal modes and frequencies of an example monomer.

Finally, it should be noted that both sets of VDOSs contain some imaginary frequencies, as expected, since the configurations sampled are not strict local minima of course. These are indicated in Figure 5.1 by the negative frequencies instead of the correct imaginary ones. For the full normal mode VDOS, 10.4%

frequencies are imaginary, while for the lormal VDOS, the percentage is 3.6%. The imaginary-frequency lormal modes are frustrated translational or rotational modes and of course the motions of these modes are hindered in the liquid environment. So, these modes are included in the LMon-4 calculations and real-valued eigenvalues are obtained for them. The details of treating imaginary-frequency modes in MULTIMODE are given elsewhere.[24] It is perhaps worth noting that a full normal mode VDOS using PIMD simulations with the TTM3-F potential, reported 14% imaginary frequencies.[7]

Using the sample set described above, we calculated LMon-4 spectra for three potentials and corresponding dipole moments surfaces, WHBB and DMS(1b-LTP, 2b-MP2), q-TIP4P/F and TTM3-F. For each set of MULTIMODE calculations the first 50 eigenvalues and eigenvectors of the VCI matrix were obtain and by default all dipole transition matrix elements were calculated numerically. This amounted to roughly 7,000,000 dipole transition vector matrix elements for the 100 monomers and 10 snaphots. Of these, roughly 6,000,000 were used in the thermally averaged spectrum at 300 K. For the IR spectrum from the ground vibrational state of total of roughly 100,000 dipole matrix elements were calculated.

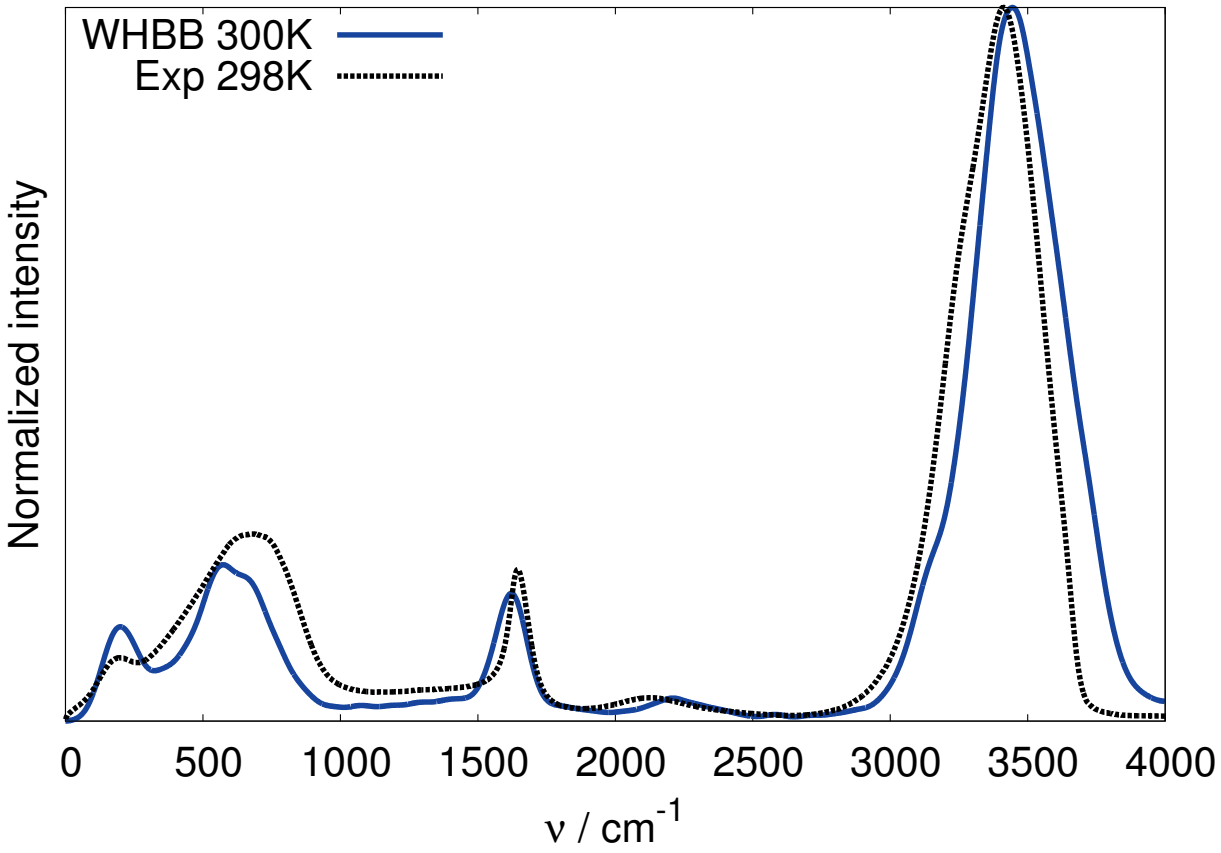

Figure 5.3. Thermally averaged LMon-4 IR spectra of liquid water at 300K using WHBB potential and the new DMS. The experimental spectrum is from ref 1.

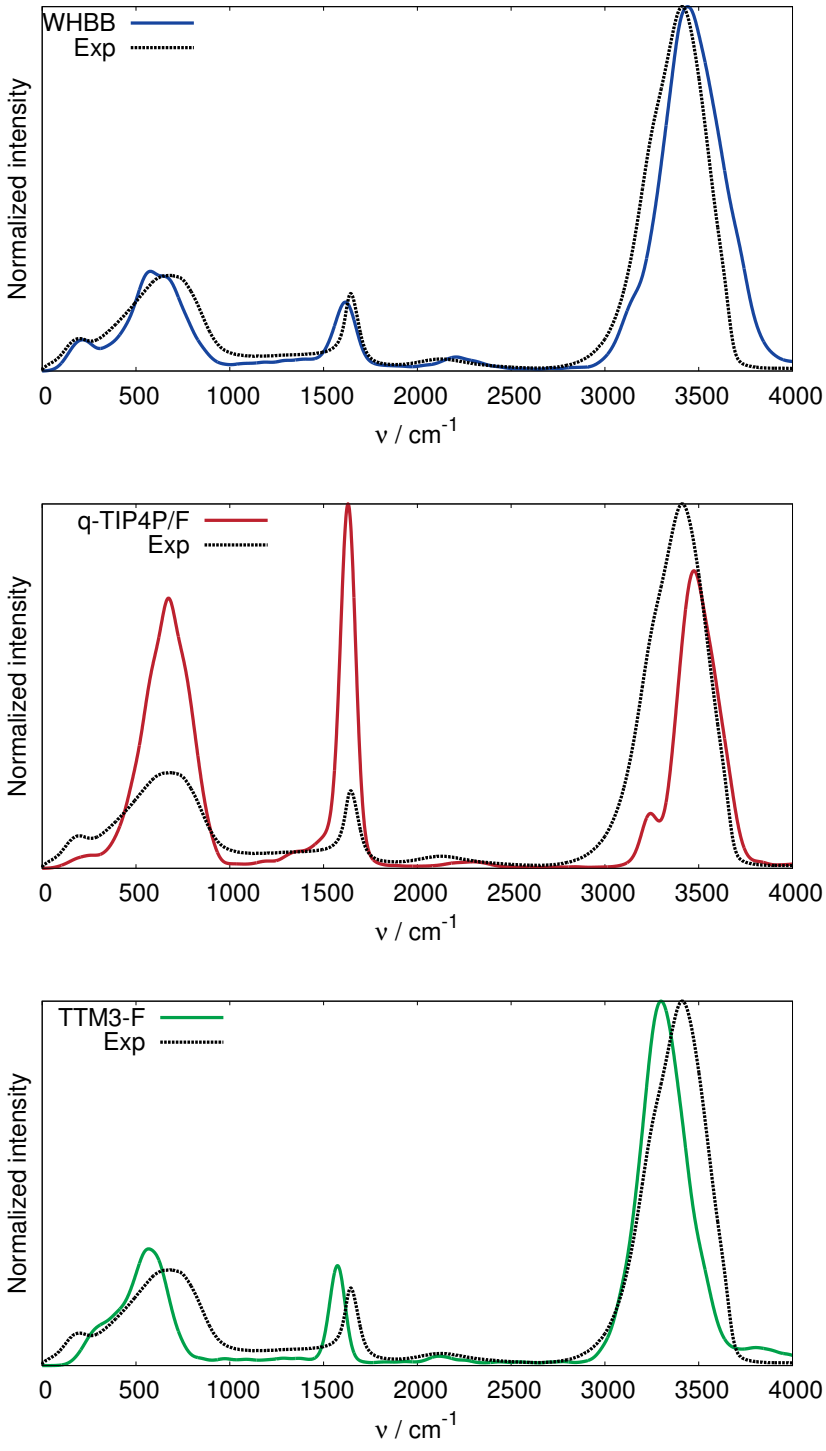

Figure 5.4. LMon-4 spectra containing transitions only from the ground state using WHBB (with the new DMS), q-TIP4P/F and TTM3-F PESs and DMSs. The

experimental spectrum is from ref 1.

The thermally averaged spectrum from WHBB (with the new DMS), is compared to experiment[1] in Figure 5.3. Theoretical and experimental spectra are normalized to the band with the highest intensity. A cursory scan of results shows very good agreement with experiment. The LMon-4 spectrum features three major bands: the so-called "intermolecular band" in the range 0-1000 cm^{-1} and the well-known bands of the bend at around 1500-1700 cm^{-1} and the OH-stretch at around 3000-3800 cm^{-1}. We will present detailed analysis of the origins of these bands below. We focus here the excellent agreement between the theory and the experiment for both peak frequencies and intensity. The predicted peak positions of the two most well known bands, the bend and the OH-stretch, are within roughly 30 cm^{-1} of the experimental ones. The bend band peaks at 1645 cm^{-1} from the experiment and 1617 from theory. The OH-stretch peaks are at 3413 cm^{-1} from the experiment and 3441 cm^{-1} from theory. Besides the well-known bend and stretch bands, we also note the WHBB spectrum is able to well reproduce the experimental features of the broad band at 0-1000 cm^{-1}, notably the small peak at around 260 cm^{-1} and the major one at around 600 cm^{-1}. In addition the well-known, broad combination band in the range 2000-2400 cm^{-1} is accurately captured by the WHBB spectrum. We will return to these two bands and give the molecular

"deconstructions" for each band below. The agreement on intensity is also very good, especially for the ratio between the bend and the stretch. We will provide detailed discussion of the intensities also below.

Next, we compare LMon-4 IR spectra using q-TIP4P/F and TTM3-F PESs and DMSs with experiment and WHBB. For these comparisons, we consider transitions only from the ground vibrational state. This is done for a couple of reasons. One is that this provides the "cleanest" comparison of the theoretical spectra. Second, we note that WHBB spectrum in Figure 5.4a is very similar to the thermal spectrum in Figure 5.3. This is not surprising because at 298 K the thermal populations of hot bands is much less for the intramolecular modes, than the ground vibrational state population. Second, transitions from the first excited vibrational states have similar magnitudes in both the energies and transition dipole matrix moments, as those from the ground state. So, it is reasonable to also include the experimental spectra in each panel of this figure.

The LMon-4 spectrum using the q-TIP4P/F model is shown in Figure 5.4b from the same LMon-4 method and sampled from the same set of configurations. The main discrepancy to the experiment (and WHBB) is clearly the incorrect relative intensity for the bend, the stretch and the intermolecular bands. The intensity will be discussed extensively later. There are some other disagreements with the experiment as well. The two small maxima at 0-300 cm^{-1} and 2000-2400 cm^{-1} are

present, but not as intense as the ones in experiment or in the WHBB spectrum. The OH-stretch peak is blue-shifted from the experiment by ~60 cm^{-1}. Note the spectrum shown here has two differences from the previous one from the joint work reported recently.[20] This work considers all the six intermolecular modes while the previous joint work has only three highest frequencies intermolecular modes. Therefore, it is reasonable to see the spectrum in this work shows slightly more intense intermolecular band, especially for the region around 250 cm^{-1} which is due to the three lowest frequencies intermolecular modes. Also we notice the peak position of the bend in this work is roughly 20 cm^{-1} higher than the previous work, and the OH stretch peak is roughly 45 cm^{-1} lower. Another, possibly significant difference with that previous work is the sampling of the classical MD configurations. Here the monomers are rigid and the potential is TIP4P plus E3B rigid monomer, whereas the previous work uses PIMD configurations obtained with q-TIP4P/F. To test whether the frequency shift is due to the sampling or the LMon-4 subspace, we examined the rigid monomer MD sampled q-TIP4P/F spectrum using the transition dipole matrix elements only from the 3 sets of LMon-4 of highest frequencies intermolecular modes and saw basically identical peak positions to our current spectrum using all 6 sets of LMon-4. This confirms that the sensitivity of peak position is primarily due to the different sampling in this work and in the previous joint work. More discussion on the sampling is given in the

Supplementary Materials of Ref. 20.

The LMon-4 spectrum using the TTM3-F model is shown in figure 5.4c. The TTM3-F spectrum features good agreement with the experimental intensities, but the peak positions of the three major bands all show systematic red-shifts relative to experiment. The red-shifts for the OH-stretch, the bend and the intermolecular bands are roughly 115, 70, and 100 cm^{-1}, respectively. As already been pointed out in the literature,[7] such systematic red-shift is due to the fact that TTM3-F is parametrized to the experimental IR from classical MD simulations; if using classical MD to get IR, the red-shifts are only 25 cm^{-1} for the bend and 23 cm^{-1} for the OH.[7] It is a well-known issue that classical MD produce blue-shifted frequencies, relative to accurate quantum calculations because without zero-point energy in the simulation, the classical dynamics configurations mainly sample the harmonic region of the potential. It is worth noting that the present red-shifts relative to experiment are largely consistent with those reported in CMD,[8] RPMD,[10] and LSC-IVR[7] calculations. Specifically, the red-shift of the bend is 100, 76, and 35 cm^{-1} in CMD, RPMD, and LSC-IVR calculations, respectively, and for OH stretch the red-shift is 103, 172, and 128 cm^{-1}, respectively. The combination band at roughly 2200 cm^{-1} is clearly present in the LMon-4 spectrum. This feature is also present in the LSC-IVR calculations, but not clearly present in the classical MD and CMD calculations.[7] Also seen in the TTM3-F spectrum is that each of the three main peak is narrower than

the correspondent experimental peak.

It is gratifying to see the *ab initio* DMS reproduces the experimental intensity of each spectral band with good accuracy, especially the correct relative intensity of the bend over the OH stretch. We can conclude that the intrinsic 2-body dipole is needed to calculate the IR spectrum of liquid water. In Chapter 2, we have already shown that the 2-body dipole causes the dramatic increase of the OH stretch intensity in the water dimer and the prism hexamer over the isolated water monomer. Here in the scenario of liquid water spectrum, one sees with the 2-body DMS included, the intensity of the OH stretch is about 5 times higher than the bend, correctly reproducing the experiment. In contrast, the spectrum using the q-TIP4P/F model and the same LMon method (shown in Figure 5.4b) fails to get this intensity ratio. (Previous work using q-TIP4P/F and other dynamics methods have shown similar intensity.[5,11,20]) The reason is that without an explicit 2-body dipole interaction, the effects of electron polarization and partial charge transfer are neglected in any of the fixed point-charge models. It is interesting to note that the ratio of the bend to OH-stretch peak intensity is close to what is found for the water monomer, cf. Table 2.1. This is not surprising of course for a fixed (monomer) charge model.

As noted in the Introduction, the TTM3-F DMS is based on a simple charge-transfer model of a monomer as the OH bond is stretched, and takes an

empirical approach to incorporate this effect by modifying the gas-phase monomer dipole moment. Since the parameters are determined to reproduce the experimental IR intensity, albeit with classical MD simulation, it is not surprising to see good intensity agreement with LMon method.

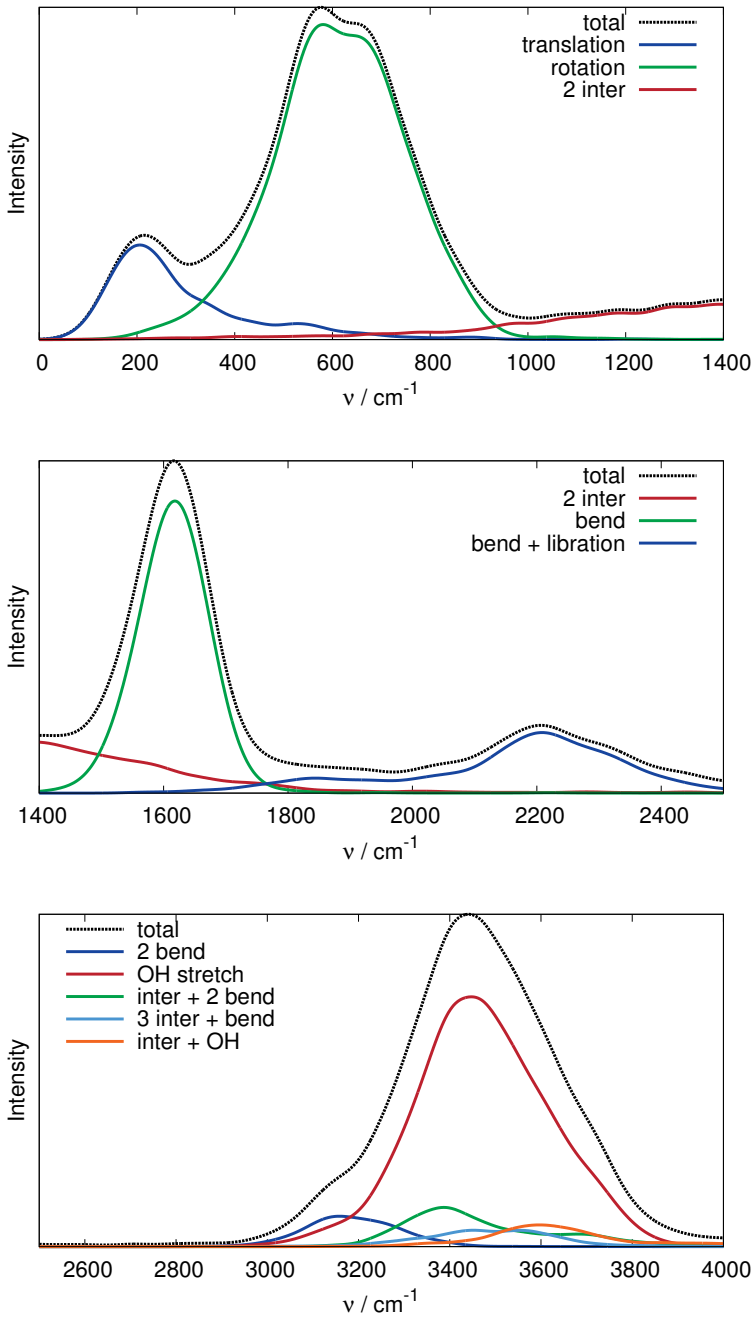

Figure 5.5. Deconstruction of spectral bands, see text for more details.

Next, we deconstruct the WHHB spectrum and give the molecular origin of each spectral band. This is done for the spectrum shown in Figure 5.4a, i.e., for

transitions out of the ground vibrational state of all modes. The assignment is made by analyzing the VCI states within each band, and the results are shown in three frequency ranges in Figure 5.5. The dominant VSCF/virtual state of a VCI eigenstate is used for the assignment. Starting from the far infrared end, the broad band from 0-1000 cm^{-1} is due to the fundamentals of intermolecular monomer modes. These modes are the first six ones illustrated in Figure 5.2. The small maximum seen in the region of 0-300 cm^{-1} is due to the three lowest frequency intermolecular modes, which are hindered translational modes for most monomers. The band in the region of 400-1000 cm^{-1} is due to the three highest frequency intermolecular modes, which are hindered rotational modes for most monomers. It is also of interest to note that the structure of this IR band is, not surprisingly, reflected approximately in the harmonic vibrational density of states, shown in Figure 5.1. This similarity confirms that this band is essentially due to fundamental excitations.

The flat and less intense intermediate band from 1000-1500 cm^{-1} is mainly due to the overtone of intermolecular modes. This is consistent with the absence of harmonic VDOS in this spectral region. Also, it is important to note the combination excitations involving the intermolecular modes are not accounted for in the present calculations and so contributions from these excitations are not present in the LMon-4 spectra. The band from 1500-1700 cm^{-1} is due

predominantly monomer fundamental bend excitation. The well-known, spectral feature and broad maxium in the range 2000-2400 cm^{-1} is mostly due to the combination band of the bend and an intermolecular mode, mainly a hindered rotational mode. Note again the absence of harmonic VDOS in this spectral range. This analysis supports the assignment of this band given in experiments.[2] The broad band between 3000 and 4000 cm^{-1} is, as expected, dominated by the OH stretch, as numerous previously studies have suggested and focused on.[13-17] However, we found there are other contributions to this band. These include the bend overtone, which we had previously reported in the OH stretch band in ice Ih and several isomers of water hexamer, the bend overtone plus intermolecular modes, and OH stretch plus intermolecular modes. Note these VCI states, although marked by their largest coefficient, are strongly mixed with major contribution from the OH stretch VSCF state. The noticeable intensity of these VCI states also largely come from the OH stretch VSCF/virtual state.

Overall, we believe the present results and comparison with experiment represent a significant step forward in the fully *ab initio* approach to a quantitative and robust ("the right answers for the right reasons") description and calculation of IR spectrum of liquid water at 298 K, where experiments have been done. We have shown the central role of an accurate *ab initio* dipole moment surface, which we feel has not been sufficiently emphasized previously. The present study of this dipole

moment points out serious limitations of fixed-charge models. It is beyond the scope of this Section to probe deeply into whether such a model with monomer polarizability can correctly capture the correct physics of even the 2-body dipole, but there is mounting evidence that it cannot. This comes even from the pioneering work of Xantheas and co-workers (TTM3-F), who, despite incorporating a sophisticated polarizable model for water, had to significantly modify the monomer dipole moment surface, to achieve agreement with experimental intensities for the water IR spectrum. Certainly, the virtually established role that some charge-transfer occurs in the water dimer, adds to the conclusion that long-range "induction" is not sufficient to describe the water dipole moment.

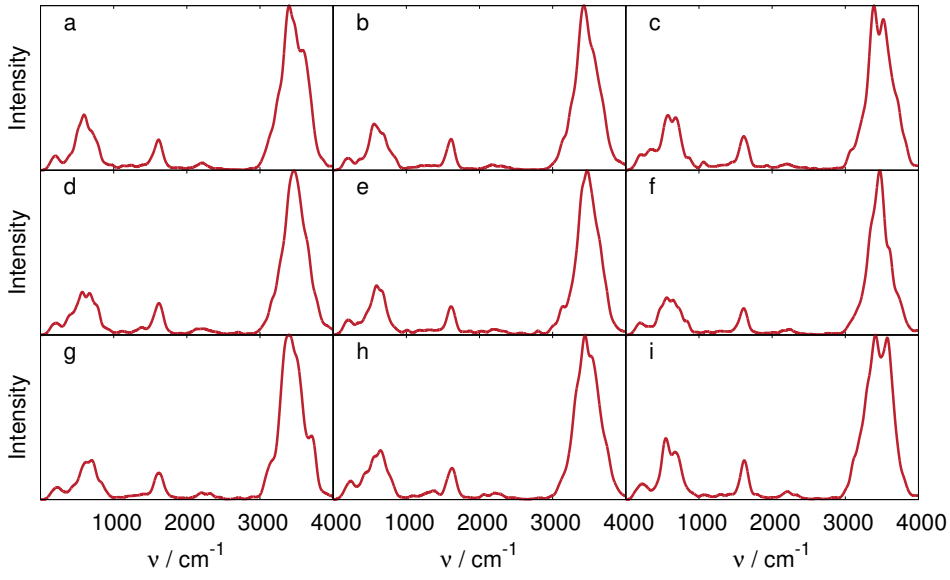

Figure 5.6. IR spectra of 9 snapshots. The interval is 30 ps. Each spectrum is obtained in the same way as the one in Figure 5.4a with a FWHM of 70 cm^{-1}.

Some remarks about the LMon-4 approach taken here are in order. First, it is an approximate quantum treatment in several respects. It incorporates the six intermolecular modes of each monomer, but one-by-one. This is done largely for computational efficiency and indeed the cost of LMon-4 is modest. With WHBB PES and the new DMS, each LMon-4 calculation takes roughly 20 minutes using a single core on a single node of a multi-node workstation. The time is 4 min with q-TIP4P/F PES and DMS, and 20 min with TTM3-F PES and DMS. Since all the tasks are independent, the computations were distributed to multiple cores on several nodes of our in-house cluster. So the typical wall-clock time for the present calculations is roughly 1 day using 60 cores and could be much shorter if using more cores. Of course, the scaling of the LMon approach with the number of coupled modes is steep, and full 9-mode coupled calculations for each monomer would certainly require at least ten times more cpu time. Another approximation of the approach taken here is the absence of explicit time dependence. The spectrum is obtained from samples of an MD trajectory and so no time-coherence is described by this approximation. One understands for say elementary isomerization dynamics that coherent beating between say two isomeric minima can introduce coherences in the IR spectrum, e.g., fine structure such as line splitting or additional spectral lines. It is beyond the scope of this Section to explore the possible issues

and errors associated with this. However, it is of interest to examine the present LMon-4 IR spectra for a series of MD "snapshots". This is done in Figure 5.6 for the WHBB PES and present DMS for transitions out of the ground vibrational state. As seen the IR spectra are quite similar, although each is "noisier" than the spectrum shown in Figure 5.4a. To us this suggests that the IR spectral bands are dominantly inhomogeneously broadened at 298 K. The good agreement with experiment seen in Figure 5.3 certainly supports this conclusion. However, there has been much discussion in the literature about the spectral lines shapes of water and it is beyond the scope of this Section to delve deeply into that issue. The interested reader could consult the discussion of line shapes in recent joint work comparing the IR spectra of ice and liquid water in reference 38 using four different approaches.

The favorable aspects of the LMon approach in addition to its efficiency are that it is fully quantum and so the description of zero-point energy, fundamentals, combination and overtone bands is straightforwardly obtained. In addition, no approximations are needed on the form the dipole moment, e.g., that it a linear operator. Another advantage of the local approach is that it can be readily extended to mixed clusters and also the direct ("on-the-fly") calculation of the electronic energy of a monomer embedded in a homogenous or inhomogeneous environment of other monomers can be done fairly efficiently. This was done

recently for mixed HCl/H_2O clusters,[24-26] and for the spectral signature of hydronium in the separated ion pair of the $H_3O^+Cl^-(H2O)_3$ cluster.[27]

5.4. Summary

To summarize, the IR spectrum of liquid water at 300 K was calculated using the *ab initio* WHBB PES, the new DMS, and quantum LMon-4 method; very good agreement was found for both band positions and intensities, including the well-known combination band between the intramolecular bending and OH-stretch bands. With the same LMon-4 method, the spectrum using q-TIP4P/F model predicts qualitatively wrong intensity for the spectrum because of its linear dipole as mentioned above. The spectrum using TTM3-F model shows systematic red-shifts, because the model is based on classical simulation which misses the important quantum effects. Intensities are much better; however, these were adjusted by using a model dipole moment for the monomer to give good agreement with experiment, based on a standard classical MD treatment of the IR spectrum.

Deconstruction of the spectrum shows that the simple-looking IR spectrum of liquid water has its complicated molecular origins. Specifically, many combination and overtone bands contribute the overall spectrum, especially in the OH-stretch region. This also demonstrates the strength of the LMon-4 approach in studying the condensed-phase vibrational spectra, because it is capable in describing these

bands.

References

1. J. E. Bertie and Z. Lan, Appl. Spectrosc. **50**, 1047 (1996).
2. S. Y. Venyaminov and F. G. Prendergast, Anal. Biochem. **248**, 234 (1997).
3. J. B. Brubach, A. Mermet, A. Filabozzi, A. Gerschel and P. Roy, J. Chem. Phys. **122**, 184509 (2005).
4. J. J. Max and C. Chapados, J. Chem. Phys. **131**, 184505 (2009).
5. S. Habershon, T. E. Markland and D. E. Manolopoulos, J. Chem. Phys. **131**, 024501 (2009).
6. J. Liu, W. H. Miller, F. Paesani, W. Zhang and D. A. Case, J. Chem. Phys. **131**, 164509 (2009).
7. J. Liu, W. H. Miller, G. S. Fanourgakis, S. S. Xantheas, S. Imoto and S. Saito, J. Chem. Phys. **135**, 244503 (2011).
8. F. Paesani, S. S. Xantheas and G. A. Voth, J. Phys. Chem. B **113**, 13118 (2009).
9. F. Paesani and G. A. Voth, J. Chem. Phys. **132**, 014105 (2010).
10. S. Habershon, G. S. Fanourgakis and D. E. Manolopoulos, J. Chem. Phys. **129**, 074501 (2008).
11. M. Rossi, M. Ceriotti and D. E. Manolopoulos, J. Chem. Phys. **140**, 234116 (2014).
12. H. Ahlborn, X. Ji, B. Space and P. B. Moore, J. Chem. Phys. **111**, 10622 (1999).
13. S. A. Rice, M. S. Bergren, A. C. Belch and G. Nielsen, J. Phys. Chem. **87**, 4295 (1983).

14. V. Buch, J. Phys. Chem. B **109**, 17771 (2005).

15. H. Torii, J. Phys. Chem. A **110**, 9469 (2006).

16. B. M. Auer and J. L. Skinner, J. Chem. Phys. **128**, 224511 (2008).

17. J.-H. Choi and M. Cho, J. Chem. Phys. **138**, 174108 (2013).

18. A. Witt, S. D. Ivanov, M. Shiga, H. Forbert and D. Marx, J. Chem. Phys. **130**, 194510 (2009).

19. Y. Wang and J. M. Bowman, J. Chem. Phys. **134**, 154510 (2011).

20. M. Rossi, H. Liu, F. Paesani, J. Bowman and M. Ceriotti, J. Chem. Phys. **141**, 181101 (2014).

21. Y. Wang and J. M. Bowman, J. Phys. Chem. Lett. **4**, 1104 (2013).

22. C. J. Tainter, P. A. Pieniazek, Y.-S. Lin and J. L. Skinner, J. Chem. Phys. **134**, 184501 (2011).

23. J. M. Bowman, X. Huang, and S. Carter, Spectrochim. Acta A **58,** 839 (2002).

24. A. K. Samanta, G. Czakó, Y. Wang, J. S. Mancini, J. M. Bowman, and H. Reisler, Acc. Chem. Res. **47**, 2700 (2014).

25. J. S. Mancini and J. M. Bowman, J. Chem. Phys. **139**, 164115 (2013).

26. J. M. Bowman, Y. Wang, H. Liu and J. S. Mancini, J. Phys. Chem. Lett. **6**, 366 (2015).

27. J. S. Mancini and J. M. Bowman Phys. Chem. Chem. Phys. **17**, 6222 (2015).

Chapter 6.

Water Hexamer

6.1. Overview

The water hexamer has attracted the interest of chemists for more than two decades because it is the "smallest droplet" of water.[1] The several low-lying isomers with only small differences in energy and entropy have stimulated a series of state-of-the-art spectroscopic and theoretical studies. The seminal work using vibration-rotation tunneling spectra has identified the cage as the most stable structure at 6 K.[1] Rare-gas tagging vibrational action spectra measured at higher temperature show that the book isomer is dominant.[2,3] In helium nanodroplet, the isomer form seen is the higher-energy cyclic ring, evidently because the rapid cooling of monomers in helium surrounding prohibits the cyclic structure from isomerizing to the low-lying forms.[4,5] Very recently, the prism isomer of $(H_2O)_6$ has been observed for the first time from broadband rotational spectroscopy,[6] however, the cage isomer was reported as the dominant isomer, in agreement with previous microwave experiments.[1]

Theoretically, coupled-cluster calculations with single, double and perturbative

triple excitations, CCSD(T), using complete-basis-set extrapolation, shows the that prism isomer has the lowest electronic energy.[7-10] The energy of the cage isomer is approximately 0.25 kcal/mol higher than the prism. A recent study using the parametric two-electron reduced density matrix (2-RDM) method shows the cage isomer has a 0.07 kcal/mol higher electronic energy than the prism isomer.[11] The small electronic energy difference between isomers can be compensated with the zero-point energy and at non-zero temperature entropy, resulting in a different free-energy ordering at different temperatures. At 0 K, including zero-point energy (ZPE), full-dimensional diffusion Monte-Carlo (DMC) calculations using the *ab initio* WHBB water potential shows the prism and cage are nearly isoenergetic.[12] Replica-exchange path-integral molecular dynamics (RE-PIMD) shows the fraction of cage versus prism isomer increases as temperature rises.[12] Up to 60 K, the book isomer has a negligible population, but becomes dominant when the temperature is above 150 K, due to the its floppier structure and thus higher entropy.[12] A recent PIMD simulation by Babin and Paesani,[13] using WHBB and their new related *ab initio* PES, denoted HBB2-pol, shows that for $(D_2O)_6$ the prism is dominantly populated at temperatures below at least 30 K. This important finding, which is understandable based on the diminished effect of ZPE, will hopefully stimulate new experiments on the isotopologs.

There have been a number of theoretical simulations of the IR spectra of

hexamer clusters, most recently by Tainter and Skinner,[14] and Wang and Bowman.[15] The latter considered the overtone of the monomer bend and showed its importance in the "OH-stretch" portion of the spectrum. With inclusion of these bands agreement between theory and experiment for the cyclic ring and book isomers is very good.

Dilute mixtures of HOD in D_2O and H_2O have been used to decouple and thereby isolate the spectroscopy and vibrational relaxation dynamics of the OD and OH stretches in HOD, see for example refs. 16-18 and references therein for liquid, and ref. 19 and references therein for ice. Simulations of the vibrational spectra of dilute HOD in water systems have been reported.[20-23] We recently reported quantum calculations of the vibrational relaxation pathways of the OH and OD stretches for dilute HOD in D_2O and H_2O Ice Ih.[24]

In recent work by Skinner and co-workers, "dilute" HOD in the water hexamer cage was investigated.[23] Specifically, the IR spectrum of the cage isotopolog of $HOD(D_2O)_5$ in the range 3000-3800 cm^{-1} was calculated using that group's combined quantum and classical approach, with each OH stretch treated as a local mode. The OH-stretch frequencies of the 12 unique sites for HOD in this cluster were shown to be correlated with the hydrogen bonding class, based on both the donor and acceptor H-bonding environment. By contrast for HOD in liquid and ice D_2O the calculated and experimental spectra show two seemingly simple broad

peaks centered on the OD-stretch and the OH-stretch.

Stimulated by this work and also by the recent prediction of Babin and Paesani[13] that the prism form of $(D_2O)_6$ is lower in free energy at low temperatures than the cage isomer, we consider both the prism and cage isomers of $HOD(D_2O)_5$, as it is likely that both are significantly populated at low temperatures. We also extend the spectral range down to 1000 cm^{-1} in order to encompass all the monomer intramolecular spectral features. In addition, we examine the energetic site dependence of the HOD in these clusters to shed light on whether there is a possible significant non-uniform distribution among the twelve sites. The answer to this question may be relevant to the site distribution of dilute HOD in the liquid and ice environments mentioned above. Finally, following our earlier calculations on the IR spectrum of pure H_2O Ice Ih,[25] we present the analogous spectra for pure D_2O and pure HOD Ice Ih.

6.2. HOD Doped Cage and Prism Hexamer

In this work, as noted already we consider the prism and cage isomer and use the structures from WHBB, which were reported in ref. 26. We systematically hydrogenate the 12 unique positions of the cage and prism $(D_2O)_6$, therefore consider 12 $HOD(D_2O)_5$ isotopomers for both cage and prism.

For the present application to $HOD(D_2O)_5$, the LMon calculation is

straightforwardly performed for each monomer for the cage and prism isomers of $HOD(D_2O)_5$.

In recognition of the relaxation, we apply a Lorentzian lineshape function to each stick. The full-width at half maximum is chosen to be 5 cm^{-1}, which corresponds to a reasonable guesstimate of the lifetime of the order of a picosecond, which is based on lifetimes reported for HOD in ice, see ref. 24 and references cited therein. The resulting spectra should look a bit more like experimental ones at low temperature, where rotational broadening of the band is quite narrow. Stick spectra are also shown in separate figures just in the OH stretch region to assign each feature to a site and the nature of the H-bonding.

Finally, to estimate the H-atom site energetics, harmonic zero-point energy analysis is done for each of the 12 isotopomers. This was done by performing a full dimensional, i.e., 6x9= 54, normal mode analysis for each isotopomer from which the harmonic ZPE is then trivial to obtain for each isotopomer. The full normal mode analysis is efficient using the PES, taking roughly 5 seconds per isotopomer, on a single CPU of a 5-year old workstation. It is perhaps worth noting that it is not necessary to diagonalize the Hessian to get the total harmonic ZPE, as reported previously by Higgs.[26] We did not use this interesting approach, however.

6.3. IR Spectra of Prism and Cage $HOD(D_2O)_5$

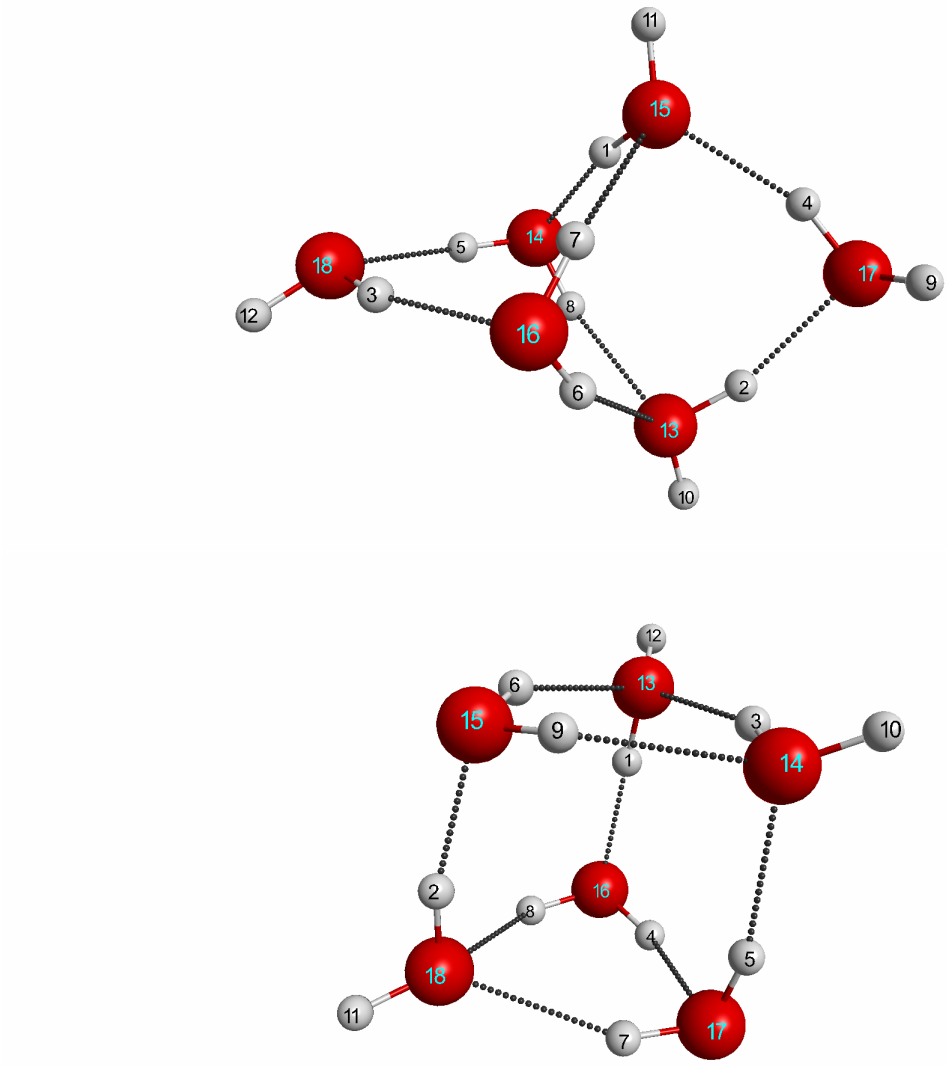

Figure 6.1. Structure and atom numbering for the cage (top) and prism (bottom) isomers of water hexamer.

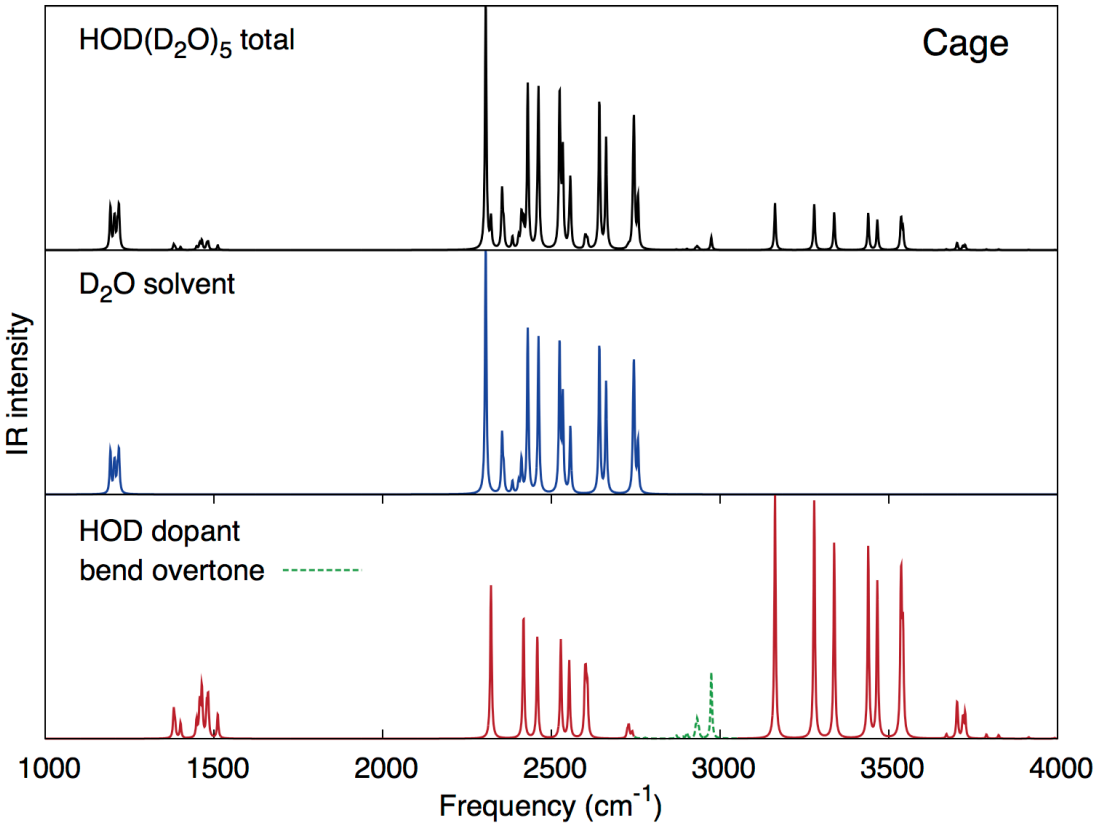

Figure 6.2. IR spectra of cage $HOD(D_2O)_5$

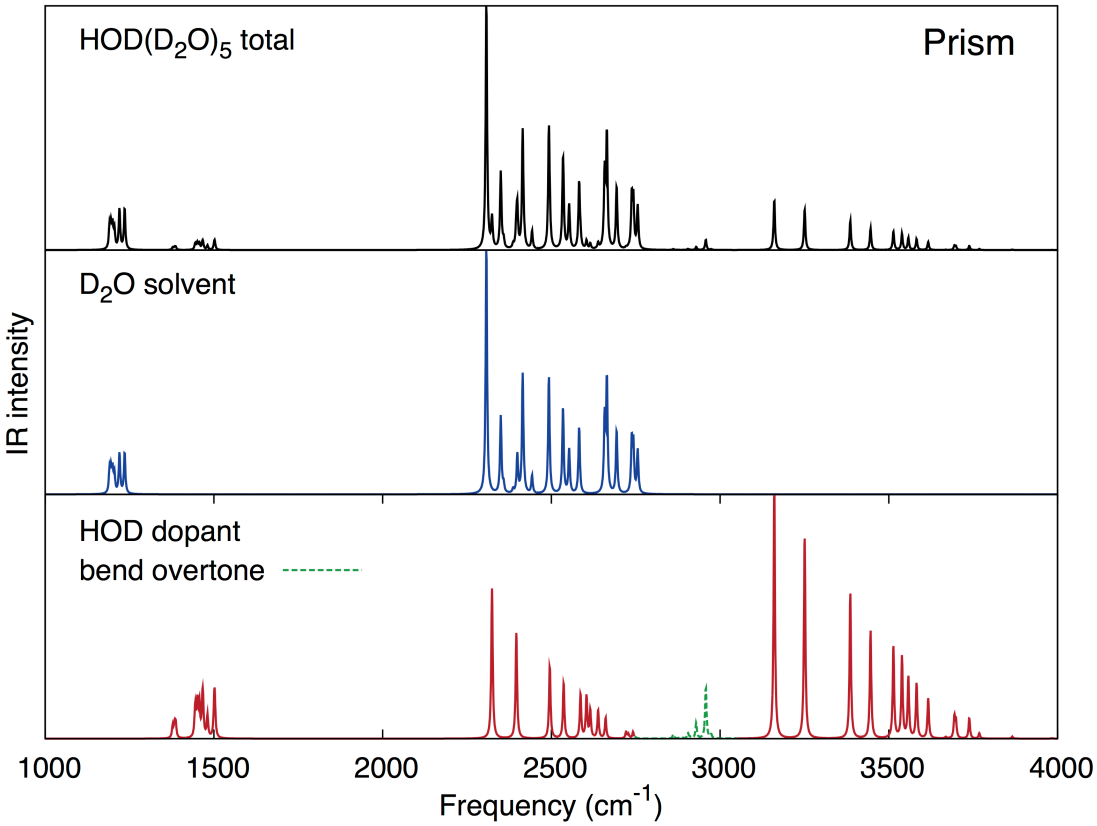

Figure 6.3. IR spectra of prism $HOD(D_2O)_5$

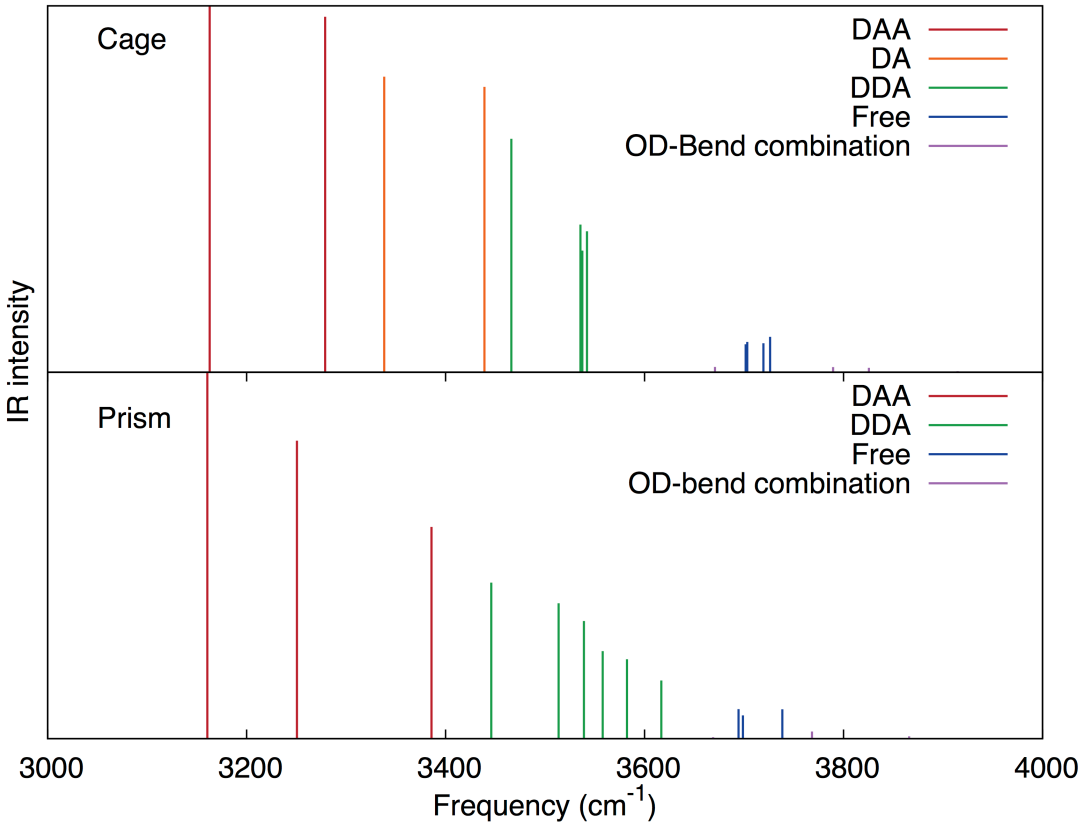

Figure 6.4. OH stretch band of IR spectra of the cage and prism $HOD(D_2O)_5$.

The structures and atom number assignments of the cage and prism hexamers are shown in Figure 6.1. As noted, there are 12 unique hydrogen sites for both cage and prism isomers, so there are 12 isotopomers of $HOD(D_2O)_5$. These are numbered in the figure in ascending order by the OH-stretch frequency, based on our calculations. The complete IR spectrum for all 12 isotopomers of the cage $HOD(D_2O)_5$ in the range 1000-4000 cm-1 from LMon calculations is shown in Figure 6.2. The contributions from each "dopant" HOD and the five "solvent" D2O are also shown in the bottom two panels. From bottom up, the spectrum of the HOD

monomers have 4 bands: the HOD bends clustered at roughly 1500 cm^{-1}, the OD stretches in the range 2300-2750 cm^{-1}, the bend overtone at roughly 3000 cm^{-1}, OH stretches in the range 3150-3750 cm^{-1}, and finally weak features at around 3700 cm^{-1}, due to the HOD bend plus the H-bonded OD stretch. For D_2O, the bending modes are at roughly 1200 cm^{-1}, and the bands in the range 2300-2750 cm^{-1} include the OD stretches and small contributions from the overtone of the D_2O bend in the range 2350-2410 cm^{-1}. The total spectrum of $HOD(D_2O)_5$, obtained by combining the bands of both the HOD dopant and D_2O solvent, is shown at the top panel of Figure 6.2. Notice the intensities for D_2O bend and OD stretch bands are larger than those of the corresponding bands of HOD monomers; this is mainly due to the ratio of dopant and solvent, which is 1:5. Note to obtain the overall spectrum, equal population of the 12 isotopomers of $HOD(D_2O)_5$ is assumed. In Section 3.3, we discuss this in detail.

The corresponding spectra of the prism $HOD(D_2O)_5$ are shown in Figure 6.3. Compared with the spectra of the cage in Figure 6.2, the prism spectra show the same bands in similar frequency ranges. However, a noticeable difference from the cage spectrum is seen in structure of the OH stretch portion of the spectrum. Detailed discussion of these OH-stretch bands of both isomers will be presented below. The same assumption that populations of the 12 isotopomers are equal is applied to the prism as well.

Next, we focus on the OH-stretch region of the IR spectra for the cage and prism $HOD(D_2O)_5$. These bands are of most interest because the OD-stretch bands in HOD are largely masked by the D_2O solvent stretch-bands. To analyze this portion of the spectra, we present the stick spectra of the cage and the prism from LMon calculations in Figure 6.4. There are 12 sticks for each isomer, which correspond to the 12 unique hydrogen sites, spanning a range from 3150 to 3700 cm^{-1}. (Note the HOD bend overtone is below 3000 cm-1 and not shown in Figure 6.4, unlike the case of pure H2O where the bend overtone is embedded in the OH-stretch region of the spectrum[25]). As seen, each stick is color-coded according to the well-known Donor (D)/Acceptor (A) classification.[2] We discuss this in detail below, but first we make a more "coarse-grained" observation about these stick spectra. It is based on identification of two types of monomers. One is with one free-OH(D) and one H-bonded OH(D). There are four such monomers in the cage and three in the prism. The second monomer type is with no free-OH(D) stretches and thus with two H-bonded OH(D) stretches. There are two of these monomers in the cage and three in the prism. We now note that for the first type of monomer, i.e., with one free-OH(D), the two OH-stretches spectral sticks are at the extremes of the spectral range. The free-OH stretches, shown in blue, are the highest frequency bands in the spectrum and the H-bonded OH-stretches, shown in red and orange, are the lowest frequency bands of the spectrum. The OH-bands for the second type of

monomer, which has 2 H-bonded OH-stretches, shown in green, are between the free-OH bands and the lowest frequency H-bonded OH bands, which are assigned to the first type of monomer. (Note the same correlation of OH stretch frequency and monomer type is seen in the correspondent pure $(H_2O)_6$.)

To go beyond this coarse-grained analysis, the D/A classification is used. Recall a monomer with two donor H-atoms and two acceptor H atoms is labeled as DDAA. We use this notation to indicate only the H-bonded OH-stretches and continue to use the term "Free" to indicate free-OHs. This labeling is used in Table 6.1, where each labeled spectral line is identified by the site numbering shown in Figure 6.1. For the cage isomer, it is straightforward to see the H-bonded OH-stretches on the first type of monomer are either DAA or DA. The H-bonded OH-stretches on the second type of monomer are DDA. We see the DAA OH-stretches, shown in red sticks, are more red-shifted than the DA ones, shown in orange sticks. For the prism, all H-bonded OH-stretches on the first type of monomer are DAA, and the ones on the second type are DDA. To summarize, the OH-stretch frequencies are in the order of DAA < DA < DDA < Free. This order, seen in the cage and prism isomers, is consistent with the results of the book isomer in pure $(H_2O)_6$.[2] Finally it is worthwhile to note that Ohno *et al*[27] and later Tainter *et al*[23] have analyzed the OH frequencies by considering not only the H-bond

configurations on the donor monomer but also on the acceptor monomer, using an "M-index". This provides additional insights into the pattern of spectral features and also in making connections with the condensed phase and surfaces and we refer the reader to those papers for this insightful and detailed analysis.

Table 6.1. Monomer classification of the 12 $HOD(D_2O)_5$ isotopomers of the cage and prism isomers. Hydrogen sites follow the atomic numbering in Figure 6.1. For H-bond type, D denotes one donor and A denotes one acceptor.

Hydrogen site	Cage	Prism
1	DAA	DAA
2	DAA	DAA
3	DA	DAA
4	DA	DDA
5	DDA	DDA
6	DDA	DDA
7	DDA	DDA
8	DDA	DDA
9	Free	DDA
10	Free	Free

11	Free	Free
12	Free	Free

Next, we compare our numerical results for the cage isomer with previous local-mode calculations of the OH-stretch fundamental of Skinner and coworkers[23] in Table 6.2. For consistency, we show the current OH-stretch fundamentals; however, we remind the reader that in this energy range there are also combination states of the HOD bend plus H-bonded OD-stretch. As seen, the two calculations are consistent with each other, but there are some differences too. First, peaks 4 and 5 from our calculations are blue-shifted by 40 cm^{-1} compared with the local-mode ones. Second, in our calculations sticks 6,7,8 are very close in frequencies, whereas the local-mode peaks are more dispersed. Overall it is gratifying to see good agreement between these two calculations given that there are significant differences in their details. Perhaps the biggest difference is the treatment of the electronic structure, which in the local-mode calculations is DFT-B3LYP/6-311++G** for the OH-stretch and a semi-empirical three-body interaction and in the LMon ones, using WHHB, which is based on CCSD(T)/aug-cc-pVTZ for the intrinsic two-body and MP2/aug-cc-pVTZ for the intrinsic three-body interactions. A significant point in common is the explicit consideration of the important three-body interactions.

Table 6.2. OH stretch frequencies of the 12 sites of the cage and prism $HOD(D_2O)_5$. Also shown is the OH stretch frequencies of the cage $HOD(D_2O)_5$ with the local-mode calculations from ref. 23. (The frequencies from ref. 23 were determined by us from digitized versions Figure 6.1 in that paper.)

Peak	Cage this work	Cage Ref. 23	Prism this work
1	3163	3148	3161
2	3279	3274	3251
3	3338	3330	3386
4	3439	3392	3446
5	3466	3421	3514
6	3536	3517	3539
7	3537	3547	3558
8	3542	3576	3582
9	3702	3709	3617
10	3703	3714	3694
11	3719	3727	3699
12	3726	3738	3738

Finally, we compare the spectra of the cage and prism isomers. The most significant difference between the two isomers is perhaps in the region above 3500 cm^{-1}. In this region, the spectrum of the prism is more dispersed than the cage. This suggests that IR spectroscopy should be able to clearly distinguish the cage and prism isomers of $HOD(D_2O)_5$.

6.4. Harmonic Zero-Point Energies of Isotopomers of Prism and Cage $HOD(D_2O)_5$

Table 6.3. Harmonic zero-point energy (ZPE) and ΔZPE, relative to cage $(D_2O)_6$, of the twelve $HOD(D_2O)_5$ isotopomers of the cage hexamer. The site labels are given in Figure 6.1. The harmonic frequency for each OH is also shown.

Hydrogen site	Frequency (cm^{-1})	ZPE (kcal/mol)	Δ ZPE (kcal/mol)
1	3382	71.50	2.18
2	3503	71.48	2.16
3	3549	71.48	2.16
4	3635	71.49	2.17
5	3671	71.50	2.18
6	3727	71.46	2.14

7	3732	71.46	2.14
8	3737	71.47	2.15
9	3893	71.33	2.00
10	3899	71.34	2.01
11	3906	71.35	2.03
12	3918	71.30	1.97

It is of interest to investigate the site-dependence of the ZPEs of the cage and prism isotopomers of $HOD(D_2O)_5$. These were obtained in the harmonic approximation, as described above, and the results are given in Tables 6.3 and 6.4, respectively. As seen these range from 71.30-71.50 kcal/mol for the cage and 71.56-71.73 kcal/mol for the prism. Note these energies are relative to the potential minimum of the corresponding isomer. It is well established that the prism minimum is below the cage one as discussed in more detail below. From these ZPEs we define the "hydrogenation energy" as the ZPE difference between the $HOD(D_2O)_5$ and the reference energies of cage or prism $(D_2O)_6$:

$$\Delta E_H = E[HOD(D_2O)_5] - E[(D_2O)_6]$$

We see this energy is of the order of 2 kcal/mol, for any of the 12 sites in the cage or prism isomers. However, at the "free-OD" sites, ΔE_H is about 0.15-0.2 kcal/mol lower than ΔE_H at "hydrogen-bonded" positions, for both cage and prism. This

suggests that at 0 K to about roughly 100 K hydrogenation is energetically favored at the "free-OD" positions. We must add an important caveat to this conclusion though. As is well known, especially by us, harmonic ZPEs are not accurate to within 0.15-0.2 kcal/mol for a cluster this large, however, the estimate of the *difference* in harmonic ZPEs is probably at least of the right sign, based on cancellation of errors. And so, it should be reasonable guide to the site preference of H-atom substitution. Also note this suggests the relative intensities of IR spectral bands might be altered due to the non-equal populations of the 12 sites.

Table 6.4. Harmonic zero-point energies (ZPE) and ΔZPE, relative to prism $(D_2O)_6$, of the twelve $HOD(D_2O)_5$ isotopomers of the prism hexamer. The site labels are given in Figure 6.1. The harmonic frequency for each OH is also shown.

Hydrogen site	Frequency (cm^{-1})	ZPE (kcal/mol)	Δ ZPE (kcal/mol)
1	3385	71.73	2.18
2	3473	71.72	2.16
3	3596	71.71	2.15
4	3646	71.73	2.18
5	3715	71.69	2.13
6	3730	71.69	2.13

7	3748	71.70	2.14
8	3776	71.67	2.12
9	3805	71.66	2.11
10	3891	71.56	2.01
11	3904	71.58	2.02
12	3921	71.59	2.03

A similar analysis could be done for dilute HOD in condensed phase; however, that would be a fairly major computational effort for a future study. However, based on the very limited study for the hexamer which shows the largest difference for the free-OH and the fact that there are no free-OH stretches in the core regions of the ice or liquid it is likely that the differences in ZPEs are quite small from site to site.

Finally, we attempt to answer the question which isomer of $HOD(D_2O)_5$ is more stable at 0 K, cage or prism? The CCSD(T)/CBS calculations shows the electronic energy of the prism is lower than the cage by 0.25 kcal/mol.[9] For the harmonic ZPE, all the 12 isotopomers of the prism are higher than the highest-energy isotopomer of the cage. The relative harmonic ZPE of the prism over cage ranges from 0.06 to 0.43 kcal/mol. Therefore, this suggests both the cage and the prism could be the most stable isomer, depending on the hydrogen sites. These preliminary predictions

may be tested by new experiments on the isotopologs of water hexamers.

6.5. Summary

We presented local-monomer IR spectra of the cage and prism isomers of $HOD(D_2O)_5$ in the range of 1000-4000 cm^{-1}. The appearance of the bend overtone in the region of 2700-3000 was noted. The OH stretch bands of both isomers show rich structures, due to the abundant H-bonding environments. Also, the spectra of HOD and D_2O ice Ih were presented, and these are in good quantitative agreement with experiment. Finally, we reported preliminary site-energetics of the 12 isotopomers of the cage and prism $HOD(D_2O)_5$ based on harmonic zero-point energy analysis.

References

1. K. Liu, M. G. Brown, C. Carter, R. J. Saykally, J. K. Gregory and D. C. Clary, Nature **381**, 501 (1996).
2. C. Steinbach, P. Andersson, M. Melzer, J. K. Kazimirski, U. Buck and V. Buch, Phys. Chem. Chem. Phys. **6**, 3320 (2004).
3. E. G. Diken, W. H. Robertson and M. A. Johnson, J. Phys. Chem. A **108**, 64 (2003).
4. K. Nauta, Science **287**, 293 (2000).
5. C. J. Burnham, S. S. Xantheas, M. A. Miller, B. E. Applegate and R. E. Miller, J. Chem. Phys. **117**, 1109 (2002).
6. C. Perez, M. T. Muckle, D. P. Zaleski, N. A. Seifert, B. Temelso, G. C. Shields, Z. Kisiel and B. H. Pate, Science **336**, 897 (2012).
7. E. E. Dahlke, R. M. Olson, H. R. Leverentz and D. G. Truhlar, J. Phys. Chem. A **112**, 3976 (2008).
8. B. Santra, A. Michaelides, M. Fuchs, A. Tkatchenko, C. Filippi and M. Scheffler, J. Chem. Phys. **129**, 194111 (2008).
9. D. M. Bates and G. S. Tschumper, J. Phys. Chem. A **113**, 3555 (2009).
10. U. Góra, R. Podeszwa, W. Cencek and K. Szalewicz, J. Chem. Phys. **135**, 224102 (2011).
11. J. J. t. Foley and D. A. Mazziotti, J. Phys. Chem. A **117**, 6712 (2013).

12. Y. Wang, V. Babin, J. M. Bowman and F. Paesani, J. Am. Chem. Soc. **134**, 11116 (2012).

13. V. Babin and F. Paesani, Chem. Phys. Lett. **580**, 1 (2013).

14. C. J. Tainter and J. L. Skinner, J. Chem. Phys. **137**, 104304 (2012).

15. Y. Wang and J. M. Bowman, J. Phys. Chem. Lett.**4**, 1104 (2013).

16. E. T. J. Nibbering and T. Elsaesser, Chem. Rev.**104**, 1887 (2004).

17. R. Rey, K. B. Møller and J. T. Hynes, Chem. Rev.**104**, 1915 (2004).

18. H. J. Bakker and J. L. Skinner, Chem. Rev.**110**, 1498 (2009).

19. F. Perakis, J. A. Borek and P. Hamm, J. Chem. Phys. **139**, 014501 (2013).

20. M. S. Bergren, D. Schuh, M. G. Sceats and S. A. Rice, J. Chem. Phys. **69**, 3477 (1978).

21. M. J. Wojcik, V. Buch and J. P. Devlin, J. Chem. Phys. **99**, 2332 (1993).

22. F. Li and J. L. Skinner, J. Chem. Phys. **132**, 204505 (2010).

23. C. J. Tainter, Y. Ni, L. Shi and J. L. Skinner, J. Phys. Chem. Lett.**4**, 12 (2013).

24. H. Liu, Y. Wang and J. M. Bowman, J. Am. Chem. Soc. **136**, 5888 (2014).

25. H. Liu, Y. Wang and J. M. Bowman, J. Phys. Chem. Lett.**3**, 3671 (2012).

26. P. W. Higgs, J. Chem. Phys. **21**, 1300 (1953).

27. K. Ohno, M. Okimura, N. Akai and Y. Katsumoto, Phys. Chem. Chem. Phys. **7**, 3005 (2005).